MMNSA

Mathematical Modelling and Numerical Simulation with Applications

ISSN Online : 2791-8564

Year : 2022

Volume : 2

Issue : 1

www.mmnsa.org

EDITOR-IN-CHIEF
Mehmet Yavuz, PhD,
Necmettin Erbakan University, Turkey

VOLUME: 2 ISSUE: 1
ISSN ONLINE: 2791-8564

March 2022
https://www.mmnsa.org

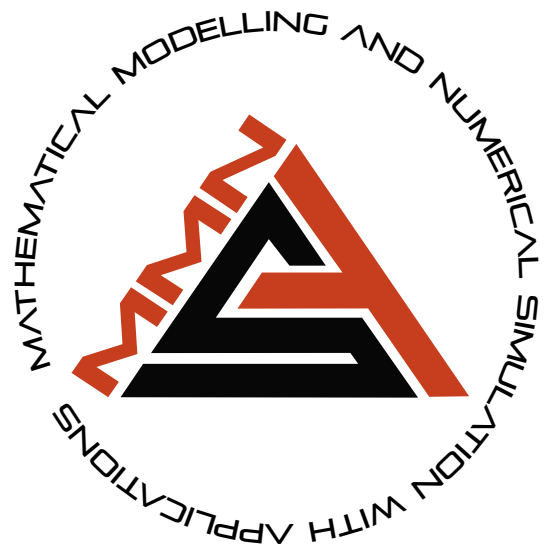

MATHEMATICAL MODELLING AND NUMERICAL SIMULATION WITH APPLICATIONS

Technical Editor

Halil İbrahim Özer
Department of Computer and Instructional Technologies
Education, Ahmet Keleşoğlu Faculty of Education,
Necmettin Erbakan University, Meram Yeniyol, 42090
Meram, Konya/TURKEY
hiozer@gmail.com

English Editor

Abdulkadir Ünal
School of Foreign Languages, Foreign Languages, Alanya
Alaaddin Keykubat University, Alanya,
Antalya/TURKEY
abdulkadir.unal@alanya.edu.tr

Editorial Secretariat

Fatma Özlem Coşar
Department of Mathematics and Computer Sciences,
Faculty of Science, Necmettin Erbakan University,
Meram Yeniyol, 42090 Meram, Konya/TURKEY

Müzeyyen Akman
Department of Mathematics and Computer Sciences,
Faculty of Science, Necmettin Erbakan University,
Meram Yeniyol, 42090 Meram, Konya/TURKEY

Contents

Research Articles

Mathematical Modelling and Numerical Simulation with Applications, 2022, 2(1), 1–12

https://www.mmnsa.org
ISSN Online: 2791-8564 / Open Access
https://doi.org/10.53391/mmnsa.2022.01.001

RESEARCH PAPER

Ion temperature gradient modes driven soliton and shock by reduction perturbation method for electron-ion magneto-plasma

Aziz Khan[1,2,*,‡], Abbas Khan[3,‡] and Muhammad Sinan[4,‡]

[1]Department of Physics, University of Malakand, Chakdara Dir(L), 18000, Khyber Pakhtunkhwa, Pakistan, [2]Department of Physics, Government Degree College, Swat, 18800, Khyber Pakhtunkhwa, Pakistan, [3]Department of Mathematics, University of Peshawar, Peshawar, 15000, Pakistan, [4]School of Mathematical Sciences, University of Electronic Science and Technology of China, Chengdu, 611731, China

* Corresponding Author
‡ azizkhanphysics@gmail.com (Aziz Khan); std104602@uop.edu.pk (Abbas Khan); sinanmathematics@gmail.com, 202124110102@std.uestc.edu.cn (Muhammad Sinan)

Abstract

In our observation, we have used an easy and reliable approach of the reduction perturbation method to obtain the solution of the ion temperature gradient mode driven linear and nonlinear structures of relatively small amplitude. One can use that methodology in the more complex environment of the plasma and can obtain a straightforward approach toward his studies. We have studied different parameter impacts on the linear and nonlinear modes of the ITG by using data from tokamak plasma. Hence, our study is related to the tokamak plasma and one that can apply to the nonlinear electrostatic study of stiller and interstellar regimes where such types of plasma environment occur.

Key words: Ion temperature gradient; soliton; shock; electron-ion plasma; reduction perturbation method; linear and nonlinear structures
AMS 2020 Classification: 70K60; 35A09; 35G20

1 Introduction

Most of the research work has been done on the linear and nonlinear structures over the last few decades and its applications are compared with the stiller and interstellar spaces where the medium is plasma [1, 2, 3]. For that purpose, many researchers investigated the electron temperature gradient (ETG) and ion temperature gradient (ITG) drift mode in which some of them used the simplest slab geometry [4, 5] and the other used some complex geometry like toroidal geometry [6]. Mathematically ITG coefficient is defined as $\eta_i = L_n/L_T$ [10] while $L_T = 1/\partial x \ln T_{io}(x)$ and $L_n = 1/\partial x \ln n_{io}(x)$ are the ion temperature and ion density scale lengths. For the first time, ITG driven mode was studied by Sagdeev and Rudakov [4], then the work extended to the nonuniform number density of plasma species with a shear magnetic field where ion kinetic effect was also introduced in their calculation. The same research was extended further with inhomogeneous plasma configuration for the instability limits in the toroidal geometry. Further, the pressure effect in the same geometry was also observed [5]. Under the external magnetic field applied to the plasma, some of the new properties of the ITG mode were introduced by Hahm and Tang [8]. Jerman et al. [10] using heat flux effect in the energy balancing equation and Braginskii's equation to derive ITG mode equation for the simple Maxwellian electron-ion plasma. The ITG and toroidal ITG modes were studied and coupled by Shukla [11, 12] the same scientists also obtained theoretical calculations for the dipolar vortices. Zakir et al. [13] calculated the nonlinear structure of dipolar vortices in the

➤ **Received:** 19.12.2021 ➤ **Revised:** 16.01.2022 ➤ **Accepted:** 19.01.2022 ➤ **Published:** 22.01.2022

plasma where electrons species were considered to be super-thermal. Adnan et al. [14] observed low-frequency electrostatic waves in an inhomogeneous plasma. Whether the instability is of η_e type or η_i type these both are very strong as compared to the gyro-radius (ρ_e/ρ_i) and driven fluxes effects [18]. In the ITG mode-driven instability both temperature gradient and number density fluctuations are out of phase, and those types of modes are robust in the non-thermal regime. η_i mode instabilities are produced due to the free energy that is stored in the form of ITG mode [16, 15].

Fluid-like plasma is complex and nonlinear where the nonlinear structures like solitary shock waves can transport heat energy, mass, and momentum inside the fluid from one to another, bringing instability in the [19, 20, 21, 22]. The nonlinear collision-less structures were studied by Sabry et al. [23] in a plasma whose constituents are electron-positron and ions. Nonlinear solitary waves were studied by many authors considering various models of plasma [24, 25], shocks [26] and vortices of the two dimensional by the authors [27, 28, 29]. For the first time, Zakir et al. [17] studied the linear and nonlinear solitary and shock waves structure in the ITG driven mode instability by considering electron to be Maxwellian and ion dynamic. Khan et al. [30] extended the work by incorporating the entropy drift in the momentum equation of the fluid and the effect of entropy in the ITG mode, his study revealed that entropy is an essential factor in the transportation of instability in the plasma. Javed et al. [32] theoretically obtained the solitary wave potential solution from the kdv equation in the ITG mode by homotopy perturbation method (HPM) and compare the solution of the analytical and HPM method and gives that both types of solutions agree with each other if the time interval is taken very small. Aziz et al. [33] observed ITG mode soliton and shock in electron-positron-ion magneto-plasma by taking electron and positron species as Maxwellian; the same work is carried out by Rehan et al. [34] and investigated the linear and nonlinear mode in (e-p-i) plasma taking electron to be super-thermal. Zakir et al. [17] studied the effects on the shock and solitary structure by taking the heat flux effect in the energy balancing equation of the ITG mode. Aziz et al. in [35] studied electron-positron-ion magneto-plasma by considering the entropy effect has study shows that it is one of the dominant factors in plasma parameters that can change the various linear and nonlinear structures magnificently in the fluid.

To observe different nonlinear structures like a soliton, shock, etc., in various compositions and models of a plasma, we can use the reduction perturbation technique (RPT). The reduction perturbation technique was first introduced theoretically to the problem's solution by [36, 37]. RPT has advantages like flexibility and algorithmic methodology to solve different problems in various fields of physics. Taniuti and Wei [38, 39] suggested RPT to be a generalized technique for obtaining the nonlinear partial differential equation of the corresponding waves in a model plasma [40]. Different types of waves to which that technique has been successfully applied are ion-acoustic in a hot and cold plasma, magnetosonic waves in both hot and cold plasma, etc. [41, 42]. As the literature shows us that no one has yet solved the shock and solitary waves solution in ITG mode by reduction perturbation technique so we for the first time investigating the problem of ITG mode driven soliton and shock formation in the electron-ion plasma by reduction perturbation method (RPT). This article is divided into the following sections: Section 2 gives MHD equations and the linear root calculation by the RPM method. In sections 3 and 4, we study the solitary and shock waves profiles; Section 5 concludes the related article.

2 Theory related to the model

We consider a nonuniform plasma consisting of two species as electron and ion, with a background magnetic field along the z-axis i.e., $B_0\hat{\mathbf{z}}$, where $\hat{\mathbf{z}}$ represents the unit vector along the z-axis and $\mathbf{B}_0$ is the magnitude of the magnetic field. We also considered the temperature and number density gradients in the x–direction to simplify the calculation of the ion temperature gradient modes driven linear and nonlinear study i.e., $d_x n_{i0} \neq 0$ and $d_x T_{i0} \neq 0$ for ions, here n_{i0}, T_{i0} are the equilibrium number density and ions temperature. The inertial mass for an electron in comparison to the ion is so small, therefor ions are taken dynamic while electrons are subjected to have Maxwellian distribution. We assume here low-frequency ITG mode i.e., $\partial_t \ll \omega_{ci} = (eB/m_i c)$, (here e stands for the ion charge, m_i is for the ion mass, B is taken for the magnitude of the magnetic field and c denote the speed of light). The fluctuations are considered to be electrostatic in nature, so we have taken $\nabla \times \mathbf{E} = 0$ in our calculation. The first equation of our model plasma for the ion temperature gradient mode is the ion momentum equation that is [13, 17],

$$(\partial_t + v_i.\nabla)\mathbf{v}_i = -\frac{e}{m_i}\mathbf{E} - \frac{1}{m_i n_i}(\nabla p_i), \tag{1}$$

where $\mathbf{E} = -\nabla\phi$. Under the action of some external forces plasma species are driven so the inhomogeneity occurs in different parameters of the plasma i.e., $n_i = n_{i0} + n_{i1}$, $T_i = T_{i0} + T_{i1}$ with $n_{i1} \ll n_{i0}$ and $T_{i0} \ll T_{i1}$ (here the quantities with subscript 0 denote the unperturbed parameters while those with subscript 1 denotes the perturbed plasma parameters). Ion velocity in the limit $\partial_t \ll \omega_{ci}$, superposed by different drifts that is given as [13, 17]

$$\mathbf{v}_i = \mathbf{v}_E + \mathbf{v}_{Di} + \mathbf{v}_{pi} + v_{ix}\widehat{x}, \tag{2}$$

where $\mathbf{v}_E = \frac{c}{B_0}(\hat{\mathbf{z}} \times \nabla\Phi)$, $\mathbf{v}_{Di} = \frac{c}{eB_0 n_i}(\hat{\mathbf{z}} \times \nabla P_i)$ and $\mathbf{v}_{pi} = -\frac{c}{B_0\omega_{ci}}(\partial_t + \mathbf{v}_i.\nabla)\hat{\mathbf{z}} \times \mathbf{v}_i$ are the $\mathbf{E} \times \mathbf{B}$ drift, ion diamagnetic drift and ion polarization drift. Here Φ, P_i represents the normalized electrostatic potential, ions pressure, and v_{ix}, the drift velocity's x—component. Here $P_i = n_i T_i$ is the ion pressure. The ion continuity equation is given by [13, 17]

$$\partial_t n_i + \nabla.(n_i \mathbf{v}_i) = 0. \tag{3}$$

The energy balance equation is given as [13, 17]

$$\frac{3}{2}\left(\partial_t + \mathbf{v}_i \cdot \nabla\right) T_i + T_i(\nabla \cdot \mathbf{v}_i) n_i = -\frac{1}{n_i}\nabla.\left[(5T_i/2eB_0)\hat{z} \times \nabla T_i\right], \tag{4}$$

$(5T_i/2eB_0)\hat{z} \times \nabla T_i$ is known as Righi-Leduce heat flux term for ions due to the ion temperature gradient. Now at the last Poission equation (that is based on the Gauss's law for electric flux) is as [13, 17]

$$\nabla^2\phi = 4\pi e(n_i - n_e). \tag{5}$$

Now to incorporate drift speed of ion v_i in the equations of (1-5) and after a little manipulation we can get the continuity equation as [13, 17]

$$D_t^i N + \tau \mathbf{v}_{ni} \nabla \Phi - \frac{1}{2} \rho_i^2 \tau^{-1} \partial_t \nabla^2 (T + N + \Phi) + \partial_z v_{iz} = 0. \tag{6}$$

In above expression, the new terms introduced are defined as $D_t^i = (\partial_t + \mathbf{v}_E.\nabla)$ [13, 17], $\mathbf{v}_{ni} = \left(\frac{cT_{io}}{eB_0}\right) \nabla \ln n_{io} \times \hat{\mathbf{z}}$, $\tau = \frac{T_{eo}}{T_{io}}$, $T = \frac{T_{i1}}{T_{io}}$, $N = \frac{n_{io1}}{n_{io}}$ and $\Phi = \frac{e\phi}{T_{eo}}$. The momentum equation obtained is as

$$(\partial_t + v_{iz}\partial_z) v_{iz} + c_s^2 \nabla \left[\Phi + \tau^{-1}(T + N)\right] = 0. \tag{7}$$

here $c_s = \rho_s \omega_{ci}$. Using the drift approximation in Eq. (4) and neglected the Righi-Leduce heat flux term in the same equation we can get the energy balance equation as

$$\partial_t T - \frac{2}{3} \partial_t N = \tau \left(\eta_i - \frac{2}{3}\right) \mathbf{v}_{ni}.\nabla \Phi. \tag{8}$$

While the Poisson equation in the form of

$$\nabla^2 \Phi = \alpha_1 \left(\frac{n_{e0}}{n_{i0}} \Phi - N\right), \tag{9}$$

where $\alpha_1 = \frac{4\pi e^2 n_{i0}}{T_e}$ in the Poisson equation which is based on the electric flux according to Gauss's law.

Phase velocity

To get dispersion relation for the ITG mode, we use a compelling reduction perturbation method (RPM). From the dispersion relation, we then can extract phase velocity for the same mode that will reveal the linear behavior of the ITG mode. To proceed further, we first introduce the stretching coordinate to express all the differential equations of Eqs. (1)-(5) in terms of ξ– the coordinate system as did by [44]. The stretching coordinates are given as $\xi = \epsilon^{\frac{1}{2}}(\frac{x}{u} - t)$ and $\ell = \epsilon^{\frac{3}{2}} t$ where the parameter ϵ has a very small value that represents, the weakness of the mode amplitude and u is the phase velocity of the mode. We write equations (6)-(9) in the stretching coordinate and then use the following power series for the different normalized quantities i.e.,

$$\begin{pmatrix} N \\ v_{ix} \\ T \\ \Phi \end{pmatrix} = \begin{pmatrix} 1 \\ 0 \\ 1 \\ 0 \end{pmatrix} + \sum_{n=1}^{m} \epsilon^n \begin{pmatrix} N^{(n)} \\ v_{ix}^{(n)} \\ T^{(n)} \\ \Phi^{(n)} \end{pmatrix}, \quad m \text{ is a higher order of the perturbation,} \tag{10}$$

which gives a number of equations. To express the lowest order of different normalized quantities in terms of each other we compare ϵ power one to both sides of each equation in the form of

$$N^{(1)} = \frac{\tau \mathbf{v}_{ni}}{u} \Phi^{(1)} + \frac{v_{ix}^1}{u}, \tag{11}$$

$$v_{ix}^{(1)} = \frac{c_s^2}{u} \left[\Phi^{(1)} + \tau^{-1} \left(T^{(1)} + N^{(1)}\right)\right], \tag{12}$$

$$T^{(1)} = \frac{2}{3} N^{(1)} - \tau \left(\eta_i - \frac{2}{3}\right) \frac{\mathbf{v}_{ni}}{u} \Phi^{(1)}, \tag{13}$$

$$N^1 = \Phi^1. \tag{14}$$

When coupled equations of $(11 - 14)$, we can get

$$1 - \frac{\tau \mathbf{v}_{ni}}{u} - \frac{c_s^2}{u^2} \left\{1 + \frac{5\tau^{-1}}{3} - \left(\eta_i - \frac{2}{3}\right) \frac{\mathbf{v}_{ni}}{u}\right\} = 0. \tag{15}$$

Eq. (15) is a cubic root equation w.r.t u, where u is the phase velocity for the ITG mode. By a little algebraic calculation, we can find easily the roots of Eq. (15). As the phase velocity is obtained from the linear algebraic equations, we can describe the linear properties of the mode from the roots. One root of Eq. (15) is as

$$u = \frac{1}{6\tau} \left[\frac{(2v_{ni}\tau^2 + (2 \times \sqrt[3]{2}\tau(v_{ni}^2\tau^3 + c_s^2(5 + 3\tau))))}{\Gamma} + 2^{\frac{2}{3}} \times \Gamma\right], \tag{16}$$

where $\Gamma = (s_1 + s_2)^{\frac{1}{3}}$, $s_1 = 33c_s^2 v_{ni}\tau^3 - 27c_s^2 v_{ni}\eta_i\tau^3 + 9c_s^2 v_{ni}\tau^4 + 2v_{ni}^3\tau^6$ and $s_2 = \sqrt{\tau^3(-4(v_{ni}^2\tau^3 + c_s^2(5 + 3\tau))^3 + v_{ni}^2\tau^3(2v_{ni}^2\tau^3 + c_s^2(33 - 27\eta_i + 9\tau))^2)}$. In Fig. (1), the graph shows the phase velocity against the electron to ion temperature ratio τ and the ion temperature gradient coefficient η_i. Observation of the graph shows that by enhancing the electron to ion temperature ratio, the phase velocity of the ITG mode decreases to the negative values, but the effect reverses as η_i value of the plasma enlarge in value. On the other side, the phase velocity increases with the ion temperature coefficient η_i. These observations

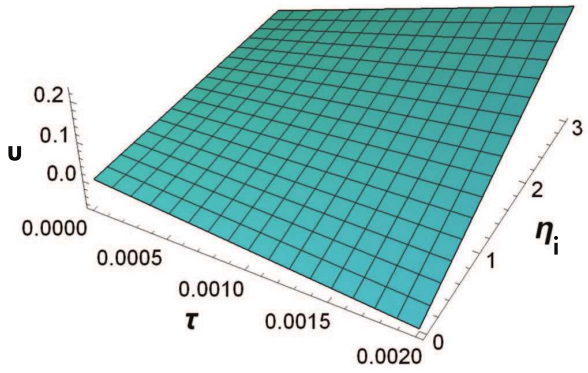

Figure 1. ITG driven mode phase velocity against τ and η_i.

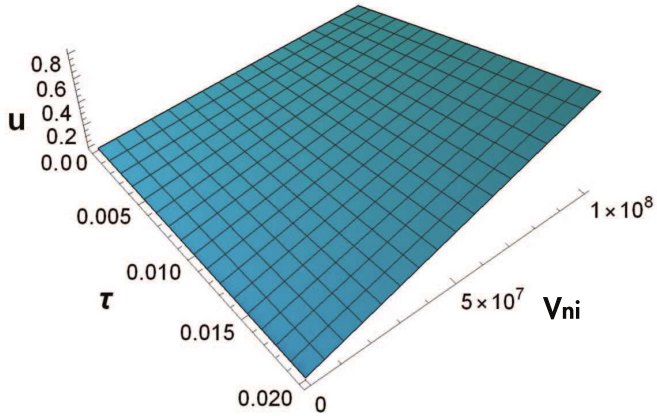

Figure 2. ITG driven mode phase velocity against τ and v_{ni}.

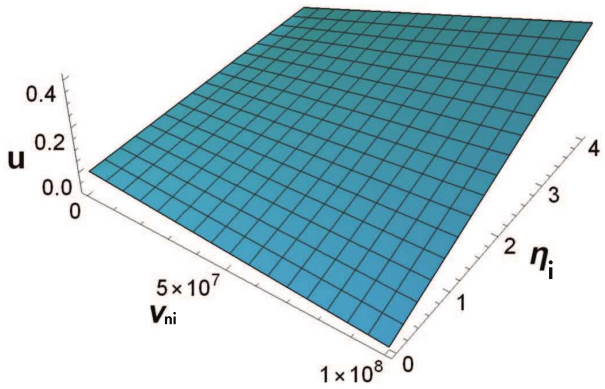

Figure 3. ITG driven mode phase velocity against τ and η_i.

remain valid with the mathematical reasoning because τ is related inversely with the ion temperature of the plasma so τ value increase means that the ion temperature decreases in the plasma, therefore, the mobility of the ion species decreases and also the phase velocity. On the other hand, the ion temperature coefficient is related directly to the change of ion temperature of the plasma, so an increase in the η_i value means increasing the value of the ion temperature in the plasma and the mobility of the ions phase velocity. Fig. (2) shows us that with v_{ni} and τ value the phase velocity of the linear mode can be enhanced here again. The ion drift speed v_{ni} related directly with the ion temperature of the plasma by increasing the v_{ni} value means to increase the value of the ion temperature and we can see from the Fig. (2) that τ value changes by minimal factor but with a significant chance of the v_{ni} the phase velocity of the mode change abruptly. Now Fig. (3) reveals the same variation for the phase velocity against v_{ni} and η_i as in the graph first of the article for τ and η_i.

3 Solitary waves

Now to obtain a nonlinear structure in the ITG driven mode (i.e., solitary and shock waves). We compare the next higher power of ϵ in the magnetohydrodynamics equations (such as in the continuity equation, momentum equation, energy balancing equation, and Poisson equation). We obtained linear and nonlinear differential equations in the form

$$\partial_\xi N^{(2)} - \frac{\tau \mathbf{v}_{ni}}{u}\partial_\xi \Phi^{(2)} - \tau \mathbf{v}_{ni}\partial_\ell \Phi^{(1)} - \frac{1}{2}\frac{\rho_i^2 \tau^{-1}}{u^2}\partial_\xi^3\left(T^{(1)} + N^{(1)} + \Phi^{(1)}\right) + \frac{1}{u}\partial_\xi v_{ix}^{(2)} = 0, \tag{17}$$

$$-\partial_\xi v_{ix}^{(2)} + \frac{v_{ix}^{(1)}}{u}\partial_\xi v_{ix}^{(1)} + \frac{c_s^2}{u}\partial_\xi\left[\Phi^{(2)} + \tau^{-1}\left(T^{(2)} + N^{(2)}\right)\right] + c_s^2\partial_\ell\left[\Phi^{(1)} + \tau^{-1}\left(T^{(1)} + N^{(1)}\right)\right] = 0, \tag{18}$$

$$-\partial_\xi T^{(2)} + \frac{2}{3}\partial_\xi N^{(2)} = \tau\left(\eta_i - \frac{2}{3}\right)\mathbf{v}_{ni}\left(\frac{1}{u}\partial_\xi \Phi^2 + \partial_\ell \Phi^1\right), \tag{19}$$

$$\frac{1}{u^2\alpha_1}\partial_\xi^2 \Phi^1 = (N^2 - \Phi^2), \tag{20}$$

where, $N^{(1)}$, $N^{(2)}$ are the normalized ion-number density of order first and second, $\Phi^{(1)}$, $\Phi^{(2)}$ are the normalized perturbed potential of order first and second, $T^{(1)}$, $T^{(2)}$ are the normalized ion-temperature of order first and second, v_{ix}, $v_{ix}^{(1)}$ are the ion-drift x-component of order first and second, v_{ni} ion-number density drift, u phase velocity of the mode, ρ_i ion gyro-radius, c_s acoustic speed, η_i ion-temperature gradient coefficient, $\alpha_1 = (4\pi e^2 n_{io})/T_e$, and $\tau = T_{eo}/T_{io}$. Now, combining Eqs. (17)-(20) we get the following nonlinear Korteweg-de-Vries (KdV) type of equation as

$$A_1\partial_\ell \Phi^1 + A_2\Phi^1\partial_\xi \Phi^1 + A_3\partial_\xi^3 \Phi^1 = 0, \tag{21}$$

where $A_1 = \left\{\tau \mathbf{v}_{ni} + u\,(1 + \tau \mathbf{v}_{ni}) - \frac{2c_s^2}{u^2}\left(\eta_i - \frac{2}{3}\right)\mathbf{v}_{ni} + \frac{c_s^2}{u}\left(1 + \frac{5\tau^{-1}}{3}\right)\right\}$, $A_2 = -u\,(u - \tau \mathbf{v}_{ni})^2$ and $A_3 = \left\{\frac{u}{\alpha_1} + \frac{1}{2}\rho_i^2\tau^{-1}u\left(\frac{8}{3} - \tau\left(\eta_i - \frac{2}{3}\right)\frac{\mathbf{v}_{ni}}{u}\right) + \frac{5}{3}\frac{c_s^2\tau^{-1}}{u^3\alpha_1}\right\}$. Dividing both sides of Eq. (21) by A_1 coefficient we get

$$\partial_\ell \Phi^1 + A\Phi^1\partial_\xi \Phi^1 + B\partial_\xi^3 \Phi^1 = 0, \tag{22}$$

where $A = \frac{A_2}{A1}$ and $B = \frac{A_3}{A1}$. The solution of Eq. (22) can be written (using a new variable as $\Omega = \xi - u\ell$ where u is the speed of the solitory waves in the ITG mode) as

$$\Phi = \Phi_0 \sec h^2\left[\frac{\Omega}{W}\right], \tag{23}$$

where $\frac{3u}{A} = \Phi_0$ and $\sqrt{\frac{4B}{u}} = W$.

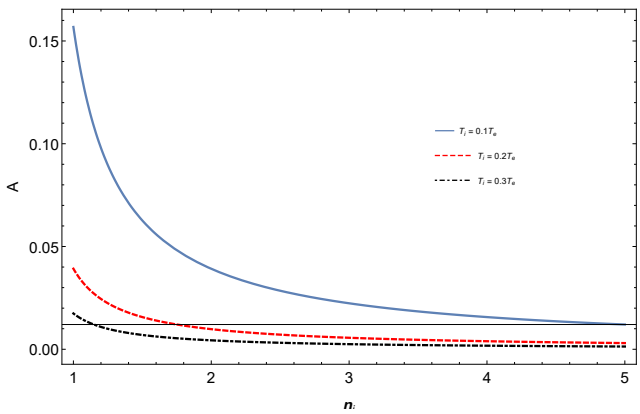

Figure 4. ITG driven mode KDV equation nonlinear coefficient versus η_i. under the effect of ion to electron temperature ratio.

Figs. (4) and (5) show that the nonlinear A and dispersion B coefficients of the kdv equation become smaller in value with the ion to electron temperature ratio T_i/T_e of the electron-ion plasma. So, we can observe the effects of different plasma parameters on the nonlinear and dispersion coefficients that will affect the magnitude as well as the sign of the coefficients hence the solitary and shock wave structure in the plasma can be changed from the compressional to the refractional type of soliton/shock.

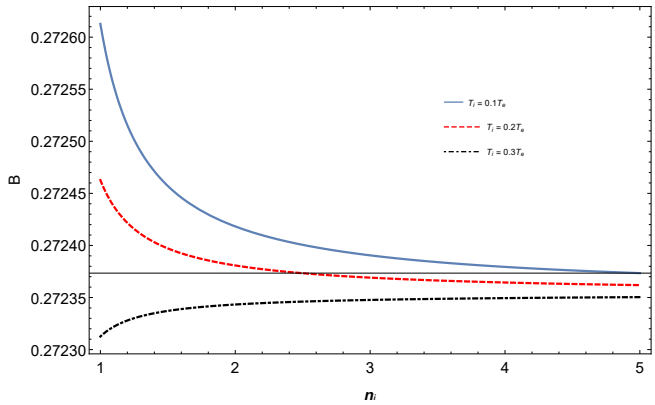

Figure 5. ITG driven mode KDV equation dispersion coefficient versus η_i under the effect of ion to electron temperature ratio.

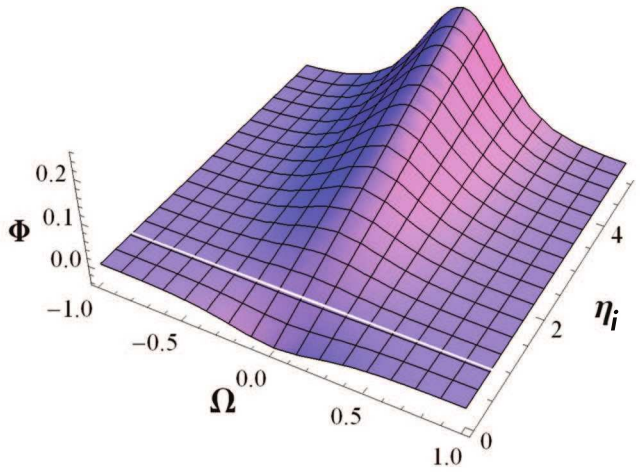

Figure 6. ITG driven mode solitary wave potential against the phase of the soliton η and η_i.

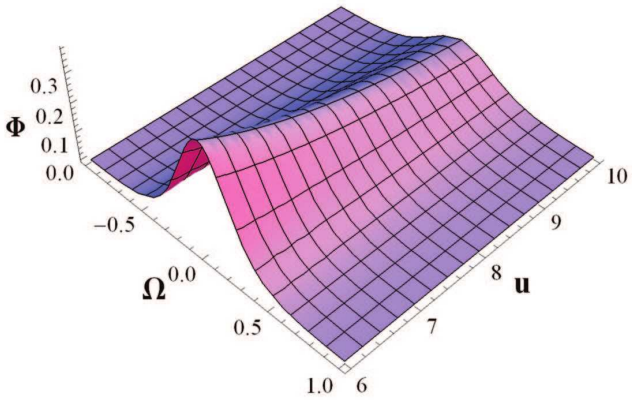

Figure 7. ITG driven mode solitan potential against phase of the soliton Ω and τ.

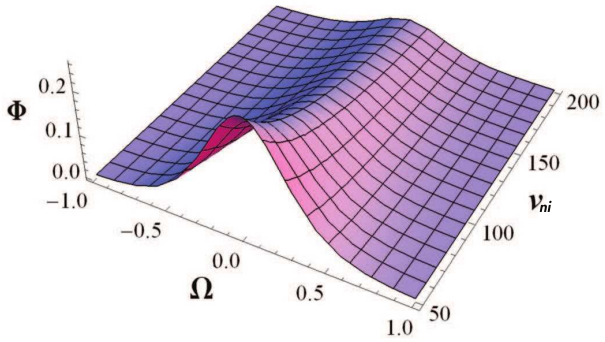

Figure 8. ITG driven mode solitary wave potential against phase of the soliton Ω and ν_{ni}.

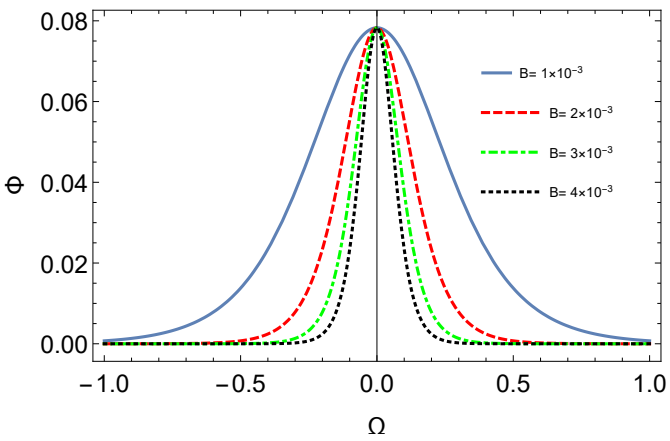

Figure 9. ITG driven mode solitary wave potential against phase of the soliton Ω.

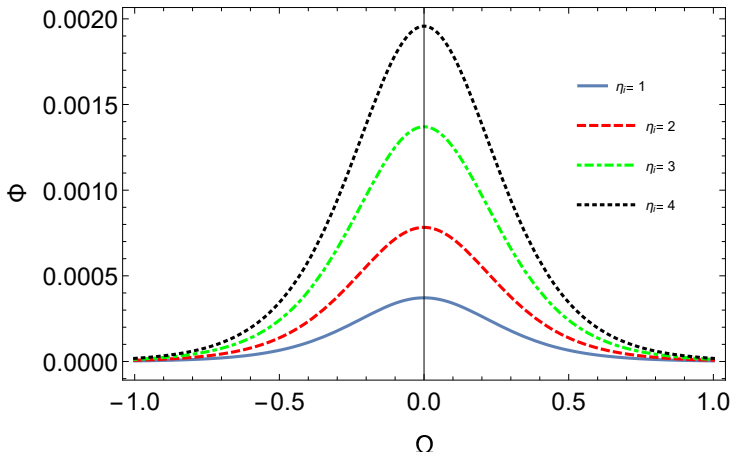

Figure 10. ITG driven mode solitary wave potential against phase of the soliton Ω.

That observation shows that both types of solitary waves can exist in the ITG mode at the low value of η_i−mode plasma a depth type of solitary waves are generated. In contrast, for $\eta_i \geq 1$ hump type of solitary waves are generated in the plasma it depends on the sign of the nonlinear coefficient of the KdV type of equation for a low value of ion temperature gradient coefficient its value is negative so refractive solitary waves are produced. Still, when the ion temperature gradient coefficient value is more significant than one, the compressive type of solitary waves is generated in the plasma. Also, dispersive properties of the solitary waves increase with the lowering of the η_i value while its amplitude is decreased by decreasing η_i value. Fig.(7) has been sketched among the soliton potential Φ against the soliton phase Ω, and its phase velocity u, which show that the solitary wave potential enhances in amplitude for low phase velocity while diminishing for the high phase velocity and also the dispersion properties of the soliton increases with the high phase velocity of the solitary waves in the electron-ion plasma. Fig. (8) is the graph of solitary wave potential against its phase and ion number density drift vni that shows the same situation as the previous graph i.e., with the drift velocity of the ion number density soliton potential decreasing in amplitude but its dispersive properties increases. Maybe the decrease in the amplitude of the solitary wave is due to the ion temperature and greater ion number density of the plasma because these plasma parameters can change its viscosity and bring more dissipation in the plasma. In Fig. (9) we have investigated the solitary wave potential against its phase Ω , which shows that the amplitude of the solitary wave is independent of the external magnetic field applied to the ITG mode driven electron-ion magnetoplasma. Still, the dispersion properties of the small amplitude solitary waves decrease with the background magnetic field's strength. While Fig. (9) shows the relation of the solitary waves against the soliton phase, with the ion temperature coefficient η_i the amplitude of the solitary wave becomes enhanced, and the dispersion properties of the waves is also increased with η_i. We can obtain the electric field from the solitary wave potential using a basic definition, i.e., $E = -\nabla\Phi$.

4 Shock wave

The shock wave can be generated in a fluid only when the dissipation effect is larger in a medium as compared to the dispersion. So, including the dissipative terms (i.e., $\eta_1 \frac{\partial^2 v_i}{\partial x^2}$) in the ion momentum equation, we will get a nonlinear Burger-like differential equation whose solution gives us the shock structure in the medium

$$A_1 \partial_\ell \Phi^1 + A_2 \Phi^1 \partial_\xi \Phi^1 - A_4 \partial_\xi^2 \Phi^1 = 0. \tag{24}$$

$A_1 = \left\{ \tau \mathbf{v}_{ni} + u\,(1 + \tau \mathbf{v}_{ni}) - \frac{2c_s^2}{u^2} \left(\eta_i - \frac{2}{3}\right) \mathbf{v}_{ni} + \frac{c_s^2}{u} \left(1 + \frac{5\tau^{-1}}{3}\right) \right\}$,
$A_2 = -u(u - \tau \mathbf{v}_{ni})^2$, and
$A_4 = \eta_1 (u - \tau \mathbf{v}_{ni})$ dividing both sides of Eq. (24) we get the nonlinear partial differential equation in the form as

$$\partial_\ell \Phi^1 + A \Phi^1 \partial_\xi \Phi^1 - C \partial_\xi^2 \Phi^1 = 0, \tag{25}$$

where $A = \frac{A_2}{A_1}$ and $C = \frac{A_4}{A_1}$ the solution of Eq (25). By using a new variable as $\Omega = \xi - u\ell$ is given as

$$\Phi = \Phi_0 \left[1 - \tan h \left(\frac{\Omega}{\frac{4C}{u}} \right) \right], \tag{26}$$

here $\frac{u}{A} = \Phi_0$ and $\frac{4C}{u} = Z$.

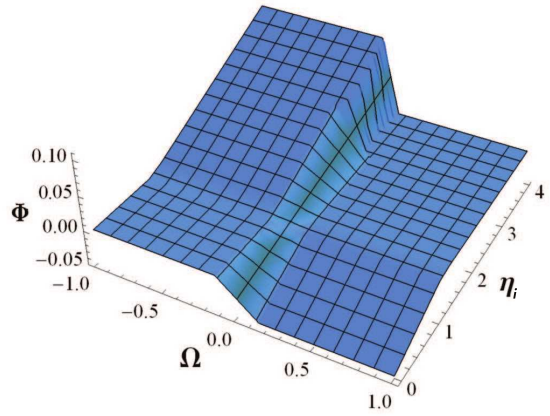

Figure 11. ITG driven mode Shock wave potential against phase of the shock Ω and η_i.

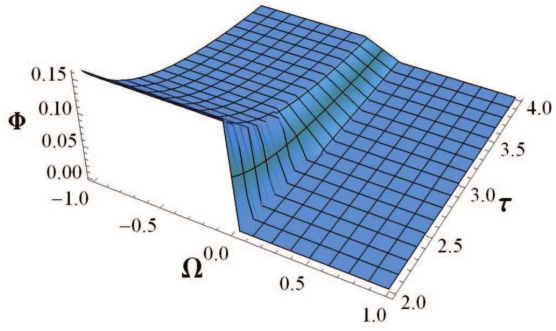

Figure 12. ITG driven mode Shock wave potential against phase of the shock Ω and τ.

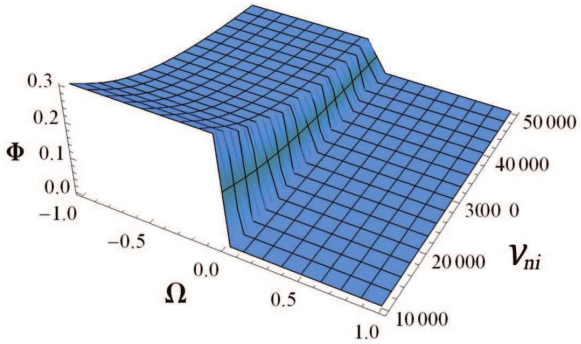

Figure 13. ITG driven mode Shock wave potential against phase of the shock Ω and ν_{ni}.

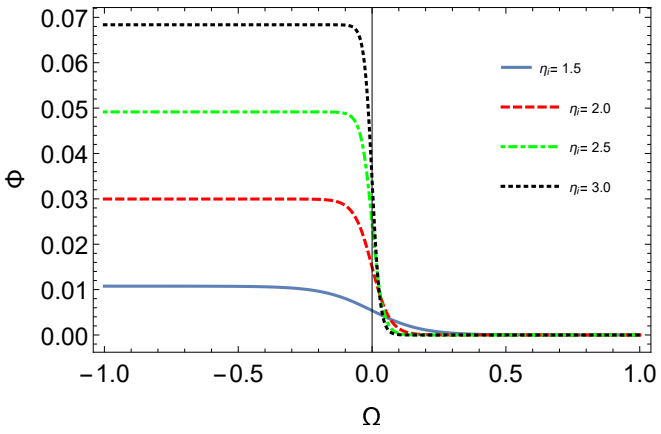

Figure 14. ITG driven mode Shock wave potential against phase of the shock Ω.

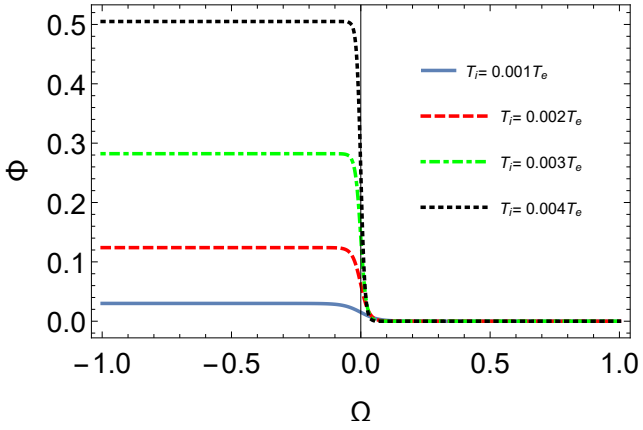

Figure 15. ITG driven mode Shock wave potential against phase of the shock Ω.

Fig. (11) is a graph of the shock wave potential against the phase of the shock and ion temperature gradient coefficient η_i. That figure gives a very interesting observation about the shock wave profile that for $\eta_i < 1$ then a rarefaction type of shock waves is produced in the plasma while compression type of the shock waves is produced when $\eta_i > 1$. Here the reason is the same as for the solitary waves because the nonlinear and dissipation coefficients of the kdv-Burger equation Eq. (25) can change its sing by changing the values of the plasma parameters. Fig. (12) reveals that the shock wave amplitude becomes smaller with the electron to ion temperature ratio, possibly, the high temperature species electron of the plasma presents opposition to the shock wave in the plasma due to the ion species. Similarly, the effect observed in Fig. (13) where the rise in the drift velocity of the ion can enlarge the shock wave amplitude and vice versa, may be the high ion number density in the fluid offer resistance to the production of the shock wave. In Fig. (14) we have compared the shock wave against its phase the 2-dimensional plot, here we can see that the amplitude of the shock with the ion temperature coefficient η_i increases and the same variation observed in Fig. (15) for the shock wave potential against its phase for the different values of the ion to electron temperature ratios, here we see the vibration of the shock wave amplitude is larger as compare to the previous Fig. (14). We have used the following parameters in analyzing the linear dispersion relation, nonlinear shock and solitory wave $n = 10^{14} cm^{-3}$, $B_0 = 1 \times 10^{-4}$, $T_i = 0.1T_e$, $n_p = 0.001n_e$, $\eta_i = 2$, $c_s = 10^6 \frac{cm}{s}$, ion gyro-frequency $\omega_{ci} = 10^4 \frac{rad}{s}$, in ξ-coordinates $u = 10^6 \frac{cm}{s}$, $\alpha = 0.1 rad$. These values are in agreement with the previous literature [13, 15, 17, 33, 35].

5 Conclusion

We have studied here the linear and nonlinear properties related to the ion temperature gradient (ITG) driven mode in the electron-ion plasma. Ions are observed to have dynamics while electrons follow the Maxwellian distribution in our consideration. We have derived the linear and nonlinear ITG modes by using a set of MHD equations for electron-ion plasma and then using the reduction perturbation method to derive the phase velocity for the mode that was independent of the wavenumber k of the wave, as has been shown in the calculation. Then we obtained a nonlinear structure in the form of solitary and shock waves in the same electron-ion magneto-plasma. We have shown in our calculation that different parameters like ion temperature, ion number density, magnetic field, etc., can affect the phase velocity as well as the shock and solitary waves in the electron-ion plasma.

Abbreviations

Electron temperature gradient (ETG), ion temperature gradient (ITG), Reduction Perturbation Method (RPM), electron-positron-ion (e-p-i), homotopy perturbation method (HPM), reduction perturbation method (RPT), Korteweg–De Vries (kdv), Magneto–hydrodynamics (MHD)

Declarations

Consent for publication

Not applicable.

Conflicts of interest

The authors declare that they have no known competing financial interests or personal relationships that could have appeared to influence the work reported in this paper.

Funding

Not applicable.

Author's contributions

Aziz Khan: Supervision, Validation, Conceptualization, Methodology, Software. Abbas Khan: Writing-Original draft preparation, methodology. Muhammad Sinan: Visualization, Methodology, Investigation, Software, Writing-Reviewing and Editing. All authors discussed the results and contributed to the final manuscript.

Acknowledgements

Not applicable.

References

[1] Goertz, C.K. Dusty plasmas in the solar system. *Reviews of Geophysics*, 27(2), 271-292, (1989). [CrossRef]
[2] Havnes, O., Melandsø, F., La Hoz, C., Aslaksen, T.K., & Hartquist, T. Charged dust in the Earth's mesopause; effects on radar backscatter. *Physica Scripta*, 45(5), 535, (1992). [CrossRef]
[3] Horanyi, M., & Mendis, D.A. The effects of electrostatic charging on the dust distribution at Halley's comet. *The Astrophysical Journal*, 307, 800-807, (1986).
[4] Rudakov, L.I., & Sagdeev, R.D.Z. On the instability of a nonuniform rarefied plasma in a strong magnetic field. *In Soviet Physics Doklady*, 6, 415, (1961, November).
[5] Coppi, B., Rosenbluth, M.N., Sagdeev, R.Z. Instabilities due to Temperature Gradients in Complex Magnetic Field Configurations. *The Physics of Fluids*, 10(3), 582-587, (1967). [CrossRef]
[6] Horton Jr, W., Choi, D.I., & Tang, W.M. Toroidal drift modes driven by ion pressure gradients. *The Physics of Fluids*, 24(6), 1077-1085, (1981). [CrossRef]
[7] Pogutse, P.O. *In Soviet Physics Doklady*. 25, 498, (1967).
[8] Hahm, T.S., & Tang, W.M. Properties of ion temperature gradient drift instabilities in H-mode plasmas. *Physics of Fluids B: Plasma Physics*, 1(6), 1185-1192, (1989). [CrossRef]
[9] Guzdar, P.N., Chen, L., Tang, W.M., & Rutherford, P.H. Ion-temperature-gradient instability in toroidal plasmas. *The Physics of Fluids*, 26(3), 673-677, (1983). [CrossRef]
[10] Jerman, A., Anderson, D., & Weiland, J. Chemiluminescent determination of adenosine, inosine, and hypoxanthine/xanthine. *Nucl. Fusion*, 27, 6, (1987).
[11] Shukla, P.K. Study of toroidal ion temperature gradient electrostatic drift waves. *Physica Scripta*, 42(6), 725, (1990). [CrossRef]
[12] Shukla, P.K., & Weiland, J. Ion-temperature-gradient driven drift vortex in an inhomogenous magnetic field. *Physics Letters A*, 136(1-2), 59-62, (1989). [CrossRef]
[13] Zakir, U., Haque, Q., Qamar, A., & Mirza, A.M. Ion-temperature-gradient driven modes in dust-contaminated plasma with nonthermal electron distribution and dust charge fluctuations. *Astrophysics and Space Science*, 350(2), 565-572, (2014). [CrossRef]
[14] Adnan, M., Mahmood, S., & Qamar, A. Coupled ion acoustic and drift waves in magnetized superthermal electron-positron-ion plasmas. *Physics of Plasmas*, 21(9), 092119, (2014). [CrossRef]
[15] Zakir, U., Haque, Q., Imtiaz, N., & Qamar, A. Dust acoustic and drift waves in a non-Maxwellian dusty plasma with dust charge fluctuation. *Journal of Plasma Physics*, 81(6), (2015). [CrossRef]
[16] Shukla, P.K., & Stenflo, L. Periodic structures on an ionic-plasma-vacuum interface. *Physics of plasmas*, 12(4), 044503, (2005). [CrossRef]
[17] Zakir, U., Adnan, M., Haque, Q., Qamar, A., & Mirza, A.M. Ion temperature gradient mode driven solitons and shocks. *Physics of Plasmas*, 23(4), 042104, (2016). [CrossRef]
[18] Mirza, A.M., Masood, W., Iqbal, J., & Batool, N. Toroidal ion-temperature-gradient driven vortices in an inhomogeneous magneto-plasma with non-Maxwellian electrons. *Physics of Plasmas*, 22(9), 092313, (2015). [CrossRef]

[19] Temerin, M., Cerny, K., Lotko, W., & Mozer, F.S. Observations of double layers and solitary waves in the auroral plasma. *Physical Review Letters*, 48(17), 1175, (1982). [CrossRef]
[20] Boström, R., Gustafsson, G., Holback, B., Holmgren, G., Koskinen, H., & Kintner, P. Characteristics of solitary waves and weak double layers in the magnetospheric plasma. *Physical review letters*, 61(1), 82, (1988). [CrossRef]
[21] Block, L.P., & Fälthammar, C.G. The role of magnetic-field-aligned electric fields in auroral acceleration. *Journal of Geophysical Research: Space Physics*, 95(A5), 5877-5888, (1990). [CrossRef]
[22] Nielsen, A.H., Rasmussen, J.J., & Schmidt, M.R. Self-organization and coherent structures in plasmas and fluids. *Physica Scripta*, 1996(T63), 49, (1996). [CrossRef]
[23] Sabry, R., Moslem, W.M., Haas, F., Ali, S., & Shukla, P.K. Nonlinear structures: Explosive, soliton, and shock in a quantum electron-positron-ion magnetoplasma. *Physics of Plasmas*, 15(12), 122308, (2008). [CrossRef]
[24] Oraevskii V.N., Tasso H. & Wobig H. (1984). Plasma Physics and Controlled Nuclear Fussion Research. *International Atomic Energy Agency Vienna*.
[25] Horton, W. Nonlinear drift waves and transport in magnetized plasma. *Physics Reports*, 192(1-3), 1-177, (1990). [CrossRef]
[26] Tasso, H. On drift wave spectra in 1D and 2D. *Il Nuovo Cimento B (1971-1996)*, 109(2), 207-209, (1994). [CrossRef]
[27] Meiss, J.D., & Horton, W. Fluctuation spectra of a drift wave soliton gas. *The Physics of Fluids*, 25(10), 1838-1843, (1982). [CrossRef]
[28] Salat, A. Is the temperature gradient or the derivative of the density gradient responsible for drift solitons?. *Plasma physics and controlled fusion*, 32(14), 1337, (1990). [CrossRef]
[29] Lashkin, V.M. Stable three-dimensional Langmuir vortex soliton. *Physics of Plasmas*, 27(4), 042106, (2020). [CrossRef]
[30] Khan, M.Y., Manzoor, M.Q., Ul Haq, A., & Iqbal, J. Effect of entropy on anomalous transport in ITG-modes of magneto-plasma. *Nuclear Fusion*, 57(4), 046027, (2017). [CrossRef]
[31] Yaqub Khan, M., & Iqbal, J. Effect of entropy on soliton profile in ITG driven magneto-plasma. *Physics of Plasmas*, 24(8), 082514, (2017). [CrossRef]
[32] Iqbal, J., & Khan, M.Y. Soliton formation in ion temperature gradient driven magneto-plasma. *Physics of Plasmas*, 24(4), 042506, (2017). [CrossRef]
[33] Khan, A., Zakir, U., & Haque, Q. Ion Temperature Gradient Mode–Driven Solitary and Shock Waves in Electron-Positron-Ion Magnetized Plasma. *Brazilian Journal of Physics*, 50(4), 430-437, (2020). [CrossRef]
[34] Rehan, M., Zakir, U., Haque, Q., & Hameed, G. Ion temperature gradient mode driven solitons and shocks in superthermal plasma. *Chinese Journal of Physics*, 68, 908-918, (2020). [CrossRef]
[35] Khan, A., Zakir, U., Haque, Q. & Qamar, A. Role of entropy in η_i-mode driven nonlinear structures obtained by homotopy perturbation method in electron–positron–ion plasma. *Zeitschrift für Naturforschung A*, 76(8), 671-681, (2021). [CrossRef]
[36] Zabusky, N.J. A synergetic approach to problems of nonlinear dispersive wave propagation and interaction. *In Nonlinear partial differential equations*. Academic Press. 223-258, (1967). [CrossRef]
[37] Zabusky, N.J., & Kruskal, M.D. Interaction of "solitons" in a collisionless plasma and the recurrence of initial states. *Physical review letters*, 15(6), 240, (1965). [CrossRef]
[38] Taniuiti, T., & Wei, C.C. *Journal of the Physical Society of Japan*, 10, 941-952, (1968).
[39] Washimi, H., & Taniuiti, T. Propagation of Ion-Acoustic Solitary Waves of Small Amplitude. *Physical Review Letters*, 17(19), 996-1002, (1966). [CrossRef]
[40] Kuninaka, H., & Hayakawa, H. Contact and Quasi-Static Impact of a Dissipationless Mechanical Model. *Journal of the Physical Society of Japan*, 75, 1-5, (2006).
[41] Zakharov, V.E. & Kuznetsov, E.A. Three-dimensional solitons. *Soviet Physics—JETP*, 39(2), 285-290, (1974).
[42] Saleem, H., & Batool, N. Nonlinear structures of drift waves in pair-ion-electron plasmas. *Physics of Plasmas*, 16(2), 022302, (2009). [CrossRef]
[43] Weiland, J. Collective Modes in Inhomogeneous Plasma: Kinetic and Advanced Fluid Theory IOP. *Bristol, Philadelphia*, (2000).
[44] Washimi, H., & Taniuti, T. Propagation of ion-acoustic solitary waves of small amplitude. *Physical Review Letters*, 17(19), 996, (1966).

Mathematical Modelling and Numerical Simulation with Applications (MMNSA) (http://www.mmnsa.org)

Mathematical Modelling and Numerical Simulation with Applications, 2022, 2(1), 13–25

https://www.mmnsa.org
ISSN Online: 2791-8564 / Open Access
https://doi.org/10.53391/mmnsa.2022.01.002

RESEARCH PAPER

Second-grade fluid with Newtonian heating under Caputo fractional derivative: analytical investigations via Laplace transforms

Ndolane Sene[1,*,‡]

[1]Department of Mathematics, Cheikh Anta Diop University, BP 5683 Dakar Fann, Senegal

[*]Corresponding Author
[‡]ndolanesene@yahoo.fr (Ndolane Sene)

Abstract

In this paper, we consider the constructive equations of the fractional second-grade fluid. The considered fluid model is described by the Caputo derivative. The problem consists to determine the exact analytical solution using the Laplace transform method. The influence of the order of the used fractional operator has been presented in this paper. We also analyze the influence of the Prandtl number in the dynamics of the temperature distribution according to the variation of the order of the Caputo derivative. The impact of the second-grade parameter and the Grashof number in the dynamics of the velocity has been presented and discussed. The influences of the parameters used in the modeling have been interpreted in terms of a fractional context. In general, it is shown that the order of the fractional operator influences the diffusivity of the considered fluid. This influence can cause an increase or decrease in the temperature and velocity distributions. The main findings of the paper have been illustrated using the graphical representations of the considered distributions according to the order of the fractional operator.

Key words: Second-grade fluid; Grashof number; Prandtl number; Laplace transforms
AMS 2020 Classification: 26A33; 35C15; 42A38; 35K57

1 Introduction

The field of fractional calculus and its application has grown many attractions these last decade. There exist nowadays many theories and applications related to the field of fractional calculus [1]. The attraction of this new field is due to the memory effect and the heredity noticed in the fractional operators. We have many fractional operators as the Caputo derivative and the Riemann-Liouville derivative which are known as the fractional derivative with singular kernels [2, 3]. We have also the so-called Atangana-Baleanu fractional operator and the Caputo-Fabrizio derivative which are known as the fractional operators with non-singular kernels [4, 5]. These singular and non-singular derivatives appear in many papers with applications to physical modeling [2, 6, 7], biological modeling [8, 9, 10, 11, 12, 13, 14], sciences and engineering modeling [15, 16, 17, 18, 19], mathematical physics modeling [20, 21, 22, 23, 24, 25, 26], physics modeling [24, 27] and others domains [28, 29, 30, 31, 32]. The field of fractional calculus is interesting but there also exist many questions without responses. The following questions are asked in the field of fractional calculus: what is a fractional operator, why fractional operators, what are the advantages, and the motivations of using the fractional operators? Some of these questions have responses but some of them are still without concrete responses. Modeling fluid, and nanofluid with fractional operators have attracted many authors these last decade. The investigations related to modeling fluid and nanofluid with the fractional operators can be found in the following papers [20, 33, 34].
The literature concerning the fluid and second-grade fluid models with fractional operators is long. In this part, we recall the literature review. In [33], the authors have proposed a model related to free convection flow near a vertical plate described by Caputo derivative and have considered its solution via Laplace transform method. In [20], the authors have taken into account the analytical solutions via Laplace

➤ **Received:** 13.12.2021 ➤ **Revised:** 16.01.2022 ➤ **Accepted:** 22.01.2022 ➤ **Published:** 26.01.2022

transform for a fractional double convection problem of fractional viscous fluid particularly described by a Caputo fractional operator. Ali et al. in [35] have proposed the exact analytical solution of MHD free convection flow of generalized Walters'-B fluid model described by new fractional operator namely Caputo-Fabrizio derivative. In [36], the authors have obtained a solution for the free convection flow of generalized Jeffrey fluid described by the Caputo-Fabrizio fractional. In [15], the authors have used the Laplace transform to get the exact analytical solution of the MHD flow of water-based Brinkman type nanofluid. In [37], the authors have used the Caputo derivative to model heat and mass transport of differential type fluid and have examined the exact analytical solution using the Laplace transform method. In [38], the authors have studied the unsteady MHD free convection flow of Casson fluid past over an oscillating vertical plate embedded in a porous medium, the Laplace transform has been used in such paper to get the analytical solutions. In [21], the authors have proposed a comparative study between the Caputo-Fabrizio derivative and Atangana-Baleanu derivative in modeling the generalized Casson fluid model with heat generation and chemical reaction. In [28], Tahir et al. have proposed the analytical solution of the heat transfer flow of Maxwell fluid described by Caputo-Fabrizio time-fractional derivative. In [39], the authors have studied the MHD flow of a Casson fluid over an exponentially shrinking sheet, the analytical solution of the proposed model has been proposed via the Adomian Decomposition Method. In the same direction of investigations related to the determination of the analytical solution using Laplace transform for the models with integer-order derivative see in [40].

In this work, we focus on the analytical solutions of the constructive equations of the second-grade fluid model described by the Caputo fractional operator. We use in this paper the Laplace transform method for getting the analytical solution. The advantages of the present investigations are we use the resolution of second-order differential equations which are not difficult to be performed. The second advantage of the present paper is the analytical solutions can be rewritten using the exponential function, the Mittag-Leffler function, the wright functions, and the Gaussian error function. The memories effect present in the Caputo derivative will also be an advantage in the present paper because the order of the Caputo derivative will play accelerations or retardation effect on the dynamics of the velocity and the temperature distribution of the considered model.

The contents of the present paper are structured as follows. In Section 2, we try to recall the fractional operators most used in the literature of fractional calculus. It will permit the readers to be familiarized with the fractional operator. In Section 3, we describe the fractional model using the Caputo derivative. In Section 4, we give the approaches to get the analytical solutions using the Laplace transform method. Note that the Laplace transform of the Caputo derivative will be frequently used. Discussion and the interpretations of the influences of the parameters utilized in the modeling have been provided in Section 5. We finish the paper with final remarks in Section 6.

2 Fractional operators

This section is devoted to giving the definitions of the fractional operators and the functions which will be used in this investigation. For present works, we need the Caputo fractional operator, the Riemman-Liouville integral, the derivatives with son singular kernels, the Mittag-Leffler functions, the wright function, and others. We also will recall the Laplace transform of the Caputo derivative because this tool is fundamental in our investigations regarding the method utilized in the present paper. The Riemann-Liouville integral is described in the following definition.

Definition 1 *[2, 3] The representation of the Riemann-Liouville integral of a considered function* $g : [0, +\infty[\longrightarrow \mathbb{R}$ *can be expressed as the following form*

$$\left(I^{\alpha} g\right)(t) = \frac{1}{\Gamma(\alpha)} \int_0^t (t-s)^{\alpha-1} g(s) ds, \tag{1}$$

the $\Gamma(...)$ *denotes the Gamma function and with order* α *verifying the condition that* $\alpha > 0$.

The Riemann-Liouville integral has its associated fractional derivative known as the Riemann-Liouville derivative. We give its definition in the following definition. This definition can be found in many papers in the literature.

Definition 2 *[2, 3] The representation of the Riemann-Liouville derivative of the considered function* $g : [0, +\infty[\longrightarrow \mathbb{R}$, *of order* α *as the form*

$$D^{\alpha} g(t) = \frac{1}{\Gamma(1-\alpha)} \frac{d}{dt} \int_0^t g(s) (t-s)^{-\alpha} ds, \tag{2}$$

the time $t > 0$, *is the order of the operator and satisfies the condition that* $\alpha \in (0, 1)$ *and* $\Gamma(...)$ *represents the Gamma Euler function.*

The Riemann-Liouville derivative has an increasing reputation in the problems related to the existence and the uniqueness, the stability analysis of the fractional differential problems. In modeling real words problems the initial condition makes this operator very limited because the real-world problems' initial conditions are not compatible with the Riemann-Liouville derivative. Therefore this derivative is not used in modeling biological models, fractional chaotic systems, and other real applications. The Caputo derivative is adequate in modeling real word problems and is defined in the following definition.

Definition 3 *[2, 3] We denote the Caputo fractional derivative with the considered function* $g : [0, +\infty[\longrightarrow \mathbb{R}$, *of order* α *as the following representation*

$$D^{\alpha} g(t) = \frac{1}{\Gamma(1-\alpha)} \int_0^t \frac{dg}{ds} (t-s)^{-\alpha} ds, \tag{3}$$

with $t > 0$, *and the order of the derivative obeys to the assumption that* $\alpha \in (0, 1)$ *and* $\Gamma(...)$ *is the Gamma Euler function.*

The Caputo derivative is the most used derivative in the literature of fractional calculus. The motivation is due to the fact that this derivative is compatible with the initial conditions used in modeling real word problems. In this paper the Laplace transform method is used for getting the exact analytical solutions, therefore we define in the following line the Laplace transform of the Caputo derivative. We have the

following representation [2, 3]

$$\mathcal{L}\left\{\left(D_c^{\alpha} g\right)(t)\right\} = s^{\alpha}\mathcal{L}\left\{g(t)\right\} - s^{\alpha-1}g(0). \tag{4}$$

with the order α satisfies the condition that $\alpha \in (0,1)$. The symbol $\mathcal{L}$ denotes the Laplace transform. The Laplace transform in Eq. (4) will play a fundamental role in the present investigation.
Before closing this section, we recall the definitions of the fractional operators with non-singular kernels. These derivatives have many applications these decades and many papers have been written to illustrate the applications of these derivatives in modeling physics, biology models, science, and engineering.

Definition 4 *[5] We represent by the following equation of the Caputo-Fabrizio derivative of the function* $g : [0, +\infty[\longrightarrow \mathbb{R}$*, of order* α *in the following term*

$$D^{\alpha,CF} g(t) = \frac{CF(\alpha)}{1-\alpha}\int_0^t g'(s)\exp\left(-\frac{\alpha}{1-\alpha}(t-s)\right)ds, \tag{5}$$

where the following the condition $t > 0$*, the order of the fractional derivative obeys to* $\alpha \in (0,1)$ *and* $CF(...)$ *denotes the normalization term and respects to the condition* $CF(0) = CF(1) = 1$*.*

Definition 5 *[4] The definition of the Atangana-Baleanu derivative of the function* $g : [0, +\infty[\longrightarrow \mathbb{R}$*, of order* α*, that is*

$$D^{\alpha,AB} g(t) = \frac{AB(\alpha)}{1-\alpha}\int_0^t g'(s)E_{\alpha}\left(-\frac{\alpha}{1-\alpha}(t-s)^{\alpha}\right)ds, \tag{6}$$

respecting the condition that $t > 0$*, the order of the fractional derivative* $\alpha \in (0,1)$ *and* $AB(...)$ *is the normalization term and obeys to the condition* $AB(0) = AB(1) = 1$*.*

We finish this section by recalling the special functions which are used to express the analytical exact solutions in this paper. We have the Mittag-Leffler function and the wright function represented in the following expressions [33],

$$E_{\alpha,\beta}(x) = \sum_{k=0}^{\infty}\frac{x^k}{\Gamma(\alpha k+\beta)}, \tag{7}$$

with $\alpha > 0$, $\beta \in \mathbb{R}$ and $x \in \mathbb{C}$, and we define the Wright function [33] with three parameters as the following

$$\phi(\beta, -\sigma, x) = \sum_{n=0}^{\infty}\frac{x^n}{\Gamma(n+1)\Gamma(\beta-\sigma n)}, \tag{8}$$

with the following conditions $\sigma \in (0,1)$, $\beta \in \mathbb{R}$ and $x \in \mathbb{C}$.

3 Fractional model under Caputo derivative

This section is devoted to the presentation of the second-grade fluid model subject of our investigations. To arrive at our end, we describe the following procedure. The sketch of modeling can be found in the literature in the following papers [20, 33], the significant difference in the model is the initial condition which play important role in the form of the analytical solutions. We take the plate vertical at x-direction and we take y-direction perpendicular to the plane generated by the plane. We consider that at the initial time, then the fluid and the plate are at rest to the constant temperature T_{∞}. At starting time, we suppose that the heat transfer from the plate to the considered fluid is proportional to a local surface temperature denoted by T. For the rest of our modeling, we consider the use of the Boussinesq approximation and then we get the following partial differential equations

$$\frac{\partial u}{\partial t} = \left(\nu + \frac{\alpha_1}{\rho}\frac{\partial}{\partial t}\right)\frac{\partial^2 u}{\partial y^2} + g\beta(T - T_{\infty}), \tag{9}$$

$$\frac{\partial T}{\partial t} = \frac{\kappa}{\rho c_p}\frac{\partial^2 T}{\partial y^2}. \tag{10}$$

The initial and boundary conditions adopted in this present investigations are described as follows

$$v(u,0) = 0, \quad T(x,0) = T_{\infty}, \tag{11}$$

$$T(0,t) = 0, \quad T(0,t) = T_{\infty} + \left[T_w - T_{\infty}\right]\left[\frac{t}{t_0}\right]. \tag{12}$$

The problem consists to get the exact analytical solutions of the model (9)-(10), and then we need more simplifications of the previous model. Therefore we introduce the following changes variables

$$y^* = \frac{yh}{k}, \quad t^* = \frac{t}{\frac{1}{\nu\left(\frac{k}{h}\right)^2}}, \quad u^* = \frac{u}{\frac{g}{\nu\left(\frac{k}{h}\right)^2}}, \quad \psi^* = \frac{T - T_{\infty}}{T_{\infty}}, \tag{13}$$

$$Gr = \beta T_{\infty}, \quad Pr = \frac{\rho c_p}{\kappa}, \quad \beta^* = \frac{\alpha_1}{\rho}\left(\frac{h}{k}\right)^2. \tag{14}$$

We use the dimensionless variable described in Eq. (13) and Eq. (14) into Eq.(9) to Eq. (12), we get a more simplified form of the fluid model considered in this paper, it is represented by the following

$$\frac{\partial u}{\partial t} = \frac{\partial^2 u}{\partial y^2} + \beta \frac{\partial^3 u}{\partial t \partial y^2} + Gr\psi, \tag{15}$$

$$\frac{\partial \psi}{\partial t} = \frac{1}{Pr}\frac{\partial^2 \psi}{\partial y^2}. \tag{16}$$

with initial and boundaries dimensionless conditions given

$$u(y,0) = \psi(y,0) = 0, \tag{17}$$

$$u(0,t) = 0, \tag{18}$$

$$\psi(0,t) = t. \tag{19}$$

Replacing the integer-order derivative by the Caputo derivative in Eqs. (15)-(16) due to the memory effect and the heredity of the Caputo derivative and the generalization of the integer-order derivative to non-integer partial differential equations, we get the following model which will be the subject of our investigations

$$D_\tau^\alpha u = \frac{\partial^2 u}{\partial y^2} + \beta D^\alpha \left(\frac{\partial^2 u}{\partial y^2}\right) + Gr\psi, \tag{20}$$

$$D_\tau^\alpha \psi = \frac{1}{Pr}\frac{\partial^2 \psi}{\partial y^2}. \tag{21}$$

As initial and boundaries conditions which the velocity and the temperature satisfy, we consider the following relationships

$$u(y,0) = \psi(y,0) = 0, \tag{22}$$

$$u(0,t) = 0, \tag{23}$$

$$\psi(0,t) = t. \tag{24}$$

Furthermore, we add the supplementary conditions that both the temperature (ψ) and the velocity (v) converge to zero when the y tends to infinity. In the following Table 1, the names of the parameters used in our modeling described in this Section 3 are provided.

Table 1. Parameter descriptions

Parameters	*Descriptions*
Pr	Prandtl number
Gr	Grashof number
c_p	Heat at a constant pressure
g	Acceleration constant
β	Volumetric coefficient of thermal expansion
ν	Kinematics viscosity of the fluid
κ	Thermal conductivity of the fluid
α_1	Second grade parameter
ρ	Fluid density

4 Analytical approaches

In this section, we consider the initial and boundary conditions in Eqs. (22)-(24) to give the analytical solution of equations (20) and (21) via the Laplace transform method. The basic tool here is solving the second-order differential equations via the Laplace transform. The sketch of the proof consists in first getting the exact analytical solution of Eq. (21) and using this solution to determine also the analytical solution of Eq. (20).

Here we begin with Equation (21) under initial and boundary conditions described in Eqs. (22)-(24). Applying the Laplace transform to both sides of Eq. (21), we have that

$$s^\alpha \bar{\psi} - s^{\alpha-1}\psi(y,0) = \frac{1}{Pr}\frac{\partial^2 \bar{\phi}}{\partial y^2},$$

$$s^\alpha \bar{\psi} = \frac{1}{Pr}\frac{\partial^2 \bar{\psi}}{\partial y^2},$$

$$\frac{\partial^2 \bar{\psi}}{\partial y^2} - Prs^\alpha \bar{\psi} = 0. \tag{25}$$

Before continuing the resolution we also apply the Laplace transform to the boundary condition (24), we get that $\psi(0,s) = 1/s^2$. Then the

analytical solution of the second-order differential equation (21) in terms of Laplace transform is given as the following form

$$\bar{\psi}(x,s) = \frac{\exp\left[-x\sqrt{Prs^{\alpha}}\right]}{s^2}. \tag{26}$$

The determination of the inverse of the Laplace transform needs to use the called wright function. This function is recalled to the preliminary section. Then the inverse of the Laplace transform given by Eq. (26) is given by

$$\psi(x,t) = t\phi\left(2, -\alpha/2, -x\sqrt{Prt}^{-\alpha/2}\right). \tag{27}$$

We now consider a special case obtained when the order of the Caputo derivative converges to one, that is $\alpha = 1$. We repeat the procedure of the solution with Eq. (25). Let consider this equation with the case $\alpha = 1$, we have the following relationship

$$\bar{\psi}(x,s) = \frac{\exp\left[-x\sqrt{Prs}\right]}{s^2}. \tag{28}$$

The final step of the resolution consists to apply the inverse of the Laplace transform to both sides of Eq. (28), it yields that

$$\psi(x,t) = \left(\frac{x^2Pr}{2} + t\right) erfc\left(\frac{x\sqrt{Pr}}{2\sqrt{t}}\right) - \frac{x\sqrt{Prt}}{2\sqrt{\pi}} \exp\left(-\frac{x^2Pr}{4t}\right). \tag{29}$$

The second step of the determination of the exact analytical solution of our model will finish with the resolution of Eq. (20). The method is similar to the procedure previously applied with the temperature distribution. In the step of the determination of the velocity, we apply the Laplace transform to both sides of equation (20), we get that

$$\begin{aligned} s^{\alpha}\bar{u} - s^{\alpha-1}\bar{u}(y,0) &= (1+\beta s^{\alpha})\frac{\partial^2\bar{u}}{\partial x^2} + Gr\bar{\psi}, \\ s^{\alpha}\bar{u} &= (1+\beta s^{\alpha})\frac{\partial^2\bar{u}}{\partial y^2} + Gr\bar{\psi}, \\ \frac{\partial^2\bar{u}}{\partial y^2} - \frac{s^{\alpha}}{1+\beta s^{\alpha}}\bar{u} &= -\frac{Gr}{1+\beta s^{\alpha}}\frac{\exp\left[-x\sqrt{Prs^{\alpha}}\right]}{s^2}. \end{aligned} \tag{30}$$

The solution in terms of the Laplace transform of the second-order differential equation (30) with initial and boundary conditions taken into account is given by the following relationship

$$\bar{u}(x,s) = C\left[\frac{\exp\left[-x\sqrt{Prs^{\alpha}}\right]}{s^{\alpha}} - \frac{\exp\left[-x\sqrt{\frac{s^{\alpha}}{1+\beta s^{\alpha}}}\right]}{s^{\alpha}}\right], \tag{31}$$

where C is given as

$$C = -Gr\left[\frac{s^{-2}}{1+\beta s^{\alpha}} - \frac{Prs^{-2}}{\beta Prs^{\alpha} + Pr - 1}\right]. \tag{32}$$

To get the analytical solution, we have to apply the inverse of the Laplace transform to both sides of Eq.(31) and use the convolution product properties. We have the following analytical solution

$$u(x,t) = \int_0^t a(t-\tau)\left(b(x,\tau) - c(x,\tau)\right)d\tau. \tag{33}$$

For obtaining the form of function, we apply the inverse of Laplace transform of the function C, we need to utilize the Mittag-Leffler function. That is

$$a(x,t) = -\frac{Grt^{1+\alpha}}{\beta}\left[E_{\alpha,2+\alpha}\left(-\frac{1}{\beta}t^{\alpha}\right) - E_{\alpha,2+\alpha}\left(-\frac{Pr-1}{\beta Pr}t^{\alpha}\right)\right]. \tag{34}$$

We continue with the inverse of the Laplace transform of the function represented as the following form

$$\bar{b}(x,s) = \frac{\exp\left[-x\sqrt{Prs^{\alpha}}\right]}{s^{\alpha}}, \tag{35}$$

which needs some manipulations. The inverse of the Laplace transform is given by the following relationship

$$b(x,t) = t^{\alpha-1}\phi\left(\alpha, -\alpha/2, -y\sqrt{Prt}^{-\alpha/2}\right). \tag{36}$$

We finish this procedure of inverse of the Laplace transforms by inverting the function defined as the form

$$\bar{c}(x,s) = \frac{\exp\left[-x\sqrt{\frac{s^{\alpha}}{1+\beta s^{\alpha}}}\right]}{s^{\alpha}}, \tag{37}$$

and then propose the analytical solution of the Eq. (20). The inverse of the Laplace transform to both sides of Eq. (37) is given by the following representation

$$c(x,t) = \int_0^{\infty} m(y,u)\phi\left(0,-\alpha,ut^{-\alpha}\right)du, \tag{38}$$

where

$$m(y,u) = 1 - \frac{2}{\pi\sqrt{\beta}}\int_0^{\infty}\frac{\sin(yu)}{u\left(u^2+1/\sqrt{\beta}\right)}\exp\left(\frac{-u^2ut}{\beta\left(u^2+1/\sqrt{\beta}\right)}\right)du. \tag{39}$$

We now consider a special case obtained when the order of the Caputo derivative converges to 1 that is $\alpha = 1$, and the parameter $\beta = 0$. Note that the parameter β is zero when $\alpha_1 = 0$ in Eq. (14). In this case, we consider the Laplace transform described in Eq. (31) with the previous assumptions, there is

$$\bar{u}(x,s) = \frac{Gr}{Pr-1}\left[\frac{\exp\left[-x\sqrt{s}\right]}{s^3} - \frac{\exp\left[-x\sqrt{Prs}\right]}{s^3}\right]. \tag{40}$$

We now apply the inverse of the Laplace transform, which is given by the following analytical form

$$u(x,t) = \frac{Gr}{Pr-1}\int_0^t (t-\tau)\,erfc\left(\frac{x}{2\sqrt{\tau}}\right)d\tau \tag{41}$$

$$- \frac{Gr}{Pr-1}\int_0^t (t-\tau)\,erfc\left(\frac{x\sqrt{Pr}}{2\sqrt{\tau}}\right)d\tau. \tag{42}$$

Before closing this section it is important to mention the method to get the Nusselt number. This number is obtained with the temperature distribution by the following formula

$$Nu = -\mathcal{L}^{-1}\left[\lim_{x\to 0}\frac{\partial\bar{\phi}(x,s)}{\partial x}\right]. \tag{43}$$

5 Discussion on the findings

In this section, we discuss the findings of the paper. We analyze the impact of the Caputo order derivative in the dynamics of the temperature and the velocity distribution. The impact of the Prandtl number, Grashof number, time, and second-grade coefficient will be discussed in terms of the variation of the Caputo derivative in detail.

The temperature distribution

We begin the discussion with the temperature distribution. In this part, the fractional-order and the Prandtl number will be analyzed in terms of their impacts on the dynamics of the temperature distribution. In this section, we consider Eq. (27) in the graphical representations. We fix the time $t = 0.6$ for Figures 1a, 1b and $t = 10$ for Figures 2a, 2b, and also we consider different values of the order of the Caputo fractional operator. We have the following graphical results: We now analyze the behaviors of the dynamics presented in the previous figures. Let the time t less than one, this assumption corresponds to Figures 1a, 1b. We observe that when the order of the Caputo derivative increases with the increase of the state y, we note that, the temperature distribution decreases. These dynamics can be explained by the fact for a short time the accumulation of the memory and heredity affects the diffusivity of the considered model. The increase in the order increases the diffusivity which generates a decrease in the temperature of the fluid. The second conclusion concerns that when the time is greater than 1, see Figures 2a, 2b, in this case, the accumulation of the memory effect and heredity makes the system more diffusive which affects the temperature distribution 2a, 2b and causes its increase. In the considered cases in this part, we note that the Caputo derivative plays an acceleration effect in the dynamics of the temperature distribution.
Let us now analyze the impact of the Prandtl number in the dynamics of the considered fluid particularly on the temperature distribution. We take two different times $t = 0.6$ for Figures 3a, 3b, and $t = 10$ for Figures 4a, 4b, different orders of the derivative have been considered and we increase the values of the Prandtl number. We have the following graphical representations:

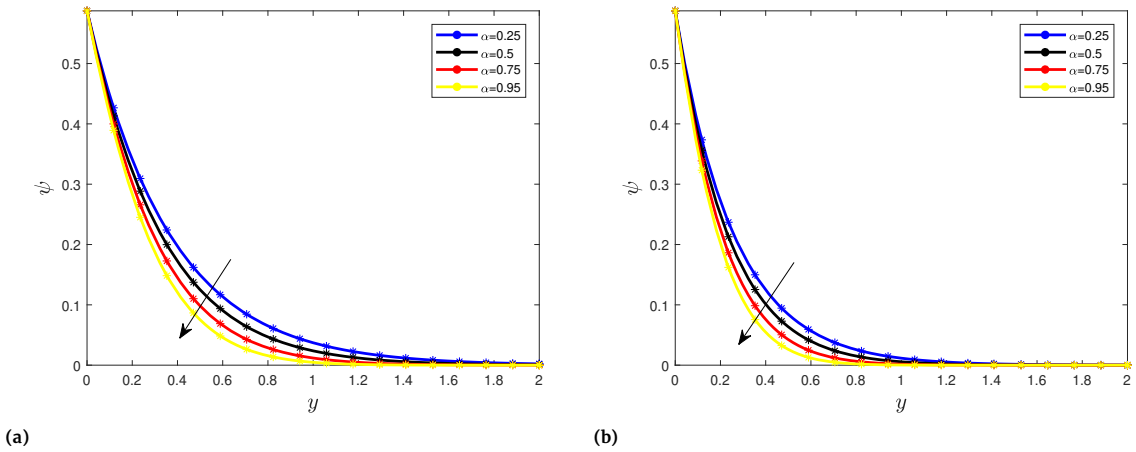

Figure 1. Temperature distribution for different values of the order α with $Pr = 6$ (a) and $Pr = 12$ (b).

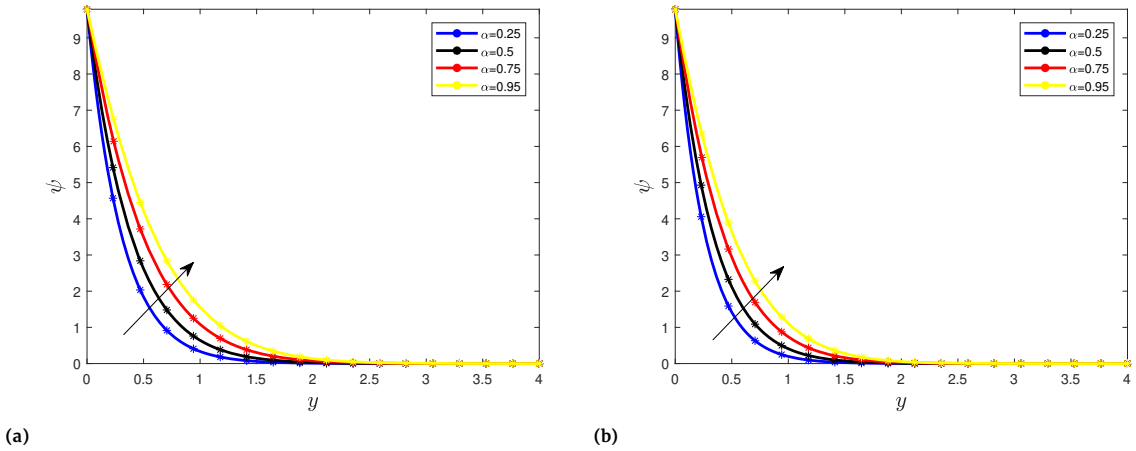

Figure 2. Temperature distribution for different values of the order α with $Pr = 6$ (a) and $Pr = 12$ (b).

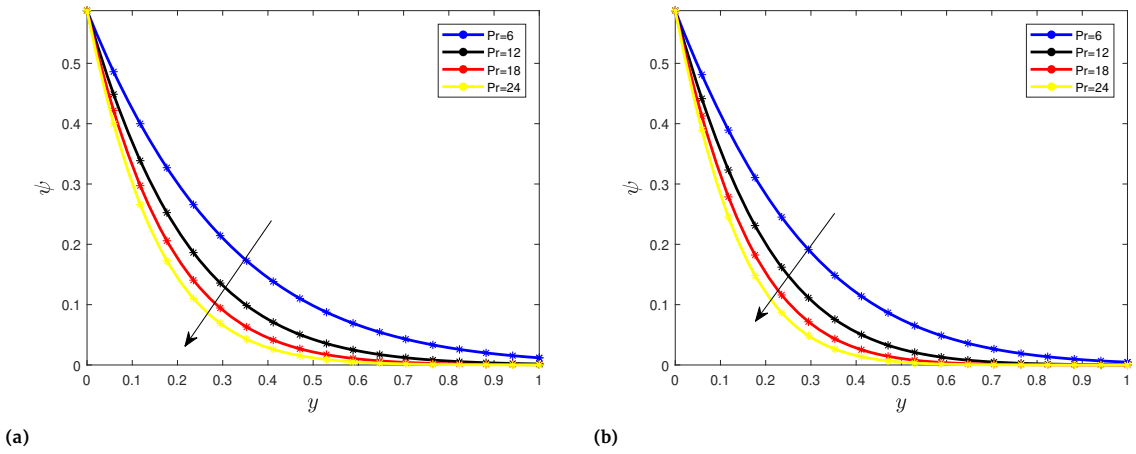

Figure 3. Temperature distribution for different values of the Prandtl number with $\alpha = 0.75$ (a) and $\alpha = 0.95$ (b).

The graphical representations 3a, 3b, 4a, 4b inform us that when the values of the *Pr* increase then temperature distribution decreases as well. These behaviors can be explained by the fact when the order of the fractional operator increases and the Prandtl number increases then the diffusivity of the system is reduced, thus its impact on the temperature distribution decreases. Let us now see what happens

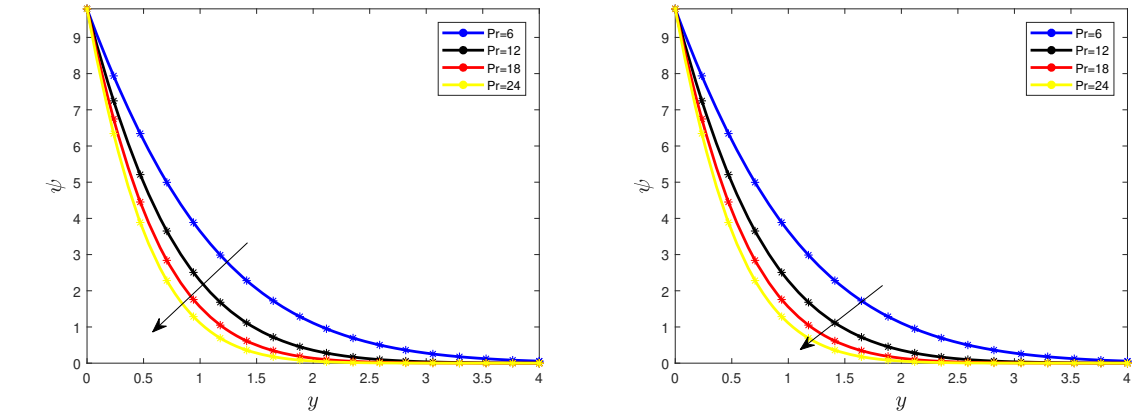

Figure 4. Temperature distribution for different values of the Prandtl number with $\alpha = 0.75$ (a) and $\alpha = 0.95$ (b).

with the temperature distribution when the time varies significantly and the Prandtl number increases. We have the following figures

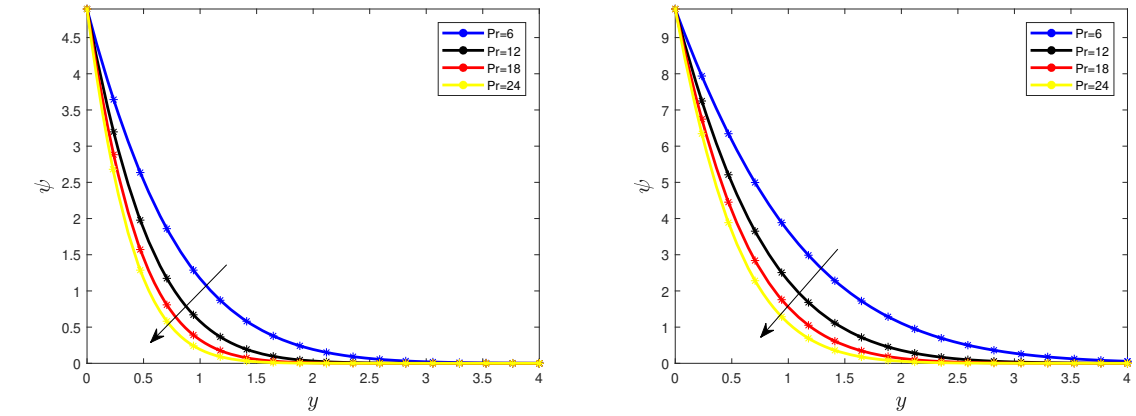

Figure 5. Temperature distribution for different values of *Pr* with $t = 5$ (a) and $t = 10$.

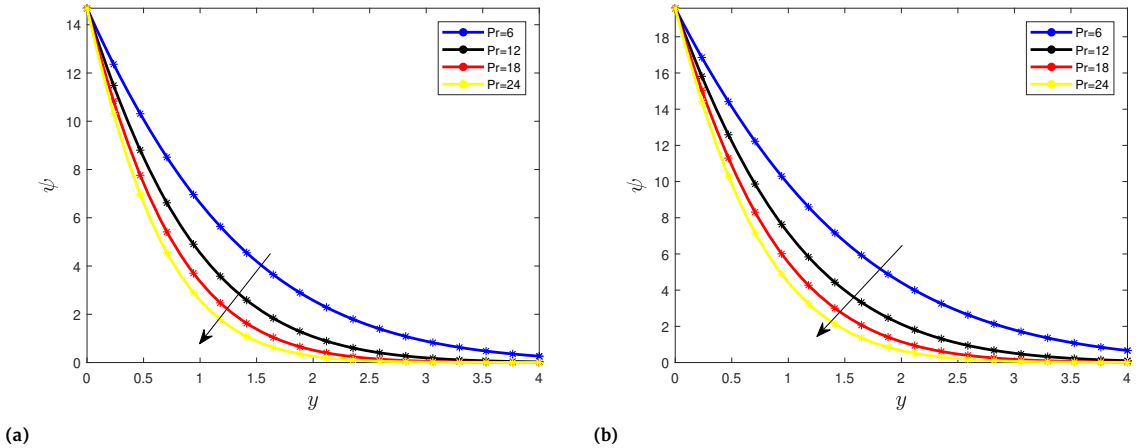

Figure 6. Temperature distribution for different values of *Pr* with $t = 15$ (a) and $t = 20$ (b).

Comparing the Figures 5a, 5b, 6a, 6b, we can observe that when the Pr number increases, then the temperature distribution decreases. In conclusion, the time does not play a role if the Prandtl number increase. For all considered times the increase of the Prandtl number generates a decrease in the temperature distribution.

The velocity distribution

In this sub-section, we try to explain and interpret the dynamics generated by the velocity. We first consider analyzing the influence of the fractional-order in the dynamics. In this section, we condition Eq. (33) in the graphical representations. In the second part, we will analyze the influence of the parameters as the Grashof number Gr and second-grade coefficient β. Let us represent the dynamics of the velocity for different values of the Caputo fractional order in the following Figures 7a, 7b, 8a, 8b. Let that $t = 5$, we have the following graphics 7a, 7b, 8a, 8b for the velocity The influence of the order of the fractional derivative is analyzed in terms of the variation of the

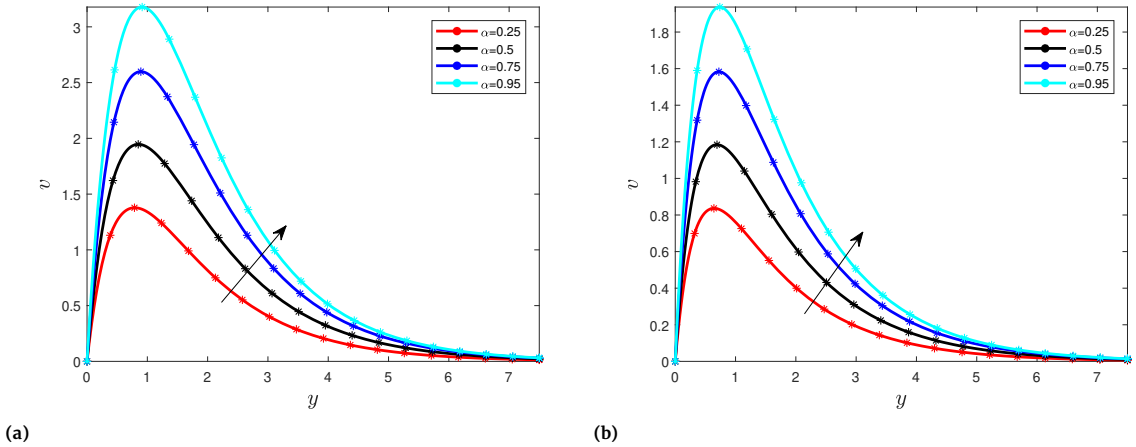

Figure 7. Velocity distribution for different values of the order α with $Pr = 5$ (a) $Pr = 10$ (b).

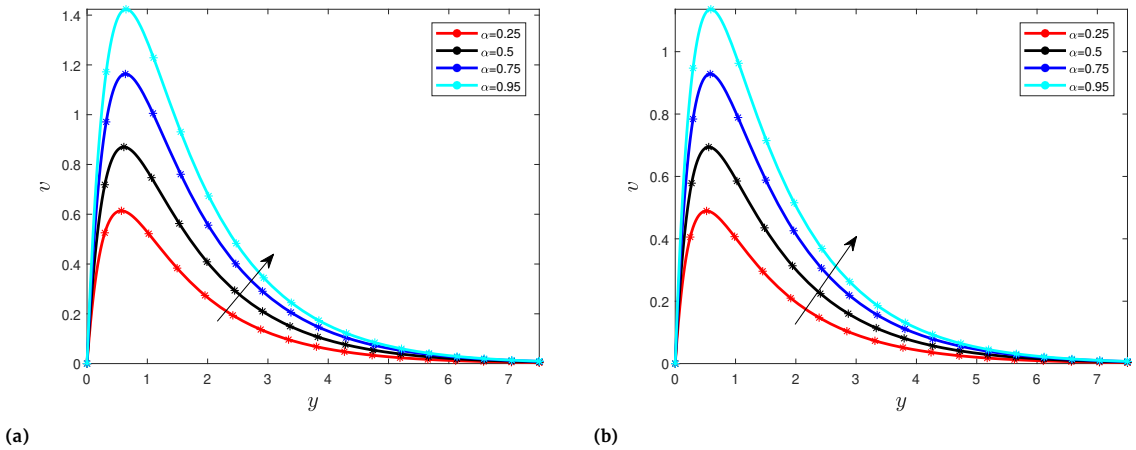

Figure 8. Velocity distribution for different values of the order α with $Pr = 15$ (a) $Pr = 20$ (b).

Prandtl number. We observe that when the order of the Caputo derivative increases, the velocity increases. Thus, the fractional-order has an acceleration effect in the present case. We also notice that when the Prandtl number increase, the velocity decreases, as well. The Prandtl number has the same influence on the temperature distribution and the velocity. We now consider a second case where the time is greater than 1 ($t = 10$) and the variation of the Grashof number is assumed. We have the following graphical representations 9a, 9b, 10a, 10b We can observe that with the previous figures the increase in the order of the Caputo derivative generates an increase in the velocity. The increase in the velocity is due to the fact when time is greater than 1, the Caputo derivative generates accumulation in the memory which causes an increase in the value of the velocity. Here, the order of the Caputo derivative has an acceleration effect. We analyze the impact of the Grashof number Gr, we can do it by analyzing the previous Figures 9a, 9b, 10a, 10b. Comparing the Figures 9a, 9b, 10a, 10b, we can observe that when the Grashof number increases, it generates an increase in velocity. This increase in the velocity is explained by the fact that when the Grashof number increases then we have increased in the thermal buoyancy force. Let us now analyze the second-grade parameter. We have

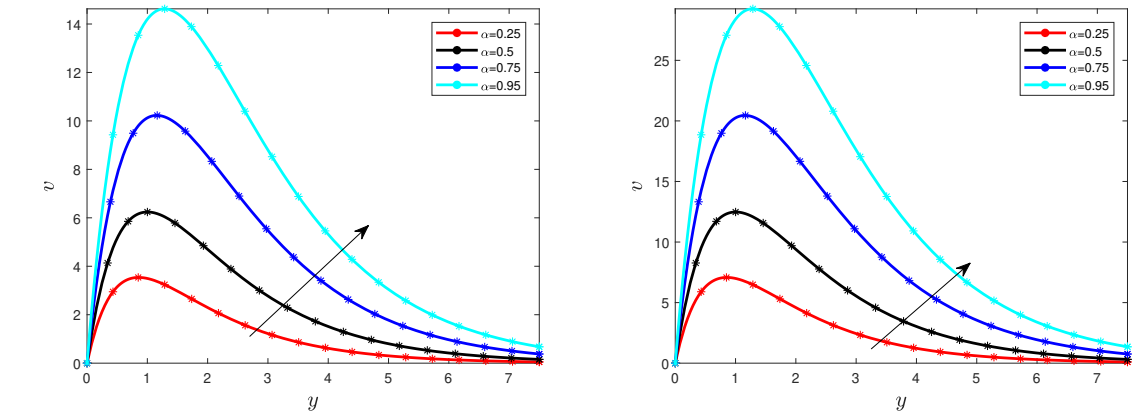

Figure 9. Velocity distribution for different values of the order α with $Gr = 5$ and $Gr = 10$.

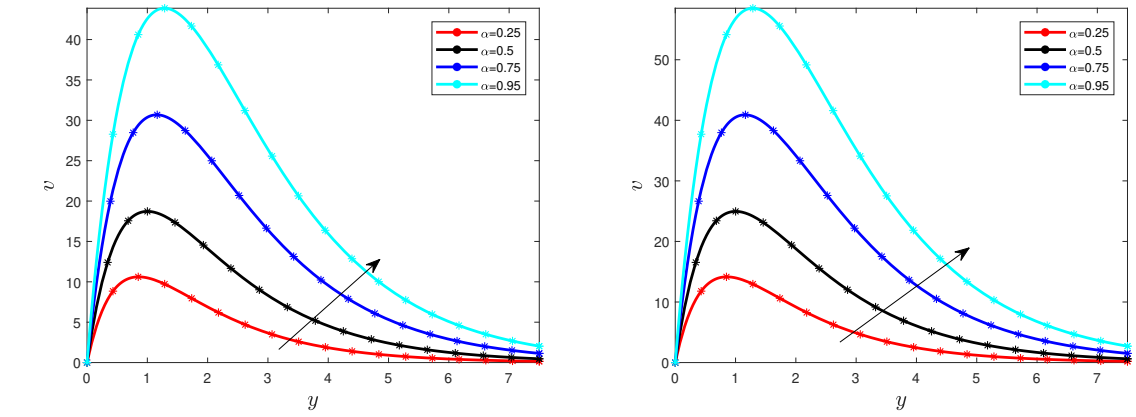

Figure 10. Velocity distribution for different values of the order α with $Gr = 15$ and $Gr = 20$.

the following graphical representations 11a, 11b, 12a, 12b, when the value of the second-grade parameter increases When we compare the

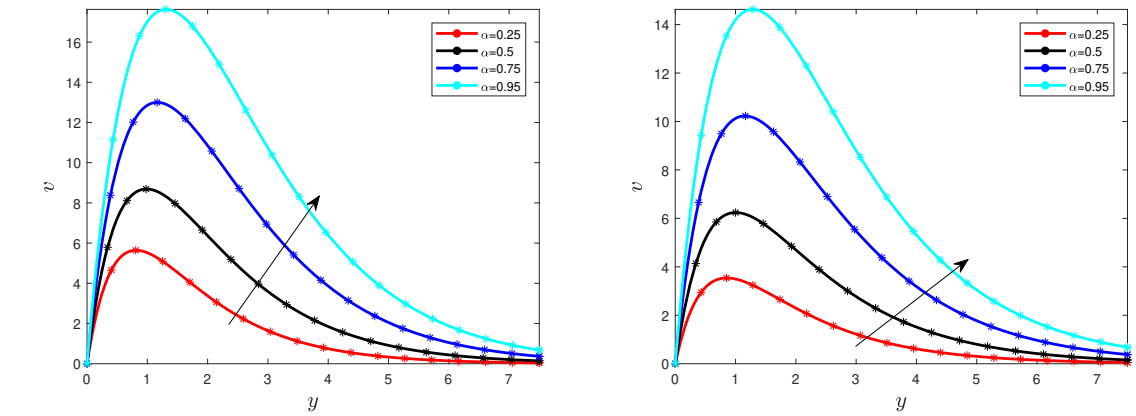

Figure 11. Velocity distribution for different values of the order α with $\beta = 0$ (a) and $\beta = 0.5$ (b).

values of the velocity in Figures 11a, 11b, 12a, 12b, we notice when the values of the second-grade parameter increase, then the velocity

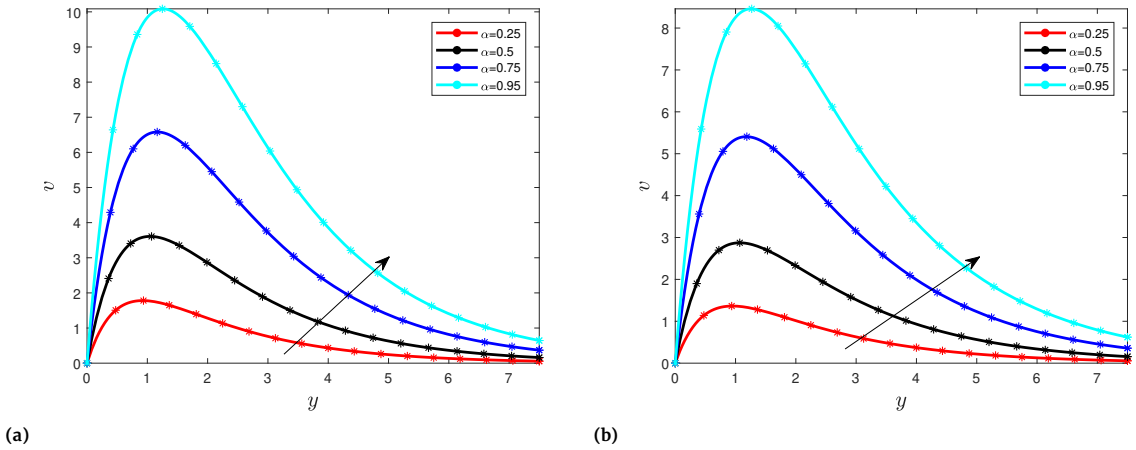

Figure 12. Velocity distribution for different values of the order α with $\beta = 0$ (a) and $\beta = 0.5$ (b).

decreases as well. This behavior is explained by the fact that in general the increase of the thickness of the boundary layer is caused by the decrease of the second-grade parameter. The present investigations are similar to the investigations provided by Shah et al in [41]. In [41], the authors consider the same model addressed in this paper with the fractional derivative with the exponential kernel. The main findings in [41] and the results in the present paper are in good agreement. One of the main advantages of the present investigations regarding the investigations existing in the literature is here we use the Caputo derivative which the application of the Laplace transform and its inverse is trivial and the expressions of the exact analytical solutions of the considered fluid model can easily be expressed via Gaussian function, exponential function, and Mittag-Leffler function.

6 Conclusion

In this paper, we have discussed the exact analytical solutions of the second-grade fluid model described by the Caputo fractional operator. After modeling the fluid model via Caputo derivative, we have used the Laplace transform method to get the analytical solutions of the fluid model considered in this paper. Many results have been proposed in our present paper. As the first finding, the order of the fractional operator accelerates the diffusion or can have a retardation effect, that depends on the considered time. We noticed that with the increase of the Prandtl number for a specific order of the Caputo derivative then the temperature distribution of the considered fluid decreases as well. This behavior is due to the reduction of the diffusivity as previously mentioned in the paper. Note that with the increase of Grashof number Gr then it generates an increase in the velocity distribution of the considered fluid. For the future direction of researches, the same second-grade fluid model can be described by non-singular fractional operators as the Atangana-Baleanu derivative and Caputo-Fabrizio derivative, and getting the exact solutions with the Laplace transform constitutes an open problem and can be focused on in the future.

Declarations

Consent for publication

Not applicable.

Conflicts of interest

The author declares that he has no known competing financial interests or personal relationships that could have appeared to influence the work reported in this paper.

Funding

The author declares that there is no funding source for the reported research.

Author's contributions

The research was carried out by the author and he accepts that the contributions and responsibilities belong to the author.

Acknowledgements

Not applicable.

References

[1] Atangana, A., & Araz, S.İ. Extension of Atangana-Seda numerical method to partial differential equations with integer and non-integer order. *Alexandria Engineering Journal*, 59(4), 2355-2370, (2020). [CrossRef]

[2] Kilbas, A.A., Srivastava, H.M., & Trujillo, J.J. *Theory and applications of fractional differential equations* (Vol. 204). Elsevier, (2006).

[3] Podlubny, I. *Fractional Differential Equations*, Academic Press: New York, NY, USA (1999).

[4] Atangana, A. & Baleanu, D. New fractional derivatives with nonlocal and non-singular kernel: theory and application to heat transfer model, *Thermal Sciences*, 20(2), 763-769, (2016). [CrossRef]

[5] Caputo, M., & Fabrizio, M. A new definition of fractional derivative without singular kernel. *Progress in Fractional Differentiation and Applications*, 1(2), 1-13, (2015). [CrossRef]

[6] Saad, K.M., Baleanu, D., & Atangana, A. New fractional derivatives applied to the Korteweg–de Vries and Korteweg–de Vries–Burger's equations. *Computational and Applied Mathematics*, 37(4), 5203-5216, (2018). [CrossRef]

[7] Sene, N. Theory and applications of new fractional-order chaotic system under Caputo operator. *An International Journal of Optimization and Control: Theories & Applications (IJOCTA)*, 12(1), 20-38, (2022). [CrossRef]

[8] Wang, X., Wang, Z., Huang, X., & Li, Y. Dynamic analysis of a delayed fractional-order SIR model with saturated incidence and treatment functions. *International Journal of Bifurcation and Chaos*, 28(14), 1850180, (2018). [CrossRef]

[9] Qureshi, S., Yusuf, A., Shaikh, A.A., & Inc, M. Transmission dynamics of varicella zoster virus modeled by classical and novel fractional operators using real statistical data. *Physica A: Statistical Mechanics and its Applications*, 534, 122149, (2019). [CrossRef]

[10] Sene, N. Fractional SIRI Model with Delay in Context of the Generalized Liouville–Caputo Fractional Derivative. *In Mathematical Modeling and Soft Computing in Epidemiology* (pp. 107-125). CRC Press, (2020).

[11] Shen, Z.H., Chu, Y.M., Khan, M.A., Muhammad, S., Al-Hartomy, O.A., & Higazy, M. Mathematical modeling and optimal control of the COVID-19 dynamics. *Results in Physics*, 31, 105028, (2021). [CrossRef]

[12] Li, X.P., Wang, Y., Khan, M.A., Alshahrani, M.Y., & Muhammad, T. A dynamical study of SARS-COV-2: A study of third wave. *Results in Physics*, 29, 104705, (2021). [CrossRef]

[13] Yavuz, M., & Sene, N. Stability analysis and numerical computation of the fractional predator–prey model with the harvesting rate. *Fractal and Fractional,* 4(3), 35, (2020). [CrossRef]

[14] Kumar, P., & Erturk, V.S. Dynamics of cholera disease by using two recent fractional numerical methods. *Mathematical Modelling and Numerical Simulation with Applications*, 1(2), 102-111, (2021). [CrossRef]

[15] Ali, F., Gohar, M., & Khan, I. MHD flow of water-based Brinkman type nanofluid over a vertical plate embedded in a porous medium with variable surface velocity, temperature and concentration. *Journal of Molecular Liquids*, 223, 412-419, (2016). [CrossRef]

[16] Abro, K.A. A fractional and analytic investigation of thermo-diffusion process on free convection flow: an application to surface modification technology. *The European Physical Journal Plus*, 135(1), 1-14, (2020). [CrossRef]

[17] Sene, N. Stability and Convergence Analysis of Numerical Scheme for the Generalized Fractional Diffusion-Reaction Equation. *In Advanced Numerical Methods for Differential Equations* (pp. 1-16). CRC Press, (2021).

[18] Hammouch, Z., Yavuz, M., & Özdemir, N. Numerical solutions and synchronization of a variable-order fractional chaotic system. *Mathematical Modelling and Numerical Simulation with Applications*, 1(1), 11-23, (2021). [CrossRef]

[19] Rashid, M., Kalsoom, A., Ghaffar, A., Inc, M., & Sene, N. A Multiple Fixed Point Result for-Type Contractions in the Partially Ordered-Distance Spaces with an Application. *Journal of Function Spaces*, 2022, 6202981, (2022). [CrossRef]

[20] Shah, N.A., Khan, I., Aleem, M., & Imran, M.A. Influence of magnetic field on double convection problem of fractional viscous fluid over an exponentially moving vertical plate: New trends of Caputo time-fractional derivative model. *Advances in Mechanical Engineering*, 11(7), 1-11, (2019). [CrossRef]

[21] Sheikh, N.A., Ali, F., Saqib, M., Khan, I., Jan, S.A.A., Alshomrani, A.S., & Alghamdi, M.S. Comparison and analysis of the Atangana–Baleanu and Caputo–Fabrizio fractional derivatives for generalized Casson fluid model with heat generation and chemical reaction. *Results in physics*, 7, 789-800, (2017). [CrossRef]

[22] Ahmad, H., Khan, T.A., Ahmad, I., Stanimirović, P.S., & Chu, Y.M. A new analyzing technique for nonlinear time fractional Cauchy reaction-diffusion model equations. *Results in Physics*, 19, 103462, (2020). [CrossRef]

[23] Yavuz, M., & Sene, N. Approximate solutions of the model describing fluid flow using generalized ρ-Laplace transform method and heat balance integral method. *Axioms,* 9(4), 123, (2020). [CrossRef]

[24] Li, J.F., Ahmad, I., Ahmad, H., Shah, D., Chu, Y.M., Thounthong, P., & Ayaz, M. Numerical solution of two-term time-fractional PDE models arising in mathematical physics using local meshless method. *Open Physics*, 18(1), 1063-1072, (2020). [CrossRef]

[25] Naik, P.A., Eskandari, Z., & Shahraki, H.E. Flip and generalized flip bifurcations of a two-dimensional discrete-time chemical model. *Mathematical Modelling and Numerical Simulation with Applications*, 1(2), 95-101, (2021). [CrossRef]

[26] Yavuz, M., & Sene, N. Fundamental calculus of the fractional derivative defined with Rabotnov exponential kernel and application to nonlinear dispersive wave model. *Journal of Ocean Engineering and Science,* 6(2), 196-205, (2021). [CrossRef]

[27] Panda, S.K., Ravichandran, C., & Hazarika, B. Results on system of Atangana–Baleanu fractional order Willis aneurysm and nonlinear singularly perturbed boundary value problems. *Chaos, Solitons & Fractals*, 142, 110390, (2021). [CrossRef]

[28] Tahir, M., Imran, M.A., Raza, N., Abdullah, M., & Aleem, M. Wall slip and non-integer order derivative effects on the heat transfer flow of Maxwell fluid over an oscillating vertical plate with new definition of fractional Caputo-Fabrizio derivatives. *Results in physics*, 7, 1887-1898, (2017). [CrossRef]

[29] Ahmad, I., Ahmad, H., Thounthong, P., Chu, Y.M., & Cesarano, C. Solution of multi-term time-fractional PDE models arising in mathematical biology and physics by local meshless method. *Symmetry*, 12(7), 1195, (2020). [CrossRef]

[30] Li, X.P., Gul, N., Khan, M.A., Bilal, R., Ali, A., Alshahrani, M.Y., ... & Islam, S. A new Hepatitis B model in light of asymptomatic carriers and vaccination study through Atangana–Baleanu derivative. *Results in Physics*, 29, 104603, (2021). [CrossRef]

[31] Nisar, K.S., Jothimani, K., Kaliraj, K., & Ravichandran, C. An analysis of controllability results for nonlinear Hilfer neutral fractional derivatives with non-dense domain. *Chaos, Solitons & Fractals*, 146, 110915, (2021). [CrossRef]

[32] Bonyah, E., Yavuz, M., Baleanu, D., & Kumar, S. A robust study on the listeriosis disease by adopting fractal-fractional operators. *Alexandria Engineering Journal*, 61(3), 2016-2028, (2022). [CrossRef]

[33] Vieru, D., Fetecau, C., & Fetecau, C. Time-fractional free convection flow near a vertical plate with Newtonian heating and mass

diffusion. *Thermal Science*, 19(1), 85-98, (2015). [CrossRef]
[34] Sene, N. Fractional diffusion equation with reaction term described by Caputo-Liouville generalized fractional derivative, *Journal of Fractional Calculus and Applications* 13(1), 42-57, (2022).
[35] Ali, F., Saqib, M., Khan, I., & Sheikh, N.A. Application of Caputo-Fabrizio derivatives to MHD free convection flow of generalized Walters'-B fluid model. *The European Physical Journal Plus*, 131(10), 1-10, (2016). [CrossRef]
[36] Saqib, M., Ali, F., Khan, I., Sheikh, N.A., & Jan, S.A.A. Exact solutions for free convection flow of generalized Jeffrey fluid: a Caputo-Fabrizio fractional model. *Alexandria engineering journal*, 57(3), 1849-1858, (2018). [CrossRef]
[37] Imran, M.A., Khan, I., Ahmad, M., Shah, N.A., & Nazar, M. Heat and mass transport of differential type fluid with non-integer order time-fractional Caputo derivatives. *Journal of Molecular Liquids*, 229, 67-75, (2017). [CrossRef]
[38] Khalid, A., Khan, I., Khan, A., & Shafie, S. Unsteady MHD free convection flow of Casson fluid past over an oscillating vertical plate embedded in a porous medium. *Engineering Science and Technology, an International Journal*, 18(3), 309-317, (2015). [CrossRef]
[39] Nadeem, S., Haq, R.U., & Lee, C. MHD flow of a Casson fluid over an exponentially shrinking sheet. *Scientia Iranica*, 19(6), 1550-1553, (2012). [CrossRef]
[40] Narahari, M., & Dutta, B.K. Effects of thermal radiation and mass diffusion on free convection flow near a vertical plate with Newtonian heating. *Chemical Engineering Communications*, 199(5), 628-643, (2012). [CrossRef]
[41] Shah, N.A., & Khan, I. Heat transfer analysis in a second grade fluid over and oscillating vertical plate using fractional Caputo–Fabrizio derivatives. *The European Physical Journal C*, 76(7), 1-11, (2016). [CrossRef]

Mathematical Modelling and Numerical Simulation with Applications (MMNSA) (http://www.mmnsa.org)

Mathematical Modelling and Numerical Simulation with Applications, 2022, 2(1), 26–40

https://www.mmnsa.org
ISSN Online: 2791-8564 / Open Access
https://doi.org/10.53391/mmnsa.2022.01.003

RESEARCH PAPER

Bi-dimensional crime model based on anomalous diffusion with law enforcement effect

Francisco Javier Martínez-Farías[1,*,‡], Anahí Alvarado-Sánchez[2,‡], Eduardo Rangel-Cortes[1,‡] and Arturo Hernández-Hernández[1,‡]

[1]Escuela Superior de Apan, Universidad Autónoma del Estado de Hidalgo, Carretera Apan-Calpulalpan Km 8, Col. Chimalpa, C.P 43920, Apan, Hidalgo, México, [2]Instituto de Ciencias Nucleares, Universidad Nacional Autónoma de México, Apdo. Postal 70-543, 04510, Cd.Mx., México

*Corresponding Author
‡francisco_martinez@uaeh.edu.mx (Francisco Javier Martínez-Farías); anahi_a.s@ciencias.unam.mx (Anahí Alvarado-Sánchez); eduardo_rangel@uaeh.edu.mx (Eduardo Rangel-Cortes); arturo_hernandez@uaeh.edu.mx (Arturo Hernández-Hernández)

Abstract

Several models based on discrete and continuous fields have been proposed to comprehend residential criminal dynamics. This study introduces a two-dimensional model to describe residential burglaries diffusion, employing Lévy flights dynamics. A continuous model is presented, introducing bidimensional fractional operator diffusion and its differences with the 1-dimensional case. Our results show, graphically, the hotspot's existence solution in a 2-dimensional attractiveness field, even fractional derivative order is modified. We also provide qualitative evidence that steady-state approximation in one dimension by series expansion is insufficient to capture similar original system behavior. At least for the case where series coefficients have a linear relationship with derivative order. Our results show, graphically, the hotspot's existence solution in a 2-dimensional attractiveness field, even if fractional derivative order is modified. Two dynamic regimes emerge in maximum and total attractiveness magnitude as a result of fractional derivative changes, these regimes can be understood as considerations about different urban environments. Finally, we add a Law enforcement component, embodying the "Cops on dots" strategy; in the Laplacian diffusion dynamic, global attractiveness levels are significantly reduced by Cops on dots policy but lose efficacy in Lévy flight-based diffusion regimen. The four-step Preditor-Corrector method is used for numerical integration, and the fractional operator is approximated, getting the advantage of the spectral methods to approximate spatial derivatives in two dimensions.

Key words: Residential burglary; Lévy flights; fractional operator; anomalous diffusion; hotspots; law enforcement
AMS 2020 Classification: 60K50; 26A33; 34D20

1 Introduction

The present work is motivated by the impact that insecurity produces for an urban area; evidently, there are different types of crimes, and each one must be studied to later design prevention policies. This work studies criminal agents' displacement effect, specialized in house robbery, with the possibility of making long journeys in a short time, described by Lévy Flights in a two-dimensional environment. We consider that this way of describing criminal diffusion is more realistic than models based on conventional diffusion. Understanding the mobility of certain social groups within an urban area is of great relevance for policymakers, especially displacements at specific geographical locations detrimental to security and forming specific patterns [1]. Several of today's models focus on the displacement of residential burglaries, this from the pioneering work by Short et al. [2, 3]. Both approximations show more significant criminal activity areas, known as hotspots. This work inspired numerous modifications, generalizations, and theoretical studies that described dynamical

➤ **Received:** 15.12.2021 ➤ **Revised:** 21.01.2022 ➤ **Accepted:** 22.01.2022 ➤ **Published:** 27.01.2022

properties, as in references [4, 5, 6, 7, 8, 9, 10, 11, 12, 13]. In these models, a local random walk with a certain degree of statistical bias defines diffusion dynamics among the criminal population. The core of model dynamics is that home thief's agents have a higher stochastical preference for specific targets known as the highest attractive zones. Several studies have been used to assess the stability of certain kinds of solutions to crime phenomena, as presented in references [12, 13, 14, 15]. This dynamic belongs to the so-called reaction-diffusion models, which are known to comprise a broad set of spatial distribution patterns [16]. Biased Brownian motion displacement is the kernel of the agent version when the agents are sensitive to environmental gradients. In the continuum limit, this phenomenon is modeled by of cross-diffusion equation. It is represented by Keller-Segel operator [17, 18]. One of the cross-diffusion attributes is that the increments represent a local displacement, where the criminal agent moves from site i to site j, and j is in the neighborhood of i. A more general model allows agents to travel to sites outside the neighborhood. These models are known as non-local diffusion and belong to the so-called anomalous diffusion models.

A non-local diffusion model would assume that criminals can make long jumps in a short time, thus moving towards more attractive areas. For example, motorized mobility is an influencing factor. The cause that house burglars would incur greater risk when leaving a familiar area may be due to real-time information received by other thieves. Sharing/receiving this information dynamically with other criminals they compete with may seem unlikely. However, Calvo et al. [19] provide an analysis of conditions under which different criminal agents are likely to collaborate. According to this, it is established that, once a home robbery agent has moved away to a specific area, he again uses random walking as a strategy to locate a target. Chaturapruek et al. [6] propose that so-called Lévy flights can describe that above dynamic, where the probability distribution of jumps length of robbery agents follows an inverse power law distribution. Thus, criminal agents can move from site i to j, where j is no longer part of the i neighborhood. Considering continuous limit, the fractional Laplacian operator appears analogously to the fractional Gierer Meinhardt model [20]. A particular property of fractional operator hotspots solutions is that they decay algebraically. Chaohao et al. [11] show that if the jump length is truncated, then a version of the conventional Laplacian diffusion model is obtained. It is considered that criminal agents do not leave a specific area, and the unique modification occurs in the diffusion coefficient. That study is carried out in one dimension for discrete and continuous cases; it also incorporates police effects on the criminal's attractiveness perception. S. Crúz-García et al. [21] propose an alternative method to Lévy flights, applying stochastic interference to the Jones et al. model [4], which contemplates large jumps from a small set of criminal agents at each time step. S. Crúz also found that if police presence is increased numerically in central hotspots, they will fragment into smaller areas. Other studies are based on discrete agent algorithms that incorporate Lévy flights in two dimensions and analyze patterns formation, depending on the model's parameters [22].

The police dissuasive influence is a multifaceted problem, and there are various proposals to be addressed, depending on the environmental conditions and the police agency's resources [23]. To illustrate this, the work of Jones [4] shows how police presence affects attractiveness when this is incorporated into the law enforcement scheme. Jones analyzes different strategies, among which Cops on the dots and Peripheral interdiction stand out; results from these studies depend on the urban environment's characteristics. Camacho [9] also compares these two strategies with one based on region partitioning into smaller areas (beats), within which cops can move, although they are not able to cross borders. Law enforcement has also been incorporated into one-dimensional fractional diffusion [6], based on the cops on the dots strategy; however, the parameter of criminal density diffusion are modified. In his work, Chaohao [11] also incorporates two forms of police agent's motion, one governed by biased Brownian diffusion and the second by Lévy flights. The main difference is that police shifts based on Lévy flights reach the steady-state solution in a shorter time.

The present work shows a two-dimensional extension of the Chaturapruek continuous model, incorporating law enforcement with Cops on dots strategy. These models have been published at the agent level (discrete) for the two-dimensional case, using Lévy flights, for example Brantingham et. al. [1], but this work proposes a deduction for the continuous two-dimensional case based on the one already made by Chaturapruek for one dimension. An interesting aspect is that it appears in our deduction, it is a new function that is the equivalent of Riemman's ζ for two dimensions, and that modifies the criminal diffusion coefficient. The main aim is to show numerically that hotspot solutions in attractiveness bi-dimensional fields are preserved by varying derivative order (in not truncated Lévy flights) using a spectral approximation to bi-dimensional fractional derivative operator. However, they may change shape or intensity. We also present criminal population spatial distribution patterns that reveal a more complex dynamic than the attractiveness field and exhibit strong dependence on the fractional order. The Cops on the dots strategy assumes that police officers have restricted movements, this differentiates the modeling behavior between house burglars with law enforcement. The investigatory police, who work within broader limits when applying their authority, represent a group that Lévy's flights might better model. However, in the present work, we do not consider this approach.

This paper is divided as follows; in Section 2, we introduce a model deduction for a two-dimensional problem. Subsection 2 presents the numerical method for model integration. Section 3 presents a qualitative analysis for stationary solutions, using a simplified attractiveness version in one dimension. A numerical sensitivity analysis of the model concerning the derivative order is performed in Section 4. In Section 5, we deduce the component that models law enforcement and present numerical results by changing fractional order, holding the Cops on dots strategy. In the final of this manuscript, a nomenclature section is presented.

2 Continuum fractional model formulation

The two-dimensional model is deduced regarding an analogous formulation of a one-dimension problem by Chaturapruek [6]. The scenario occurs in a lattice Ω with size $N \times N$, and the lattice spacing is $l = 1/N$. To simplify, we initiate the model derivation without including law enforcement. The position of each site d in Ω is represented by $d = (d_1, d_2) \in \mathbb{R}^2$. At site d and time t, there is an attractiveness $A_d(t)$, which is made of two components, $A_d(t) = A_d^0 + B_d(t)$, where A_d^0 is the intrinsic attractiveness and $B_d(t)$ is time-dependent attractiveness. The evolution of $A_d(t)$ depends on whatever occurs around it, i.e., a criminal agent can change attractiveness in a time interval δt by deciding whether or not to attack a d site, and he does so with the probability

$$p_d(t) = \frac{\epsilon A_d(t)}{1 + \epsilon A_d(t)}, \tag{1}$$

where $\epsilon > 0$ represents the effectiveness of the attractiveness at site d. Therefore, an increase in B_d in the time interval δt depends on $E_d(t)$, which indicates the number of criminal attacks on the same site during the same time interval

$$B_d(t + \delta t) = B_d(t) + \theta E_d(t),$$

here θ is the enhancement in attractiveness for a single criminal agent. Without considering that a criminal attack can exert influence in neighborhood (broken window effect [24]), the expression for $B_d(t)$ is

$$B_d(t + \delta t) = B_d(t)(1 - \omega\delta t) + \theta E_d(t),$$

where ω represents attractiveness decay rate. Permitting the inclusion of the diffusive term for attractiveness, we have

$$B_d(t + \delta t) = \left[(1 - \eta^*)B_d(t) + \frac{\eta^*}{d'}\sum_{d'} B_{d'}(t)\right](1 - \omega\delta t) + \theta n_d(t)p_d(t), \tag{2}$$

here $\eta^* > 0$ represents of attractiveness influence in position d to its immediate neighbors d', for this work, a regular Cartesian lattice is used, with $d' = 4$. Therefore, replacing in Eq. (2) the number of criminal attacks on site d in the time interval δt with the number of criminals $n_d(t)$, also replacing the probability that they will attack $p_d(t)$ and take the limit $l, \delta t \to 0$, keeping fixed the radius $l^2/\delta t$, and a new parameter $\epsilon^* = \theta\delta t$, which represents the influence of the criminal presence in each position d, in a time interval $(t, t + \delta t)$ (the detailed derivation can be seen in the work of Short et al. [2]), we have

$$\frac{\partial B(\mathbf{x}, t)}{\partial t} = \frac{\eta^* l^2}{4\delta t}\Delta B(\mathbf{x}, t) - \omega B(\mathbf{x}, t) + \epsilon^* \frac{l^2}{\delta t}\rho(\mathbf{x}, t)A(\mathbf{x}, t), \tag{3}$$

where $\rho(\mathbf{x}, t) = \lim_{l\to 0} n_d(t)/l^2$ is the criminal density, and the position $\mathbf{x} \in [0, 1] \times [0, 1]$ is defined as

$$\mathbf{x} = (x_1, x_2) = \lim_{N\to\infty, l\to 0} (d_1 l, d_2 l),\ d_1, d_2 \in [1, N].$$

For modeling criminal displacement agents in 2-D, we have the probability that a criminal will arrive at site $d = (d_1, d_2)$ from $i = (i_1, i_2)$, analogously to that defined by Chaohao et al. [11] for 1-D

$$q_{i\to d}(t) = \frac{w_{i\to d}}{\sum_{j\in\mathbb{Z}^2, j\neq i} w_{i\to j}}, \tag{4}$$

the relative weight $w_{i\to d}$ is defined as

$$w_{i\to d}(t) = \begin{cases} \frac{A_i(t)}{l^\mu ||i-d||^\mu}, & 1 \leq ||i - d|| < \infty \\ 0, & \text{other case} \end{cases}, \tag{5}$$

with $||\cdot||$ the Euclidean norm. Lévy flight is an anomalous diffusion, where the density function of jump length probability possesses an algebraic decay [20], so μ is the exponent of the underlying power law. Thus, can be expressed the following

$$\sum_{j\in\mathbb{Z}^2, j\neq i} w_{i\to j} = \sum_{j\in\mathbb{Z}^2, j\neq i} \frac{A_j(t)}{l^\mu ||i - j||^\mu} = \sum_{j\in\mathbb{Z}^2, j\neq i} \frac{A_j(t) - A_i(t)}{l^\mu ||i - j||^\mu} + \sum_{j\in\mathbb{Z}^2, j\neq i} \frac{A_i(t)}{l^\mu ||i - j||^\mu}. \tag{6}$$

On the other hand, bearing in mind the Riemann sum definition, on the continuum limit $l << 1$ for D dimensions, the operator $\mathcal{L}$ can be expressed as

$$\mathcal{L}f(\mathbf{x}) = \frac{1}{l^D}\int_{\mathbf{y}\in\mathbb{R}^D} \frac{f(\mathbf{y}) - f(\mathbf{x})}{||\mathbf{y} - \mathbf{x}||^\mu} d\mathbf{y} \approx \sum_{d\in\mathbb{Z}^D, d\neq i} \frac{f(\mathbf{y}) - f(\mathbf{x})}{l^\mu ||\mathbf{y} - \mathbf{x}||^\mu}. \tag{7}$$

Eq. (7) can be compared with respect to the fractional operator definition in D dimensions [20]

$$-(-\Delta)^s f(\mathbf{x}) = C_{D,2s}\int_{\mathbb{R}^D} \frac{f(\mathbf{y}) - f(\mathbf{x})}{||\mathbf{y} - \mathbf{x}||^{D+2s}} d\mathbf{y},\ C_{D,2s} = 2^{2s}\frac{\Gamma((D + 2s)/2)}{\pi^{D/2}|\Gamma(-s)|},\ 0 < s, \tag{8}$$

where $f(\mathbf{x}) : \mathbb{R}^D \to \mathbb{R}$. To simplify notation, it is defined $-(-\Delta)^s = \Delta^s$ [6], therefore, is possible to relate $\mathcal{L}$ with Δ^s as follows

$$\mathcal{L}f(\mathbf{x}) = l^{-D} C_{D,2s}\Delta^s f(\mathbf{x}),\quad \text{and}\quad \mu = D + 2s. \tag{9}$$

For bi-dimensional case ($D = 2$) implies $\mu \in (2, \infty)$ (4 coincide with the usual Laplacian operator). For cases where the order of the derivative $s \in \mathcal{Z}$, the operator Δ^s is a local property (conventional differentiability) and loses this local property when s is a non-integer [25]. A notable difference between cases 1 and 2-dimensions is explained in the following table:
Prefactors 2 and 4 in Table 1 are a consequence of the characteristic symmetries of the corresponding dimension. Non-integer values in the norm have their origin in diagonals that connect the point i with j.

Type of neighbors (i,j)	$D=1$ $\lvert i-j\rvert =$	$D=2$ $\lvert\lvert i-j\rvert\rvert =$
first	1	$1, \sqrt{2}$
second	2	$2, \sqrt{5}, 2\sqrt{2}$
third	3	$3, \sqrt{10}, \sqrt{13}, 3\sqrt{2}$
r-th	r	$r, \sqrt{r^2+1^2}, \sqrt{r^2+2^2}, \ldots, r\sqrt{2}$
$\sum_{j\in\mathbb{Z}^D, j\neq i} \frac{1}{\lvert\lvert i-j\rvert\rvert^{\mu}} =$	$2\sum_{r=1}^{\infty}\frac{1}{r^{\mu}}$	$4\sum_{r=1}^{\infty}\frac{1}{[\sum_{\alpha=0}^{r}\sqrt{(r^2+\alpha^2)}]^{\mu}}$

Table 1. The development in a series of accessible distances between the position i with j is shown.

Proposition 1 *For $\mu \geq 2$ and $r \geq 1$ the following inequality is satisfied:*

$$\frac{1}{r^{\mu}} \geq \frac{1}{[\sum_{\alpha=0}^{r}\sqrt{r^2+\alpha^2}]^{\mu}}.$$

Proof 1 *In essence, it is necessary to show $r^{\mu} \leq [\sum_{\alpha=0}^{r}\sqrt{r^2+\alpha^2}]^{\mu}$, in particular for $\mu \geq 2$, expanding the series and factorizing terms, we need to prove*

$$r \leq \sum_{\alpha=0}^{r}\sqrt{r^2+\alpha^2} = r\sqrt{r\left[\frac{r(r+1)(2r+1)}{6}\right]},$$

but, $r(r+1)(2r+2)/6 = 1+2^2+3^2\ldots+r^2 \geq 1$ and $r \geq 1$, then

$$\sqrt{r\left[\frac{r(r+1)(2r+1)}{6}\right]} \geq 1,$$

therefore is satisfied $r^{\mu} \leq [\sum_{\alpha=0}^{r}\sqrt{r^2+\alpha^2}]^{\mu}$ and the Proposition 1.

Using Proposition 1, it is possible to show

$$\sum_{r=1}^{\infty}\frac{1}{r^{\mu}} \geq \sum_{r=1}^{\infty}\frac{1}{[\sum_{\alpha=0}^{r}\sqrt{(r^2+\alpha^2)}]^{\mu}},$$

thus, we can define

$$z(\mu) = 2\sum_{r=1}^{\infty}\frac{1}{r^{\mu}} = 2\zeta(\mu), \text{ and } Z(\mu) = 4\sum_{r=1}^{\infty}\frac{1}{[\sum_{\alpha=0}^{r}\sqrt{(r^2+\alpha^2)}]^{\mu}}, \tag{10}$$

where $\zeta(\mu)$ is the Riemann function and $Z(\mu)$ is a new function adapted to the 2-dimensional case, and is satisfied $\frac{1}{2}Z(\mu) \leq z(\mu)$ for $\mu > 2$, this implies that $Z(\mu)$ is well defined, therefore,

$$\sum_{j\in\mathcal{Z}^2, j\neq i} w_{i\to j} = \mathcal{L}A_i(t) + l^{-\mu}Z(\mu)A_i(t),$$

so, the probability $q_{i\to d}$ could be expressed in terms of $\mathcal{L}$ and $Z = Z(\mu)$

$$q_{i\to d} = \frac{A_d(t)}{\lvert\lvert i-d\rvert\rvert^{\mu}}\left(\frac{1}{ZA_i(t)} - \frac{\mathcal{L}A_i(t)l^{\mu}}{Z^2A_i^2(t)}\right). \tag{11}$$

The result of Eq. (11) is used below in Eq. (13). The derivation of the 2-D model, in essence, is the one developed by Chaturapruek [6] for 1-D, which is clearly explained. However, an outline of the deduction is shown below.

The criminal dynamics agents can be highly complex, so limiting the model's scope is required. For this, the following assumptions are proposed:

- At position i for each time interval δt, two things are possible: (a) Each criminal commits a crime with probability $A_i\delta t$, (b) He moves to another location direction that is biased by the attractiveness distribution field.
- New criminals are being created everywhere, with a Γ spawn rate. This property allows a regular population of criminals to move continuously to more attractive places.
- House burglars can only move from a site i to a site d by means of $q_{i\to d}$ or otherwise be generated at d, at a rate Γ.
- A portion λ, proportional to house burglars $n_i(t)$, can cease to operate, leaving without committing a crime.

Expression (12) models the criminal dynamics, established on previous assumptions, such that

$$n_d(t+\delta t) = \sum_{i\in\mathbb{Z}^2, i\neq d} n_i(t)(1-A_i(t)\delta t)\cdot q_{i\to d} - \lambda n_d(t)\delta t + \Gamma\delta t, \tag{12}$$

subtracting $n_d(t)$ from both sides and dividing everything by δt, we have

$$\frac{n_d(t+\delta t)-n_d(t)}{\delta t} = \frac{1}{\delta t}\left[\sum_{i\in\mathbb{Z}^2, i\neq d} n_i(t)(1-A_i(t)\delta t)\cdot q_{i\to d} - n_d(t)\right] - \lambda n_d(t) + \Gamma, \tag{13}$$

considering only the term into the brackets of the previous equation, and replacing $q_{i\to d}$ from Eq. (11)

$$\begin{aligned}\sum_{i\in\mathbb{Z}^2, i\neq d} n_i(t)(1-A_i(t)\delta t)\left[\frac{A_d(t)}{||i-d||^\mu}\left(\frac{1}{ZA_i(t)} - \frac{\mathcal{L}A_i(t)l^\mu}{Z^2A_i(t)^2}\right)\right] - n_d(t)\\ =A_d(t)\left[\left(\sum_{i\in\mathbb{Z}^2, i\neq d}\frac{n_i(t)}{A_i(t)}(1-A_i(t)\delta t)\frac{1}{||i-d||^\mu Z}\right) - \frac{n_d(t)}{A_d(t)}\right]\\ - \sum_{i\in\mathbb{Z}^2, i\neq d} n_i(t)(1-A_i(t)\delta t)\frac{A_d(t)}{||i-d||^\mu}\frac{\mathcal{L}A_i(t)l^\mu}{Z^2A_i^2(t)},\end{aligned} \tag{14}$$

based on the fact that $n_d(t) = \sum_{i\in\mathbb{Z}^2, i\neq d}\frac{n_i(t)}{||i-d||^\mu Z}$, truncating to order $\mathcal{O}(l^\mu, \delta t)$ and neglecting terms $\mathcal{O}(l^\mu\delta t, l^{2\mu})$ [6], we have

$$\approx A_d(t)\sum_{i\in\mathbb{Z}^2, i\neq d}\left[\frac{\frac{n_i(t)}{A_i(t)} - \frac{n_d(t)}{A_d(t)}}{||i-d||^\mu Z} - \frac{n_i(t)}{||i-d||^\mu}\left(\frac{\mathcal{L}A_i(t)l^\mu}{A_i^2(t)Z^2}\right) - \delta t\frac{n_i(t)}{||i-d||^\mu Z}\right],$$

using the right side of the definition of operator $\mathcal{L}$ in equation (7)

$$\approx A_d(t)\left[\frac{l^\mu}{Z}\mathcal{L}\left(\frac{n_d(t)}{A_d(t)}\right) - n_d(t)\frac{\mathcal{L}A_d(t)l^\mu}{A_d^2(t)Z} - \delta t n_d(t)\right], \tag{15}$$

substituting the last result (15) in Eq. (13), applying the limit $l, \delta t\to 0$, and using Eq. (9) that relates the operator $\mathcal{L}$, with Δ^s, we have

$$\frac{n_d(t+\delta t)-n_d(t)}{\delta t} = \frac{l^\mu}{\delta t Z C_{2,2s}}\left[A(\mathbf{x},t)\Delta^s\left(\frac{n(\mathbf{x},t)}{A(\mathbf{x},t)}\right) - \frac{n(\mathbf{x},t)}{A(\mathbf{x},t)}\Delta^s(A(\mathbf{x},t))\right] - n(\mathbf{x},t)A(\mathbf{x},t) - \lambda n(\mathbf{x},t) + \Gamma, \tag{16}$$

in agree to equation (8) for the case $D = 2$

$$C_{2,2s} = \frac{2^{2s}\Gamma(s+1)}{\pi|\Gamma(-s)|},$$

dividing Eq. (16) by l^2, using the limit $\delta t, l\to 0$, and the definition $\rho(\mathbf{x},t) = \lim_{l\to 0} n_d(t)/l^2$, we obtain the Lévy Flight Model approximation for criminal density $\rho(\mathbf{x},t)$, as shown in Eq. (18). On the other hand, from equation (3), is obtained directly Eq. (17) (using $A(\mathbf{x},t) = B(\mathbf{x},t) + A^0(\mathbf{x})$), as follows

$$\frac{\partial A(\mathbf{x},t)}{\partial t} = \eta\Delta(A(\mathbf{x},t) - A^0(\mathbf{x})) - \omega(A(\mathbf{x},t) - A^0(\mathbf{x})) + \epsilon\rho(\mathbf{x},t)A(\mathbf{x},t), \tag{17}$$

$$\frac{\partial\rho(\mathbf{x},t)}{\partial t} = M\left[A(\mathbf{x},t)\Delta^s\left(\frac{\rho(\mathbf{x},t)}{A(\mathbf{x},t)}\right) - \frac{\rho(\mathbf{x},t)}{A(\mathbf{x},t)}\Delta^s\Big(A(\mathbf{x},t)\Big)\right] - A(\mathbf{x},t)\rho(\mathbf{x},t) - \lambda\rho(\mathbf{x},t) + \gamma. \tag{18}$$

With the following definitions:

$$\eta = \frac{\eta^* l^2}{4\delta t},\quad \epsilon = \epsilon^* l^2,\quad M = \frac{l^{\mu-2}}{\delta t Z C_{2,2s}},\quad \gamma = \frac{\Gamma}{l^2}. \tag{19}$$

Numerical integration

A straightforward way to approximate the two-dimensional fractional Laplacian operator is by Fast Fourier Transform (FFT) properties [26, 27]. The underlying factor that allows us to take advantage of the Fourier transform is that by projecting the fractional Laplacian operator to the Fourier modes space, differential operations are transformed into algebraic operations, which is relatively simple to compute. Subsequently, the inverse transform is applied, thus completing the cycle to approximate the fractional operator. Therefore, the spectral approximation [28] to Δ^s is expressed as follows:

$$\Delta^s A = \text{real}\Big\{\mathcal{F}_{2D}^{-1}\Big\{-(kx^{2s} + ky^{2s})\mathcal{F}_{2D}\{A\}\Big\}\Big\},$$

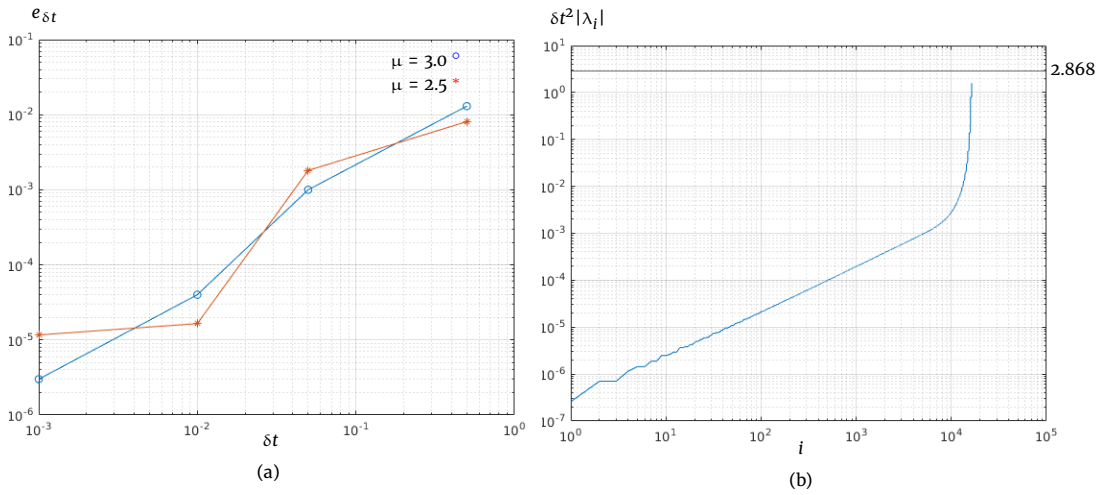

Figure 1. (a) Relative error approximation e_{dt} as function of $\delta t = \{0.5, 0.05, 0.01, 0.001\}$ after integrating a time $t = 200$ using parameters defined in Fig. 2. (b) Values $\delta t^2|\lambda_i|$, $i = 1 \dots N^2$ of discrete space operator of attractiveness. It can be seen that the stability condition $\delta t^2|\lambda_{\max}| < 2.868$ is satisfied, with $\lambda_{\max} = \max\{\lambda_i\}$.

$\mathcal{F}_{2D}$ represents the Fourier transform in two dimensions, and $kx, ky \in \mathcal{Z}$, are the wavenumbers in each orthogonal direction, respectively. Time derivatives ($\partial A/\partial t$, $\partial \rho/\partial t$) are solved via a succession between an explicit and an implicit method, as explained below. Let

$$f(A_t, \rho_t) = \begin{pmatrix} \frac{\partial A(\mathbf{x},t)}{\partial t} \\ \frac{\partial \rho(\mathbf{x},t)}{\partial t} \end{pmatrix}.$$

Step 1: A predictive step is made according to the explicit Adams-Bashforth method [29]

$$(\tilde{A}_{t+\delta t}, \tilde{\rho}_{t+\delta t}) = (A_t, \rho_t) + \frac{dt}{24}\Big[55f(A_t, \rho_t)) - 59f(A_{t-\delta t}, \rho_{t-\delta t}) + 37f(A_{t-2\delta t}, \rho_{t-2\delta t}) - 9f(A_{t-3\delta t}, \rho_{t-3\delta t})\Big]. \tag{20}$$

Step 2: A correction stage is now implemented, following the implicit Adams-Moulton method

$$(A_{t+\delta t}, \rho_{t+\delta t}) = (A_t, \rho_t) + \frac{dt}{24}[9f(\tilde{A}_{t+\delta t}, \tilde{\rho}_{t+\delta t}) + 19f(A_t, \rho_t) - 5f(A_{t-\delta t}, \rho_{t-\delta t}) + f(A_{t-2\delta t}, \rho_{t-2\delta t})]. \tag{21}$$

A successive combination at each time step into explicit (20), and implicit (21) integration procedure, conforms a four-step Predictor-Corrector method (PC4) [30]. Three additional steps are generated by applying a fourth-order Runge-Kutta method (RK4) to initiate the integration process. The reason for using PC4 is because of its lower computational cost compared to RK4 [31]. However, exists alternatives, for example, the proposed by C. Tadjeran and M. Meerschaert [32], explicitly designed for fractional operators. To evaluate the convergence of the numerical solution, the definition of relative error $e_{\delta t} = \max\{[A_{t+\delta t} - A_t]/A_t\}$ is used. The calculations of $e_{\delta t}$ with $\delta t = \{0.5, 0.05, 0.01, 0.001\}$ are presented in graph (a) of Fig. 1 for $\mu = \{2.5, 3\}$, the rest of parameters are defined in Fig. 2. One method to determine spectral stability in time depending on partial differential equations is to calculate the eigenvalues λ_i, $i = 1 \dots N^2$ of the spatial discretization of the operator $\Delta^* = \eta\Delta - \omega + \epsilon\rho(t, \mathbf{x})$ scaled by δt^2 (two dimensions) [28]. Stability condition for PC4 is $\delta t^2|\lambda_{\max}| < 720/251 \approx 2.868$ [33]. In graph (b) of Fig. 1, the eigenvalues of the discretization of the spatial operator of attractiveness A scaled by δt^2 are shown.

In Fig. 2 initial condition and numerical integration is shown. The parameter values are fixed in $N = 256$, $dt = 1 \times 10^{-3}$, integration $t = 200$, and $\eta^* = 3.94$, $\lambda = 0.05$, $\omega = 0.05$, $\Gamma = 0.019$, $\epsilon = 0.10$. (a) Initial condition is an attractiveness random map, the initial burglaries density $\rho(\mathbf{x})_0$, is a homogeneous distribution fixed at 0.2 and boundary conditions are periodic. In (b) $\mu = 4.40$ corresponds with $s = 1.20$. Maximum attractiveness intensity showed an increase compared to the initial condition, achieving a maximum of ≈ 0.8. (c) $\mu = 2.50$ corresponding with derivative order $s = 0.25$, in this case, dominate Lévy flights over Gaussian diffusion, it can be seen how attractiveness is concentrated in two principal regions (central hotspots) achieving a maximum of ≈ 1.6. The non-local effect of fractional operator explains that this plays a relevant role in how the crime field influences attractiveness distribution.

The preceding numerical examples show relatively distant cases compared to the fractional order. The most relevant aspect is the formation of intense few hotspots (central hotspots) in issues where Lévy flights dominate. For example, this result has particular interest for modeling metropolitan areas where attractiveness does not manifest homogeneous space of small hotspots distribution. Still, instead, a few hotspots rise, as is usually the case with city centers, as shown in [21]. In the case of $s \approx 1$ were recovered Laplacian diffusion results.

3 Approximate analysis for stationary solutions in one dimension

For some nonlinear phenomena under specific continuity conditions, can be done a study through a power series approximation. This idea is based on the assumption that solutions are analytical functions concerning some of their parameters. The series length is infinite, but an

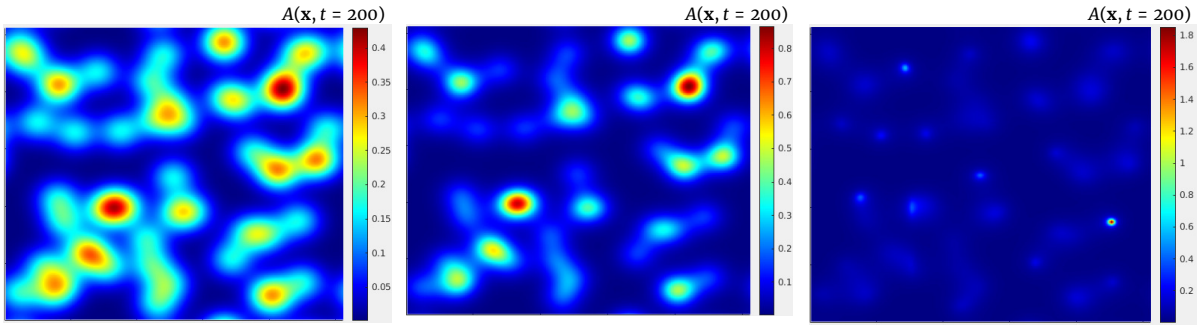

(a) Initial condition (b) $s = 1.20$ (a) $s = 0.25$

Figure 2. (a) Initial condition and (b-c) final state after integrating equations (17), (18) for a time $t = 200$. Boundary conditions are periodic for both examples. The parameters are fixed in $N = 256$, $\eta^* = 3.94$, $\lambda = 0.05$, $\omega = 0.05$, $\Gamma = 0.019$ and $\epsilon = 0.10$. Case (b) $\mu = 4.40$ corresponding with $s = 1.20$, the number of hotspots has been reduced compared to the initial condition, but the magnitude of the intensity has increased. (c) $\mu = 2.50$ equivalent to $s = 0.25$, in this instance Lévy flights (anomalous diffusion), dominate over Laplacian diffusion, the formation of hotspots with a mayor intensity is observed (respect to (b)). These can be explained as the non-spatial locality effect of the fractional operator, which allows the crime density field ρ to have a more significant influence on the appearance of a few high-intensity hotspots in the attractiveness A.

approximate model is obtained by truncating to a specific power order. The precision radius is usually a function of the power order trimmed in the series. Expanding series analysis is applied to estimate the local phenomenology of the original system through an approximate model. There are studies using series expansion on stationary solutions for the Short model [2, 7, 10]. Other studies have also been made to assess their stability [3, 8, 15, 34] and bifurcation analysis [35, 36]. Our study proposes a series expansion analysis, considering the density home burglaries field as an analytical function of attractiveness. A comparable analysis is undertaken in reference [6], although the ansatz for expansion is different from the one suggested here, as shown below. Using equation (17) in the steady-state i.e. $\partial A/\partial t = 0$, also, consider special case $A^0 = \tilde{\alpha}$ (constant in all Ω), we propose

$$\eta \Delta A - \omega A + \epsilon A \rho(A) + \omega \tilde{\alpha} = 0, \text{ and } \rho(A) = \sum_{i=0}^{\infty} \tilde{\beta}_i(s) A^i. \tag{22}$$

Replacing $\rho(A)$, dividing by η, and ordering by powers of A, we have

$$\Delta A - \frac{(\omega - \epsilon \tilde{\beta}_0)}{\eta} A + \frac{\epsilon \tilde{\beta}_1}{\eta} A^2 + \frac{\epsilon \tilde{\beta}_2}{\eta} A^3 + \ldots = -\frac{\omega \tilde{\alpha}}{\eta},$$

renaming the coefficients, as $\beta_1 = \frac{(\omega - \epsilon \tilde{\beta}_0)}{\eta}$, for $i \geq 2$ $\beta_i = \frac{\epsilon \tilde{\beta}_{i-1}}{\eta}$ and $\alpha = \frac{\omega \tilde{\alpha}}{\eta}$, therefore,

$$\Delta A - \beta_1(s) A + \beta_2(s) A^2 + \beta_3(s) A^3 + \ldots = -\alpha.$$

For qualitative analysis, we will work on one dimension ($\Delta A = A_{xx}$), and the last expression is truncated to the third power in A. Which provides us with a non-homogeneous and non-linear ordinary differential equation

$$A_{xx} - \beta_1(s) A + \beta_2(s) A^2 + \beta_3(s) A^3 = -\alpha. \tag{23}$$

For the analysis, we propose changing the second-order differential equation (23) for two first-order equations, as follows:

$$\begin{aligned} A_x &= M, \\ M_x &= \beta_1(s) A - \beta_2(s) A^2 - \beta_3 A^3 - \alpha. \end{aligned} \tag{24}$$

One further approximation is required to introduce the functional relationship between $\beta_{i=1,2,3}$, with respect to the derivative order s. In a small disturbances scheme (concerning intrinsic attractiveness), a linear relationship is suggested for the three functions, such that $\beta_i(s) = a_i s$. Fig. 3 presents the numerical solution for this approximation level. In Fig. 3 (a) the configuration space $M(\mathbf{x})$ vs $A(\mathbf{x})$ is plotted for several values of derivative order $s \in [0.2, 1.4]$. In Fig. 3 (b) Solution of eqs. (24) is shown with coefficients $a_1 = 100$, $a_2 = 8$, $a_3 = 8$, which resemble spike solutions. (c) For the complete model (eqs. (17)-(18) in 1-Dimension) is shown $M(\mathbf{x})$ vs $A(\mathbf{x})$, with parameters $\eta = 3.874$, $\omega = 0.05$, $\lambda = 0.09$, $\Gamma = 5 \times 10^{-6}$, $\epsilon = 0.04$, $s \in [0.2, 1.4]$, the initial conditions are $A(\mathbf{x}, 0) = (1 - \cos(2\pi \mathbf{x}))$, $\rho(\mathbf{x}, 0) = 0.1$ and the subjacent attractiveness $\alpha = A^0(\mathbf{x}) = 0.1$. (d) Are shown solutions of $A(\mathbf{x}, t = 200)$, for different derivative order values $s \in [0.2, 1.4]$. In sub Figs. (a)-(d), curves with the maximum amplitude correspond with lower values of s, and the amplitude decrease when s is incremented. Visually, it can be seen that the behavior of the real and approximate solutions are qualitatively different. By tuning the parameters in the approximate model, the amplitude and width of the curves can be adjusted, however, to modify the shape of the curve a different model is required. With this observation, we can say that an approximation by a few terms is not enough to capture the dynamic of the attractiveness represented by Eq. (17). Also, the linear relationship between the coefficients $\beta_{i=1,2,3}$ and the order of the derivative s, seems not to be adequate to approximate the behavior of the system.

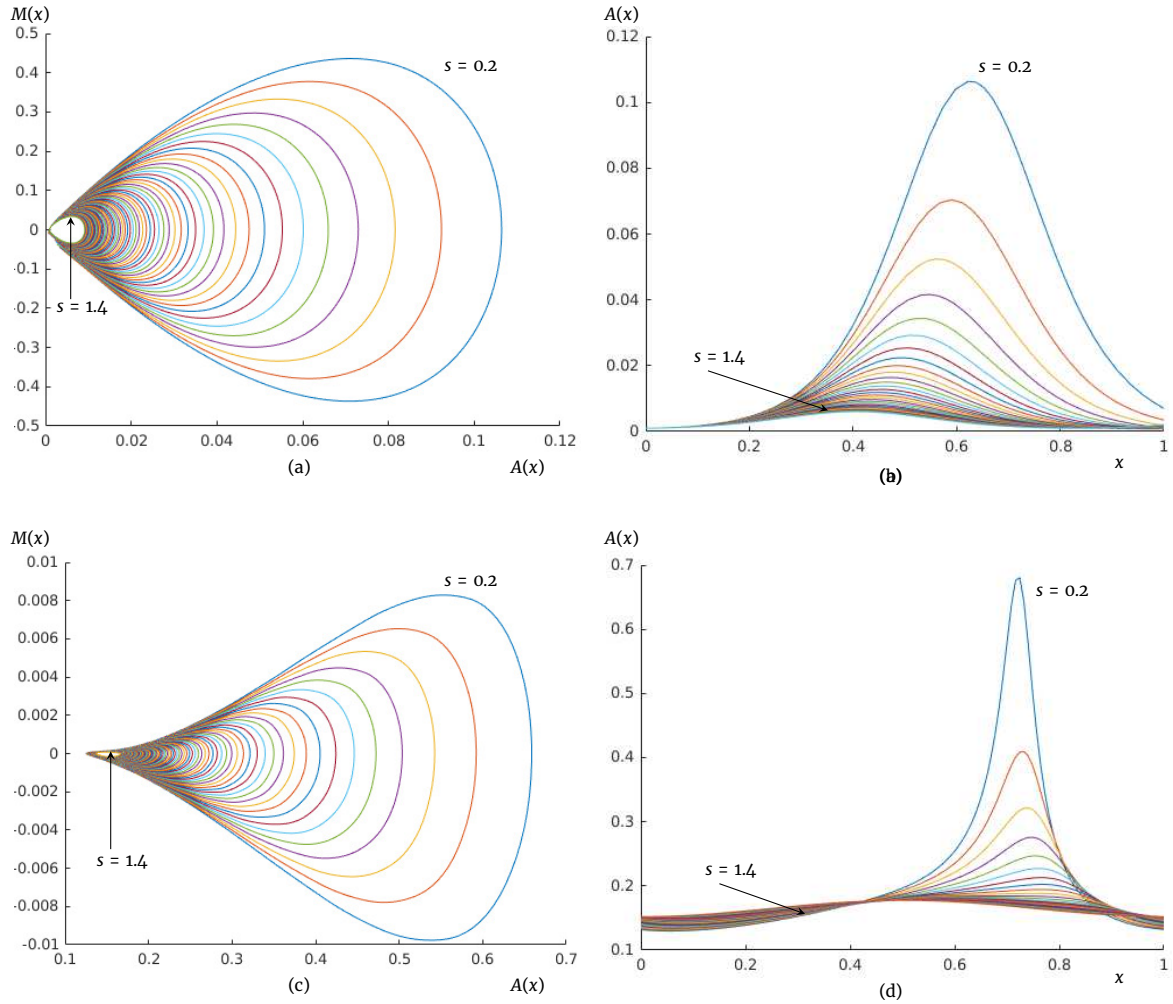

Figure 3. Graphical comparison between complete (eqs. (17) and (18) in 1-dimension) and approximated model (Eq. (24)). (a) Evolution of different derivative order values $s \in [0.2, 1.4]$ for $M(x) = \partial A(x)/\partial x$ vs $A(\mathbf{x})$. (b) Spatial distribution of $A(\mathbf{x})$ for $s \in [0.2, 1.4]$. (c) Solution of the complete model (eqs. (17), (18) in 1-dimension) for derivative order $s \in [0.2, 1.4]$. (d) Spatial distribution of the solution $A(\mathbf{x}, t = 200)$ for $s \in [0.2, 1.4]$. The parameters of the approximation (Eq. (24)) are $\beta_i(s) = a_i s$ with $a_1 = 100$, $a_2 = 8$, $a_3 = 8$. Parameters of the eqs. (17) and (18) are $\eta = 3.874$, $\omega = 0.05$, $\lambda = 0.09$, $\Gamma = 5 \times 10^{-6}$, $\epsilon = 0.04$ and $\alpha = A^0(\mathbf{x}) = 0.1$. It is appreciated that an approximation of a few terms and linear relations of the $\beta_{i=1,2,3}$ coefficients and s does not consistently capture the dynamics of the complete model. However, the relation between curve amplitude and fractional derivative is represented in a qualitative way.

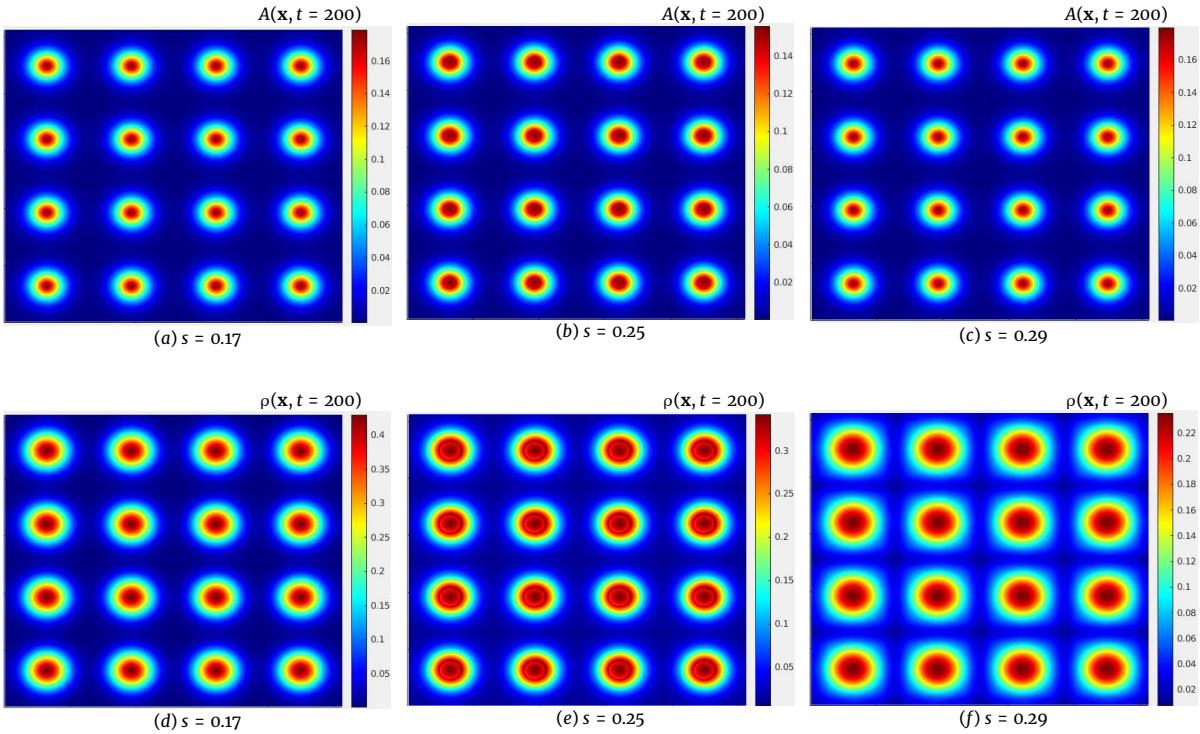

Figure 4. Numerical attractiveness solution $A(\mathbf{x}, t)$, after integrating for $t = 200$. (a), (b) and (c) represent the attractiveness field for $s = \{0.17, 0.25, 0.29\}$ respectively. Figures (d), (e) and (f) correspond to the criminal density distribution field for (a), (b) and (c) respectively. The three scenarios show in the attractiveness field a hotspot's existence, coupled spacially with hotspots in the criminal density field. For case (a)-(d), the attractiveness hotspots have a localized and intense dot at the center, and the criminal density field exhibits similar behavior. In (b)-(d) appears an intense ring around the center of the hotspot. Those phenomena occur in attractiveness and criminal density fields. In figures (c) -(f), the attractiveness increases marginally concerning the previous cases. The hotspots in crime density are less intense than (a)-(c) and (b)-(e).

4 Numerical analysis of fractional order in 2-dimensions

Using the integration method explained in Subsection 2, several bi-dimensional scenarios were calculated, while varying s. The initial condition $A_0(\mathbf{x})$ for all cases is composed of an array with 4×4 Gaussian distributions on the domain $\Omega = [0, 1] \times [0, 1]$ and periodic boundary conditions. In Fig. 4, the final state is shown after integrating by $t = 200$ for $s = \{0.19, 0.25, 0.29\}$, with parameters $\eta = 3.947^*$, $\omega = 0.05$, $\lambda = 0.05$, $\Gamma = 0.0019$, $\epsilon = 0.10$. As observed in Figs (a)-(c) (attractiveness) and (d)-(f) (density criminal agents), exist different behavior regimes for values of $s < 0.45$, which is where the Lévy flights dominate over conventional diffusion. Although there are not quite significant changes in the attractiveness hotspots magnitude in (a)-(c), there are more noticeable changes in criminal agents density distribution (d)-(f). To explain this change is necessary to understand criminal density dynamics, as we hypothesized below. In the space of criminal density, Figs. (d)-(f) a descending difference in the magnitude of the hotspot can be observed, while s increases, simultaneously the hotspot base becomes wider. The hypothesis is that stochastic flights are longer and directed to the most attractive areas, with greater precision, while $s < 1$. When derivative order s increases, Lévy flights exist, but now they compete with Laplacian diffusion.

In agreement with numerical observations (Fig. 4), there are two-dimensional periodic solutions for different derivative order values s. However, there are considerable differences between them, analogous to the one-dimensional case reported by Chaturapruek et al. [6]. The magnitude and spatial distribution of the attractiveness field and the criminal density constitute most of these differences. The results interpretation is that for $s < 1$, the fractional operator Δ^s manifests its non-local nature. From graphs of Fig. 4, the maximum attractiveness intensity variation is observed by changing parameter s. The two-dimensional system solutions are determined numerically for $s \in [0.17, 1.20]$. To analyse results, we determine global properties $\max[A]/\max[A_0]$ (max for all $\mathbf{x}$ on Ω), as a function of s.

In Fig. 5 it is observed how the total attractiveness $\mathrm{I}[A_s]$, defined in equation (25) shifts with respect to the total attractiveness of the initial condition $\mathrm{I}[A_0]$. In graphs (a) and (b) of Fig. 5, both properties are shown, as well as the integration time $t = 200$. Graph (a) for $s < 0.5$ corresponds to a regime where Lévy flights dominate Laplacian diffusion. The Maximum attractiveness reaches high values compared to the rest of the graph. The region $0.5 < s$ shows $\max A_s / \max A_0$ has small variations, but it shows a local maximum at $s \approx 1$. In graphs (a)-(b), it is observed that in the case $s > 0.5$, the attractiveness magnitude remains low (respect to the case $s < 0.5$) and continues with this trend, for s explored in this experiment. The hypothesis to explain these two regimens is a behavior change between them from Lévy flights diffusion to one where the Laplacian diffusion has relevant effects or dominates. As a result of the analysis of graphs, it can be said that in an environment where criminal agents have high mobility, attractiveness increases significantly for usual Laplacian diffusion.

$$\mathrm{I}[A_s] = \int_\Omega A_s(\mathbf{x}, t = T_c)d\mathbf{x} \text{ and } \mathrm{I}[A_0] = \int_\Omega A_0(\mathbf{x})d\mathbf{x}. \tag{25}$$

In Fig. 5 the substantial increase in both global attractiveness properties, for values of $s < 0.45$ reveals a significant criminal population is leaving its neighborhood and is continually moving to the most attractive areas. This mechanism is reinforced by a cyclical process and

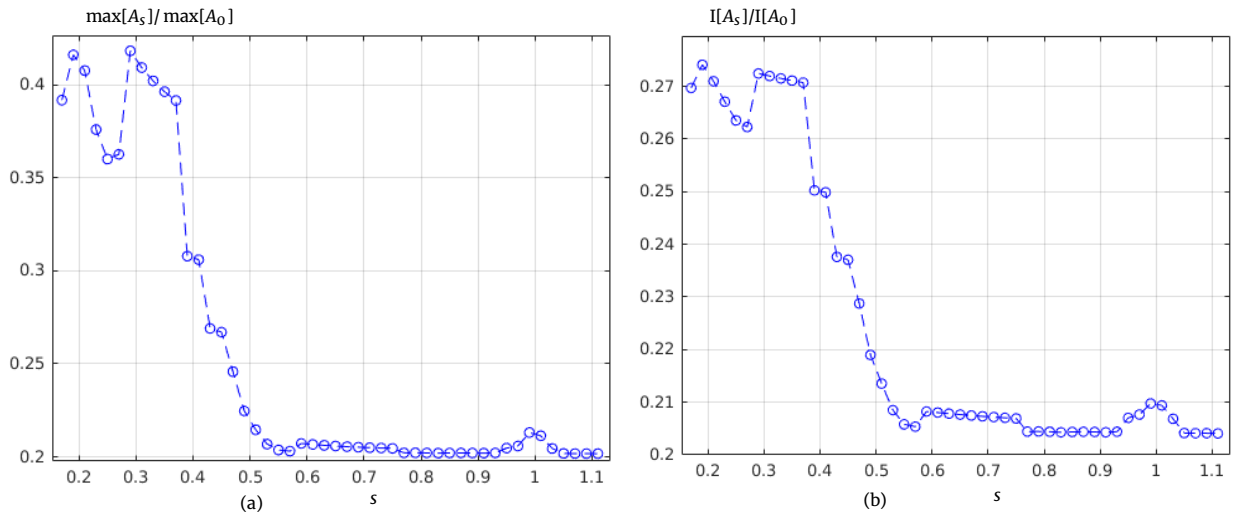

Figure 5. In both graphs the parameters are fixed at $T_c = 200$, $\eta = 3.947$, $\omega = 0.05$, $\lambda = 0.05$, $\Gamma = 0.0019$, $\epsilon = 0.10$ and $s \in [0.17, 1.20]$. (a) Evolution of $\max[A_s]/\max[A_0]$, which measures the maximum attractiveness values in Ω. Graph (b) shows $I[A_s]/I[A_0]$, which represents a total attractiveness measurement in Ω. As the previous graph, this shows two attractiveness regimes with a transition zone between them, for the same values of Ω, although, there is a significant decrease when $s = 1$, which corresponds to the usual Laplacian diffusion. In both graphs, there is evidently a region for values of $s < 0.4$ where essentially there is great attractiveness, both at the maximum intensity level, as in case (a), and global attractiveness, as in case (b). The explanation for this increase in attractiveness relates to greater mobility among the criminal population.

is only limited by local diffusion. In fact, for $s \lesssim 0.37$, the numerical solutions show a remarkable increase, as local criminal diffusion is not enough to delocalize the high attractiveness concentration, and the integration process is numerically unstable. Another exciting aspect is the apparition of a local maximum for $s \approx 1$ because evidence of a substantial change occurs within the usual Laplacian diffusion regime (for the case $s = 1$, the conventional definition of the Laplacian operator is used) in this regime, an intense local diffusion increase the attractiveness. In Fig. 5 (b) is shown the total attractiveness on Ω, it has a similar trend to that of the graph (a), that is, the global attractiveness also changes as a function of s.

5 Law enforcement of fractional bi-dimensional model

How police officers engage with the attractiveness field is fundamental to the model dynamics. As mentioned before, there are several law enforcement strategies for Laplacian diffusion, and each one produces different results [4, 9, 11], particularly in the work of N. Rodriguez [37], a complete study is made of different patterns on hotspot policing. The usual Laplacian diffusion models primarily represent these, and those fractional models represent only one dimension. Two main components maintain the incorporation of police officers: (a) Displacement dynamics over the environment, i.e., displacement rules. (b) The way criminals interact with the environment; what makes criminals perceive particular sites as less attractive. The strategy applied in this work is cops on the dots, considering this as a typical law enforcement example. Therefore, police agents' existence modifies criminal attractiveness perception in the following way

$$\tilde{A}_d(t) = e^{-\chi k_d(t)} A_d(t), \tag{26}$$

where $\chi > 0$ represents police influence on criminal perception. The probability that a criminal agent performs an attack on the site $d \in \Omega$ at time $t + \delta t$ is expressed as

$$\tilde{p}_d(t) = \frac{\epsilon \tilde{A}_d(t)}{1 + \epsilon \tilde{A}_d(t)}.$$

A similar deduction to that described by the equations (1) and (3), is made, for attractiveness in the police presence $A(\mathbf{x}, t)$, and residential burglaries $\rho(\mathbf{x}, t)$. In the continuous limit, we have

$$\frac{\partial A(\mathbf{x}, t)}{\partial t} = \eta \Delta A(\mathbf{x}, t) - \omega(A(\mathbf{x}, t) - A_0) + \epsilon \theta \tilde{A}(\mathbf{x}, t)\rho(\mathbf{x}, t). \tag{27}$$

In the case of $\rho(\mathbf{x}, t)$, the attractiveness change, expressed in equation (26), is exhibited in a variety of probability $q_{i,d}$ to go from a site i to d in a $(t, t + \delta t)$ period, as follows:

$$q_{i \to d} = \frac{w_{i \to d}}{\sum_{d \in \mathcal{Z}, d \neq i} w_{i \to d}},$$

where the weight $w_{i \to d}$ is defined as

$$w_{i \to d} = \frac{\tilde{A}_d(t)}{l^{\mu} ||i - d||^{\mu}},$$

and the sum of the weights is

$$\sum_{d\in\mathcal{Z}^2, d\neq i} w_{i\to d} = \sum_{d\in\mathcal{Z}^2, d\neq i} \frac{\tilde{A}_d(t)-\tilde{A}_i(t)}{l^\mu ||i-d||^\mu} + \sum_{d\in\mathcal{Z}^2, d\neq i} \frac{\tilde{A}_i(t)}{l^\mu ||i-d||^\mu}.$$

Using equation (9) for the operator $\mathcal{L}$, and with a similar deduction to that shown in section 2, then we have:

$$\frac{\partial \rho(\mathbf{x},t)}{\partial t} = D\left[\tilde{A}(\mathbf{x},t)\Delta^s\left(\frac{\rho(\mathbf{x},t)}{A(\mathbf{x},t)}\right) - \frac{\rho(\mathbf{x},t)}{\tilde{A}(\mathbf{x},t)}\Delta^s\left(\tilde{A}(\mathbf{x},t)\right)\right] - \tilde{A}(\mathbf{x},t)\rho(\mathbf{x},t) + \gamma. \tag{28}$$

Values for D and γ are specified in equation (19). A relevant aspect of the cops on the dots strategy is that those police officers are biased towards the most attractive areas. These phenomena generate a masking effect that reduces the attractiveness perception of criminals concerning specific places, thus forcing them to move to less attractive areas or disappear from the scene without ever committing a crime. The probability that a police officer will move from site i to site d is

$$q_{i\to d}(t) = \frac{A_d(t)}{\sum_{i\sim d} A_i(t)},$$

the expected number k of police agents at site d over time $t+\delta t$ is expressed as

$$k_d(t+\delta t) = \sum k_i(t) q_{i\to d}(t).$$

Chaohao [11] make a similar deduction for the continuous limit, which, if adapted to the two-dimensional case, can be expressed as:

$$\frac{\partial k}{\partial t} = \tilde{D}\nabla\cdot\left[\nabla k - \frac{2k}{A}\nabla A\right], \tag{29}$$

where $\tilde{D} = \omega D$. The equations (27)-(29) represent the fractional diffusion model with law enforcement, which will be used for the simulations below. The model parameters were set in $T_c = 200$, $\eta^* = 3.94$, $\lambda = 0.05$, $\omega = 0.05$, $\Gamma = 0.019$, $\epsilon = 0.15$, $s \in [0.17, 1.20]$ and the effect of the law enforcement $\chi = 0.0, 0.86, 3.86$. Similar to the section 4, the maximum and the attractiveness total sum over Ω, is determined integrating and divided by the maximum and the total sum, respectively, of the initial condition A_0.

A relevant aspect to the law enforcement incorporate, then integration of the system (Eqs. (27)-(29)) becomes unstable for $s < 0.5$, although it also depends on the value of χ. This phenomenon is notorious because the system shows a large ring formation around the hotspot center before blowing up.

In Fig. 6 (a) the $\max[A_s]/\max[A_0]$ for $\chi = 0.0, 0.86, 3.86$ indicated with blue, green and red colors respectively, are shown. The missing points correspond to the cases with law enforcement $\chi = 0.96, 3.86$ and, it is where the model could not be integrated numerically for a time $t = 200$ as observed for values $s < 0.45$, the maximum attractiveness magnitude, grows with the police presence, at least for case $\chi = 0.86$, i.e., attenuation in the attractiveness by law enforcement was expected, but in a nonintuitive response of the system, it was increased ($s < 0.45$). Reading this result is not easy and possibly not unique, but one interpretation is that criminal agents move relatively easily to hotspots, while police officers move by Laplacian diffusion and therefore are slower. Thus, the police agents slowly concentrate on some hotspots, but the criminals can create new hot zones without allowing the police agents to react adequately. For values $s > 0.45$, the maximum attractiveness is reduced by the police presence, which is an expected result. Fig. (b), representing the total attractiveness in Ω, shows similar behavior to Fig. (a). A rapid criminal diffusion based on Lévy flights, and a slow police response, have increased global attractiveness levels. It can be concluded that both graphs in Fig. 6 show two types of attractiveness response to law enforcement: First, for a certain intensity of Lévy flights, the attractiveness increases with the law enforcement, and second, the attractiveness is attenuated when the criminal diffusion is comparable to the police diffusion. It shows that different surveillance strategies should be evaluated to find an effective response of police agents to avoid criminal attacks.

Fig. 7 (a)-(b) presents stable attractiveness results $A(\mathbf{x}, t = 200)$, for the values of $s = 0.31$ with $\chi = 0.86$ and $s = 0.45$ with $\chi = 3.86$ respectively. These results correspond to the first points on the left of the graphs in Fig. 6 with $\chi > 0$. In (a), a ring with less angular symmetry is shown, and the intensity of attractiveness drops suddenly for a critical radius. In addition, isolated spots are observed inside the ring. In numerical tests for values of $s < 0.31$, these isolated points grow without limit. The attractiveness dynamic resulting in the spatial distribution observed in (a) is difficult to explain. However, a hypothesis is that a weak police presence in an environment of high criminal mobility fragments usual hotspots into a more complex structure. In Fig. (b), conventional hotspots are observed, the deterrent police influence can be appreciated too, in the attractiveness magnitude. However, a symmetry break has occurred. The upper right corner hotspot began to grow more than the rest. For $s < 0.45$ and $\chi = 3.86$, structures similar to case (a) appear, but they blow up before the integration time reaches $t = 200$.

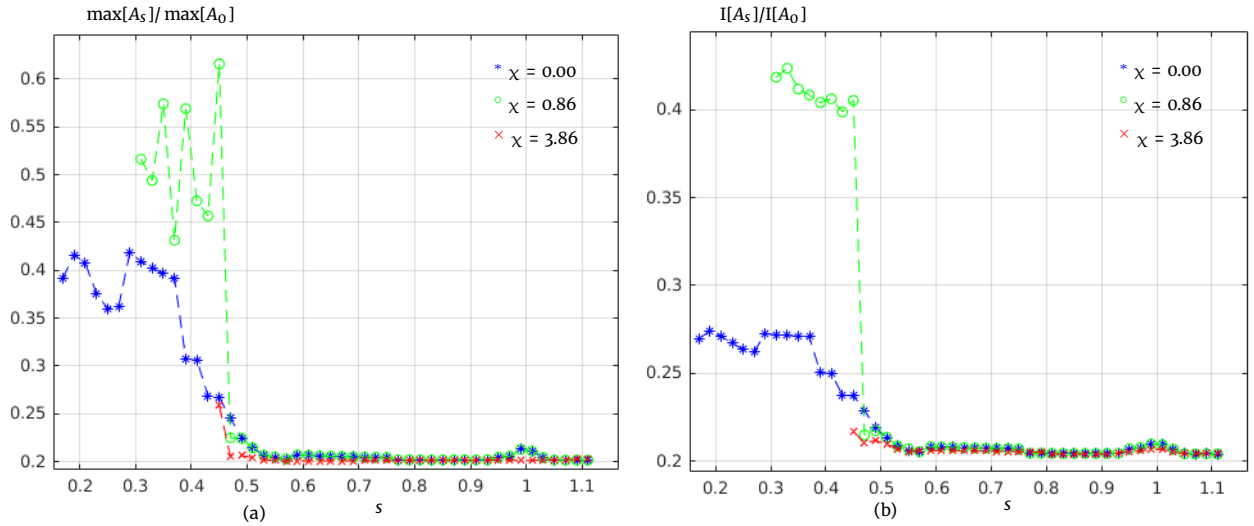

Figure 6. In both graphs the parameters are fixed in $T_c = 200$, $\eta = 3.94$, $\lambda = 0.05$, $\omega = 0.05$, $\Gamma = 0.019$, $\epsilon = 0.15$, $s \in [0.17, 1.20]$. (a) Evolution of max[A_s]/ max[A_0] (A_0 is the initial condition), Which is a measure of the maximum attractiveness values in Ω, for $\chi = 0.0, 0.86, 3.86$. Graph (b) shows I[A_s]/I[A_0], which represents a measure of total attractiveness in Ω to $\chi = 0.0, 0.86, 3.86$. Like the previous graph, the existence of two attractiveness regimes exists, the first ($s < 0.45$) is dominated by Lévy flights, and the second ($s > 0.45$) corresponds to a more conventional diffusion.

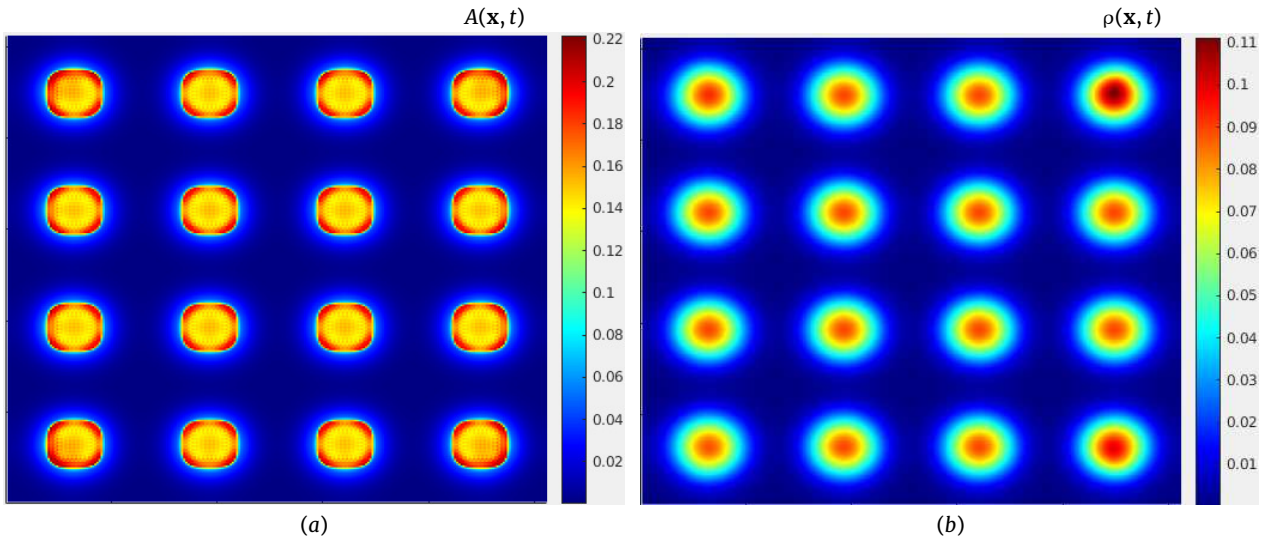

Figure 7. Spatial distribution for the $\chi = 3.86$ and $s = 0.31$ cases, the rest of the parameters are those specified in Fig. 6. (a) Field of attractiveness: A type of hotspot with a shape that varies from the classic one (circular) is visible. (b) The result of the integration is a more conventional hotspot distribution, however, some hotspots have started to grow more than others.

6 Conclusions

We have made a numerical study of the fractional model for the bi-dimensional case of home thieves dynamics, incorporating the police effect and using the Cops on dots strategy. The fractional operator was approximated through two-dimensional Fourier transform properties. It is observed that applying a Predictor-Corrector 4 schedule to a random initial attractiveness distribution, the number and hotspot magnitude are related to the derivative order s of the fractional operator. In a 1-dimensional scenario, stationary solutions analysis found that a series expansion and linear relations between series coefficients with derivative order are not adequate to approximate the functional relationship between attractiveness and criminal density population, inclusive for the small attractiveness amplitudes. A global properties analysis is made, the maximum and total attractiveness were used as estimators of the system evolution. The results from 2-dimensional scenarios reveal two regions with highly contrasting attractiveness behavior. The hypothesis is that Lévy flights dominate the powerful attractiveness region when derivative order ($s < 0.45$ super diffusive regimen). In the interval $s \in [0.45, 0.5]$, the dynamics combine the impact of Lévy flights with Laplacian diffusion. An appreciable variation emerges due to a smooth change in global maximums attractiveness for $s = 1$; It is explained by the functional form of the coefficient D_s. Still, the interpretation is that the local diffusion of criminal agents is based entirely on Brownian motion and produces its maximum effect on attractiveness. Incorporating dissuasive police effect into the model, maximums and total attractiveness are significantly reduced for $s > 0.5$. In case $s < 0.5$, which corresponds to a regimen where Lévy flights coexist or dominate, it is observed that surveillance type cops on the dots increase attractiveness levels in localized areas, with a more complex structure than hotspots. Also, it is interesting that the police presence induces an abrupt change in the system's evolution concerning the derivative order ($s < 0.5$). Numerical results with police influence showed an attractiveness distribution with a different symmetry than the classical hotspots with circular symmetry. However, a more detailed study is required to determine its dynamical properties. Extending the fractional model to the 2-dimensional case brings us closer to a possible application in realistic urban environments, implementing an optimal control investigation. Furthermore, it can be adequate for government agencies to identify attractive home zones and implement optimal surveillance strategies.

Nomenclature

Ω	2-dimension lattice
N	Size of Ω in each dimension
l	Lattice space
d	Position in coordinates (d_1, d_2), $d_1, d_2 = 1l, 2l, \ldots Nl$
t	time
$A_d(t)$	Attractiveness at position d at time t
A_d^0	Intrinsic attractiveness at site d
$B_d(t)$	Time t dependent attractiveness at site d
δt	Minimal time interval
$P_d(t)$	Probability of a criminal attack at site d in time δt
ϵ	Effectiveness of the attractiveness at site d
$E_d(t)$	Number of criminal attacks on site d during a time δt
θ	Enhancement in attractiveness for a single criminal agent attack
ω	Attractiveness time decay rate
η^*	Attractiveness influence in position d to its immediate neighbors
d'	Number of neighbors of position d
$n_d(t)$	Number of criminals at site d at time t
ϵ^*	Influence of the criminal presence in each position d
$\rho(\mathbf{x}, t)$	Criminal density in position $\mathbf{x}$ at time t
$\mathbf{x}$	Position in 2-dimension domain $x = (x_1, x_2)$
D	Dimension
$q_{i\to d}(t)$	Probability that a criminal will arrive at site d from i at time δt
$w_{i\to d}$	Relative weight of going from site i to site d
μ	Exponent of the underlying power law in the Lévy distribution
$\mathcal{L}$	Conventional fractional operator
Δ^s	Fractional operator derived from Lévy flight diffusion
s	Fractional order $s > 0$
$\zeta(\mu)$	Riemann function
$Z(\mu)$	Adapted function to the 2-dimensional fractional case
Γ	Crime population growth rate across all sites
λ	Rate of house burglars leaving without committing a crime in δt time
$A(\mathbf{x}, t)$	Attractiveness in position $\mathbf{x} = (x_1, x_2)$ at time t
$A_0(\mathbf{x})$	Initial condition of attractiveness
η	Rescaled attractiveness diffusion
γ	Rescaled Crime population growth rate
M	Criminal fractional diffusion
$I[A_s]$	Total attractiveness in $[0, 1] \times [0, 1]$
$\tilde{A}_d(t)$	Modified criminal attractiveness perception
χ	Police influence on criminal perception
$k_d(t)$	Expected police agents at site d at time t

Declarations

Consent for publication

Not applicable.

Conflicts of interest

The authors declare that they have no conflict of interests.

Funding

Not applicable.

Author's contributions

F.J.M-F.: Conceptualization, Methodology, Investigation, Writing-Original draft. A.A-S.: Software, Methodology, Data Curation, Writing-Original draft. R.R-C.: Visualization, Investigation, Software, Writing-Reviewing and Editing. A.H-H.: Methodology, Supervision. All authors discussed the results and contributed to the final manuscript.

Acknowledgements

F. J. Martínez-Farías was partially supported by the grant UAEHPTC764, DSA/5116/178021. We would like to thank the Supercomputing Laboratory of Apan Research Group "Energy Systems and Advanced Materials" for providing us access to supercomputing resources.

References

[1] Brantingham, P. & Tita, G. Offender Mobility and crime pattern formation from first principles. (In L. Liu, & J. Eck (Ed.), Artificial Crime Analysis Systems: Using Computer Simulations,2008). [CrossRef]
[2] Short, M., D'Orsogna, M., Pasour, V., Tita, G., Brantingham, P., Bertozzi, A. & Chayes, L. A Statistical Model of Criminal Behavior. *Mathematical Models And Methods In Applied Sciences*, 18, 1249-1267, (2008). [CrossRef]
[3] Short, M.B., Bertozzi, A.L., & Brantingham, P.J. Nonlinear patterns in urban crime: Hotspots, bifurcations, and suppression. *SIAM Journal on Applied Dynamical Systems*, 9(2), 462-483, (2010). [CrossRef]
[4] Jones, P.A., Brantingham, P.J., & Chayes, L.R. Statistical models of criminal behavior: the effects of law enforcement actions. *Mathematical Models and Methods in Applied Sciences*, 20(suppo1), 1397-1423, (2010). [CrossRef]
[5] Berestycki, H. & Nadal, J.P. Self-organised critical hot spots of criminal activity. *European Journal Of Applied Mathematics*, 21(4-5), 371-399, (2010). [CrossRef]
[6] Chaturapruek, S., Breslau, J., Yazdi, D., Kolokolnikov, T. & McCalla, S.G. Crime modeling with Lévy flights. *SIAM Journal On Applied Mathematics*, 73(4), 1703-1720, (2013). [CrossRef]
[7] Kolokolnikov, T., Ward, M. & Wei, J. The stability of steady-state hot-spot patterns for a reaction-diffusion model of urban crime. *Discrete And Continuous Dynamical Systems - Series B*, 19, 1373, (2014). [CrossRef]
[8] Zipkin, J.R., Short, M.B. & Bertozzi, A.L. Cops on the dots in a mathematical model of urban crime and police response. *Discrete And Continuous Dynamical Systems - Series B*, 19(5), 1479, (2014). [CrossRef]
[9] Camacho, A., Lee, H.R.L & Smith, L.M. Modelling policing strategies for departments with limited resources. *European Journal Of Applied Mathematics*, 27(3), 479-501, (2016). [CrossRef]
[10] Gu, Y., Wang, Q., & Yi, G. Stationary patterns and their selection mechanism of urban crime models with heterogeneous near-repeat victimization effect. *European Journal Of Applied Mathematics*, 28(1), 141-178, (2017). [CrossRef]
[11] Pan, C., Li, B., Wang, C., Zhang, Y., Geldner, N., Wang, L. & Bertozzi, A.L. Crime modeling with truncated Lévy flights for residential burglary models. *Mathematical Models And Methods In Applied Sciences*, 28(09), 1857-1880, (2018). [CrossRef]
[12] Wang, Q., Wang, D. & Feng, Y. Global well-posedness and uniform boundedness of urban crime models: One-dimensional case. *Journal Of Differential Equations*, 269(7), 6216-6235, (2020). [CrossRef]
[13] Rodríguez, N. & Winkler, M. Relaxation by nonlinear diffusion enhancement in a two-dimensional cross-diffusion model for urban crime propagation. *Mathematical Models And Methods In Applied Sciences*, 30(11), 2105-2137, (2020). [CrossRef]
[14] Kang, K., Kolokolnikov, T. & Ward, M. The stability and dynamics of a spike in the 1D Keller–Segel model. *IMA Journal Of Applied Mathematics*, 72(2), 140-162, (2007). [CrossRef]
[15] Mei, L. & Wei, J. The existence and stability of spike solutions for a chemotax is system modeling crime pattern formation. *Mathematical Models And Methods In Applied Sciences*, 30(09), 1727-1764, (2020). [CrossRef]
[16] Kondo, S. & Miura, T. Reaction-Diffusion Model as a Framework for Understanding Biological Pattern Formation. *Science*, 329(5999), 1616-1620, (2010). [CrossRef]
[17] Keller, E. & Segel, L. Traveling bands of chemotactic bacteria: A theoretical analysis. *Journal Of Theoretical Biology*, 30(2), 235-248, (1971). [CrossRef]
[18] Biler, P. & Wu, G. Two-dimensional chemotaxis models with fractional diffusion. *Mathematical Methods In The Applied Sciences*, 32(1), 112-126, (2009). [CrossRef]
[19] Calvó-Armengol, A. & Zenou, Y. Social Networks and Crime Decisions: The Role of Social Structure in Facilitating Delinquent Behavior. *International Economic Review*, 45(3), 939-958, (2004). [CrossRef]

[20] Nec, Y. Spike-Type Solutions to One Dimensional Gierer–Meinhardt Model with Lévy Flights. *Studies In Applied Mathematics*, 129(3), 272-299, (2012). [CrossRef]
[21] Cruz-García, S., Martínez-Farías, F., Santillán-Hernández, A. & Rangel, E. Mathematical home burglary model with stochastic long crime trips and patrolling: Applied to Mexico City. *Applied Mathematics And Computation*, 396, 125865, (2021). [CrossRef]
[22] Levajkovic, T., Mena, H. & Zarfl, M. Lévy processes, subordinators and crime modeling. *Novi Sad Journal Of Mathematics*, 46(2), 65-86, (2016).
[23] Cohen, L. & Felson, M. Social Change and Crime Rate Trends: A Routine Activity Approach. *American Sociological Review*, 44, 588-608, (1979). [CrossRef]
[24] Wilson, J.Q. & Kelling, G. L. Broken windows. *The Atlantic*, 249, 29-38, (1982).
[25] Kilbas, A.A., Srivastava, H.M. & Trujillo, J. *Theory and Applications of Fractional Differential Equations* (Vol. 204). Elsevier, North-Holland Mathematics Studies, (2006).
[26] Kopriva, D. *Implementing Spectral Methods for Partial Differential Equations*. Springer, (2009).
[27] Osgood, B.G. *Lectures on the Fourier Transform and Its Applications*. SIAM, (2019).
[28] Trefethen, L.N. Spectral methods in MATLAB, volume 10 of Software, Environments, and Tools. *Society for Industrial and Applied Mathematics (SIAM)*, Philadelphia, PA, 24, (2000).
[29] Butcher, J. Numerical Methods for Ordinary Differential Equations. John Wiley, 2015.
[30] Ghrist, M.L., Fornberg, B. & Reeger, J.A. Stability ordinates of Adams predictor-corrector methods. *BIT Numerical Mathematics*, 55(3), 733-750, (2015). [CrossRef]
[31] Lindfield, G.R. & Penny, J.E. Numerical methods: using MATLAB. Elsevier, 2012.
[32] Tadjeran, C. & Meerschaert, M.M. A second-order accurate numerical method for the two-dimensional fractional diffusion equation. *Journal Of Computational Physics*, 220(2), 813-823, (2007). [CrossRef]
[33] Lapidus, L. & Seinfeld, J. 4 Predictor-Corrector Methods. *Numerical Solution Of Ordinary Differential Equations*, 74, 152-241, (1971).
[34] Rodriguez, N., & Bertozzi, A. Local existence and uniqueness of solutions to a PDE model for criminal behavior. *Mathematical Models and Methods in Applied Sciences*, 20(supp01), 1425-1457, (2010). [CrossRef]
[35] Cantrell, R.S., Cosner, C. & Manásevich, R. Global Bifurcation of Solutions for Crime Modeling Equations. *SIAM Journal On Mathematical Analysis*, 44(3), 1340-1358, (2012). [CrossRef]
[36] Tse, W.H. & Ward, M.J. Hotspot formation and dynamics for a continuum model of urban crime. *European Journal Of Applied Mathematics*, 27(3), 583-624, (2016). [CrossRef]
[37] Rodríguez, N., Wang, Q. & Zhang, L. Understanding the Effects of On- and Off-Hotspot Policing: Evidence of Hotspot, Oscillating, and Chaotic Activities. *SIAM Journal On Applied Dynamical Systems*, 20(4), 1882-1916, (2021). [CrossRef]

Mathematical Modelling and Numerical Simulation with Applications (MMNSA) (https://www.mmnsa.org)

Mathematical Modelling and Numerical Simulation with Applications, 2022, 2(1), 41–47

https://www.mmnsa.org
ISSN Online: 2791-8564 / Open Access
https://doi.org/10.53391/mmnsa.2022.01.004

RESEARCH PAPER

Three-dimensional fractional system with the stability condition and chaos control

Molood Gholami[1,‡], Reza Khoshsiar Ghaziani[1,‡] and Zohreh Eskandari[1,*,‡]

[1]Department of Mathematical Sciences, Shahrekord University, Shahrekord, Iran

*Corresponding Author
‡moloodgholami1370@gmail.com (Molood Gholami); khoshsiar@sci.sku.ac.ir (Reza Khoshsiar Ghaziani); z.eskandari@sku.ac.ir (Zohreh Eskandari)

Abstract

A three-dimensional system is introduced in this paper and its local stability is analyzed. Our study establishes the validity and uniqueness of the linear feedback control for the proposed system and proves its existence and uniqueness. The numerical simulation algorithm described by Atanackovic and Stankovic is finally applied. The analytical results are analyzed and the dynamics of the system are explored in more detail.

Key words: Fractional-order system; stability; control; chaotic system
AMS 2020 Classification: 34A08; 34C23; 34H10

1 Introduction

Modeling and investigating actual phenomena can be accomplished with fractional dynamical systems. A dynamical system may exhibit chaos as one of its important dynamics. Dynamical chaos disappears when the fractional order falls below a threshold in a fractional-order chaotic system. There have been several articles discussing the minimum effective dimension below which the system remains chaotic, [1, 2, 3, 4, 5, 6, 7].

Chaos theory is a field of mathematics that has already attracted the attention of many researchers from different fields of science, engineering and medicine. Chaos theory describes the behavior of certain dynamical systems whose state evolves with time and are highly sensitive to initial conditions. Because of the complexity of chaotic behavior in dynamical systems, it finds applications in a variety of fields, such as science, technology and medicine [8, 9, 10, 11, 12, 13, 14]. Studying chaotic systems can be a very valuable endeavor. Sene [15] in his paper studied the applications of the fractional-order chaotic system in the sense of Caputo fractional derivative. The presence or absence of chaotic behaviors of their model was presented in terms of the Lyapunov exponents. For the model description, the circuit schematic was drawn and simulated. Naik et al. [16] in their paper studied the chaotic dynamics of a fractional-order cancer model. A detailed analysis of the equilibrium points was also considered. They also calculated the Lyapunov exponents that give the existence of chaotic behavior of the model.

Leibniz in 1695 was the first to introduce the fractional calculus followed by Liouville in 1834, Riemann in 1892 and others [17]. Fractional calculus represents the generalization of integrals and derivatives to non-integer order. After Leibniz fractional calculus has gained increasing popularity and finds applications in various fields of science, technology and medicine [18, 19, 20, 21, 22, 23]. Recently, Ozkose and Yavuz [24] in their paper studied in fractional-order case the relations between COVID-19 and diabetes diseases under the hereditary traits then validated their model by the real data from Turkey. The Adams-Bashforth-Moulton predictor-corrector method was employed for the numerical solution of their model. For the advantages of the fractional-order derivative, they considered the memory trace and hereditary traits in the model. Fractional model, similar electrode-electrolyte, electromagnetic, and wave models have been found to

➤ **Received:** 04.11.2021 ➤ **Revised:** 05.02.2022 ➤ **Accepted:** 08.02.2022 ➤ **Published:** 16.02.2022

explain many systems in the physical, chemical, and biological processes.

The rest of the paper is decorated as: after the introduction in Section 1, Section 2 gives some preliminaries and discusses a chaotic three-dimensional system. Section 3 examines whether or not a proposed system solution exists and is unique. In Section 4, we introduced the stability conditions of the equilibrium points of the system. The linear feedback control system studied in Section 5 is based on the Routh-Hurwitz method. In Section 6, we present numerical simulations based on algorithmic methods and discuss the obtained results. Finally, in Section 7, we conclude the study.

2 Preliminaries

Many well known fractional derivatives including Riemann-Liouville, Grunwald-Letnikov as well as Caputo exist in the literature and are all common fractional derivative definitions. As a result, we investigate the fractional derivative of Caputo, as defined in [25]:

$$D^{\eta}g(\tau) = \frac{1}{\Gamma(m-\eta)}\int_0^t (\tau-\sigma)^{m-\eta-1}g^{(m)}(\sigma)d\sigma \tag{1}$$

$$= j^{m-\eta}\left(\frac{d^m}{d\tau^m}g(\tau)\right). \tag{2}$$

It is defined as follows: m is integer, $m-1<\eta<m$ and Γ is the Gamma function, and j^{θ} is Riemann-Liouville integral operator.

$$j^{\theta}g(\tau) = \frac{1}{\Gamma(\theta)}\int_0^t (\tau-\sigma)^{\theta-1}g^{(m)}(\sigma)d\sigma, \quad \tau>0. \tag{3}$$

Theorem 1 *[26] An autonomous linear system*

$$D^{\eta}x = Lx, \qquad x(0)=x_0,$$

where L is a $m\times m$ matrix and $0<\eta<1$ is asymptotically stable if and only if $|\arg(\mu)|>\frac{\eta\pi}{2}$ for all eigenvalues μ of L. The components of the solution $x(\tau)$ decay to zero in this case, each component of solution $x(\tau)$ decays toward or like $\tau^{-\eta}$. Also, this linear system is stable if and only if $|\arg(\mu)|\geq\frac{\eta\pi}{2}$ and those critical eigenvalues that satisfy $|\arg(\mu)|=\frac{\eta\pi}{2}$ that geometric multiplication is one. In Ref. [27], a chaotic system in three dimensions is described by:

$$\begin{cases} x_1'(\tau) = ax_1 - x_2x_3, \\ x_2'(\tau) = -bx_2 + x_1x_3, \\ x_3'(\tau) = -cx_3 + x_1^2, \end{cases} \tag{4}$$

where x_1, x_2, x_3 are state variables, $a, b, c\in\mathbb{R}^+$ are constant parameters. For $a=6, b=12, c=14$, the chaotic attractors for system (4) are displayed in Fig. 1.

Three equilibrium points exist in the system

$$O=(0,0,0), \quad Q_1 = \left(\sqrt[4]{abc^2}, \sqrt[4]{a^3c^2/b}, \sqrt{ab}\right), \quad Q_2 = \left(-\sqrt[4]{abc^2}, -\sqrt[4]{a^3c^2/b}, -\sqrt{ab}\right).$$

3 Solution's existence and uniqueness

Taking into account the initial value problem:

$$D^{\eta}W(\tau) = g(\tau, W(\tau)), \quad 0<\tau<\Omega, \quad W^{(k)}(0) = W_0^{(k)}, \quad k=0,1,\ldots,m-1. \tag{5}$$

Theorem 2 *(Existence [28]) Let us consider*

$$E := [0, W^*]\times[W_0^{(0)}-\varepsilon, W_0^{(0)}+\varepsilon],$$

with some $W^*>0$ and some $\varepsilon>0$, and the function $g: E\to\mathbb{R}$ $\chi := \min\{\chi^*, (\varepsilon\Gamma(\eta+1)/||g||_{\infty}^{\frac{1}{\eta}}\}$. Then, there exists a function $W:[0,\chi]\to\mathbb{R}$ which solves the initial value problem (5).

Theorem 3 *(Uniqueness [28]) Let us consider*

$$E := [0, \chi^*]\times[W_0^{(0)}-\varepsilon, W_0^{(0)}+\varepsilon],$$

with some $\chi^*>0$ and some $\varepsilon>0$. Therefore the function $f: E\to\mathbb{R}$ is surrounded on E and regard the second variable, meet the Lipschitz condition, i.e.,

$$|g(\tau, W) - g(\tau, V)| \leq J|W-V|,$$

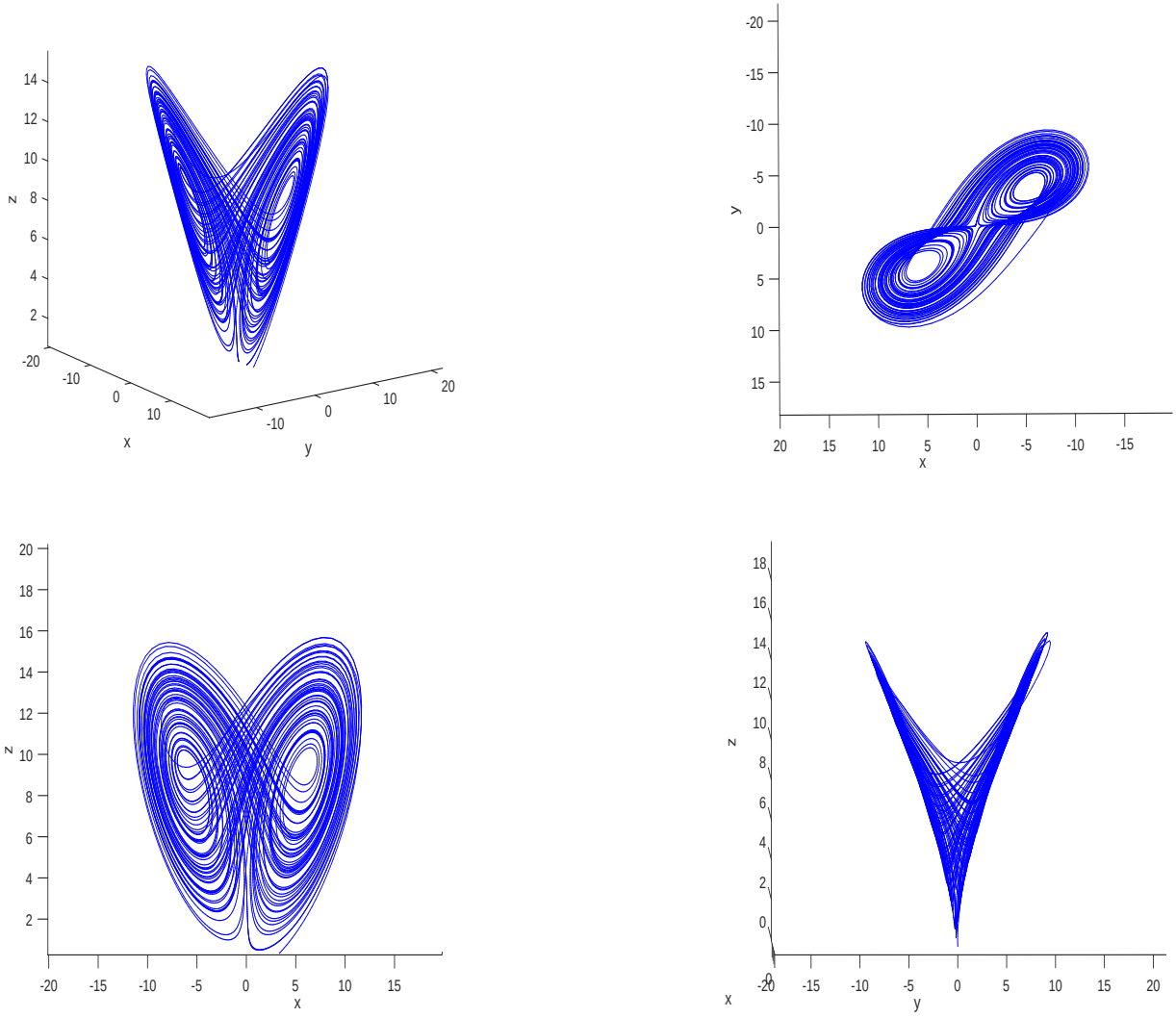

Figure 1. The chaotic attractors for system (4)

with constant $J > 0$ independent τ, W and V. Then, describe χ as Theorem (2), there exists one function $W : [0, \chi] \to \mathbb{R}$ solving the initial value problem (5).

Theorem 4 *In the fractional-order three-dimensional system (4), the initial value problem can be expressed as follows:*

$$D^{\eta}x(\tau) = Ax(\tau) + x_1(\tau)Bx(\tau) + x_2(\tau)Cx(\tau), \qquad x(0) = x_0, \tag{6}$$

where $0 < \tau < \Omega, x(\tau) = (x_1(\tau), x_2(\tau), x_3(\tau))^{\Omega} \in \mathbb{R}^3, x(0) = (x_{10}, x_{20}, x_{30})$

$$A = \begin{pmatrix} a & 0 & 0 \\ 0 & -b & 0 \\ 0 & 0 & -c \end{pmatrix}, \quad B = \begin{pmatrix} 0 & 0 & 0 \\ 0 & 0 & 1 \\ 1 & 0 & 0 \end{pmatrix}, \quad C = \begin{pmatrix} 0 & 0 & -1 \\ 0 & 0 & 0 \\ 0 & 0 & 0 \end{pmatrix}.$$

If

$$\Omega := \min\{\Omega^*, (\varepsilon\Gamma(\eta + 1)/||g||_{\infty})^{\frac{1}{\eta}}\}, \quad \Omega^* > 0,$$

there exists a unique solution for (6).

Proof Consider

$$g(x(\tau)) = A\,x(\tau) + x_1(\tau)Bx(\tau) + x_2(\tau)Cx(\tau), \quad x(\tau) \in [0, \Omega^*] \times [x_0 - \varepsilon, x_0 + \varepsilon],$$

for any Ω^*, $\varepsilon > 0$. Moreover, one has

$$\begin{aligned} |g(x) - g(y)| &= |A(x-y) + x_1Bx - y_1By + x_2Cx - y_2Cy| \\ &\leq ||A||(x-y)| + |x_1Bx - y_1By| + |x_2Cx - y_2Cy|, \end{aligned} \tag{7}$$

where $y(\tau) \in [0, \Omega^*] \times [x_0 - \varepsilon, x_0 + \varepsilon]$, and $|\cdot|$ represents the matrix vector norm. Clearly

$$\begin{aligned} |x_1Bx - y_1By| &= |x_1Bx - y_1Bx + y_1Bx - y_1By| \\ &= |(x-x)-)Bx + y_1B(x-y)| \\ &\leq ||B||(|x| + |y_1|)(|x-y|). \end{aligned}$$

Likewise, one has the following result:

$$|x_2Cx - y_2Cy| \leq ||C||(|x| + |y_2|)(|x-y|).$$

Eq. (7) gives the result that

$$\begin{aligned} |g(x) - g(y)| &\leq [||A|| + ||B||(|x| + |y_1|) + ||C||(|x| + |y_2|)](|x-y|) \\ &\leq [||A|| + (||B|| + ||C||)(2|x_0| + 2\epsilon)](|x-y|) \\ &\leq L(||x-y||), \end{aligned}$$

where $J = ||A|| + (||B|| + ||C||)(2|x_0| + 2\varepsilon) > 0$. Hence, the fractional-order dimensional system is Lipschitz-satisfying. Then, compatible to the existence and uniqueness theorem of the fractional-order dimensional system the initial value problem of the commensurate order system (6) has a unique solution in the interval

$$\Omega := \min\{\Omega^*, (\varepsilon\Gamma(\eta+1)/||g||_\infty))^{\frac{1}{\eta}}\}.$$

■

4 Conditions for the stability of equilibrium points

The characteristic equation of system (4) is determined by

$$p(\mu) = \mu^3 + r_1\mu^2 + r_2\mu + r_3 = 0, \tag{8}$$

whose discriminant $D(p)$ is defined by

$$D(p) = R(p, p'), \tag{9}$$

and

$$D(p) = 18r_1r_2r_3 + r_1^2r_2^2 - 4r_3r_1^3 - 4r_2^3 - 27r_3^2. \tag{10}$$

If Δ_1, Δ_2 and Δ_3 are Routh-Hurwitz determinants $\Delta_1 = r_1$, $\Delta_2 = \begin{vmatrix} r_1 & 1 \\ r_3 & r_2 \end{vmatrix}$ and $\Delta_3 = r_3$. Thus we have the following stability conditions [28].
(I) If $D(p) < 0$, $a_1 > 0$, $a_2 > 0$, $a_1a_2 = a_3$, then the equilibrium point is locally asymptotically stable for all $\eta \in (0, 1)$.
(II) The condition $r_3 > 0$, is the necessary condition for the equilibrium point to be locally asymptotically stable.

Some stability conditions for the equilibrium points Q_0, Q_1 and Q_2

The characteristic polynomial of equilibrium point Q_0 is given by:

$$p(\mu) = \mu^3 + \mu^2(c + b - a) + \mu(bc - ac) - abc. \tag{11}$$

It is clear that $r_3 = -abc < 0$, thus applying the stability condition (II) to characteristic equation (11) implies that E_0 in unstable. Similary, the equilibrium point Q_1 and Q_2 have the same characteristic polynomial, which given as:

$$p(\mu) = \mu^3 + (c + b - a)\mu^2 + (ac + bc)\mu + 4abc = 0. \tag{12}$$

Thus, applying the Routh-Hurwitz conditions and the necessary stability condition part (I), imply that equilibrium points Q_1, Q_2 are unstable.

5 Linear feedback control of the chaotic system

Here, the control of fractional three-dimensional chaotic system (4) is discussed by using the linear feedback control.
The controlled fractional order chaotic system (4) is given by:

$$\begin{cases} D^{\eta}x_1(t) = ax_1 - x_2x_3 - k_1(x_1 - \bar{x}_1) \\ D^{\eta}x_2(t) = -bx_2 + x_1x_3 - k_2(x_2 - \bar{x}_2) \\ D^{\eta}x_3(t) = -cx_3 + x_1^2 - k_3(x_3 - \bar{x}_3), \end{cases} \tag{13}$$

where (k_1, k_2, k_3) are feedback control and $k_1, k_2, k_3 > 0$ and by suitable choice of feedback control according to stability conditions (I, II), we can drive the system (13) trajectories to unstable equilibrium point Q_1.

Controlling chaos for the equilibrium point Q_1

In this section, we apply stability condition of chaotic system to study chaos control. For this, we obtain the characteristic equation of the controlled system (13) evaluated at the equilibrium point by:

$$\mu^3 + \mu^2(s_1 + s_2 + k_2 + b) + \mu(s_1s_2 + 2bs_2 + k_2s_1 + k_2s_2) + (s_1s_2)k_2 + bs_1(c + k_2), \tag{14}$$

where $s_1 = (k_1 - a)$ and $s_2 = (k_3 + c)$. By applying the Routh-Hurwitz conditions (I, II) to equilibrium point (13) we find that: k_1, k_2, k_3, are all positive and defined by equation (13).
Furthermore, the inequality is enough conditions for stabilizing the controlled system (13) to the equilibrium point Q_1 and Q_2: In the system (13) we consider the fixed parameters $a = 6$, $b = 12$, $c = 4$ and using the feedback control gains $(k_1, k_2, k_3) = (2.88, 1.33, 0.52)$.
For the above mentioned value parameters and feedback control gains, it becomes clear that the trajectories of controlled system (13) with fractional order η converge to the equilibrium point Q_1.
Fig. 2 shows the trajectories of controlled fractional system for $\eta = 0.98$, which converges to the equilibrium point Q_1.
However, when $\eta = 1$ the controlled system (13) is not stable near equilibrium point Q_1 (see Fig. 3).

6 Numerical simulations and discussion

For solving system (4), we employ a numerical technique developed by Atanackovic and Stankovic [29] to solve the fractional differential equation, and we depict trajectories of system (4) using the well known Runge-Kutta method of order fourth for parameters $a = 6$, $b = 12$, $c = 4$. We have the equilibrium point $Q_1 = (135.764, 67.882, 8.485)$ and $Q_2 = (-135.764, -67.882, -8.485)$.
Fig. 1 presents numerical values for system (4) for different values. An analysis of the local stability of a three-dimensional system is presented in this paper. This study aims to verify the validity and uniqueness of linear feedback control for the proposed system and prove its existence and uniqueness. An algorithm is finally applied to the numerical simulation.

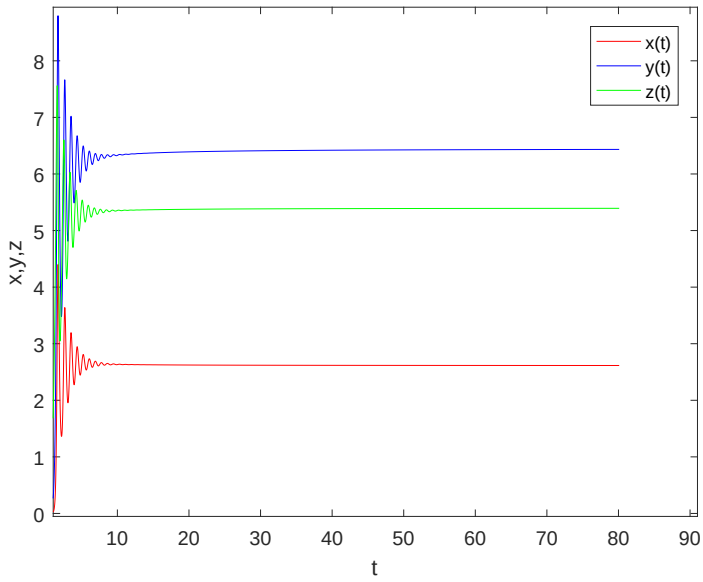

Figure 2. The trajectories of the controlled system (13) by $\eta = 0.98$

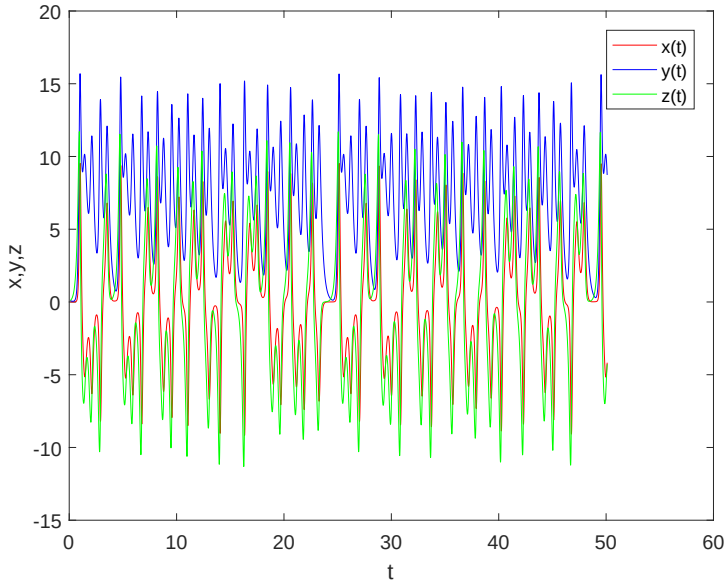

Figure 3. The trajectories of the controlled system (13) by $\eta = 1$

7 Conclusions

In the present paper, we examined a three-dimensional fractional order chaotic system. The conditions that ensure the existence and uniqueness of its solution were identified. We employed Routh-Hurwitz method to determine the stability conditions. We also employed the feedback control of the chaotic system with fractional order. Through the numerical simulations, the performance and authenticity of the proposed method were presented. The trajectories of the model (4) through the well known Runge-Kutta method of order fourth were depicted. It is concluded from the obtained results that the fractional power of the derivative has a significant effect on the dynamic process. Also, it is observed that the smaller fractional power of the derivative is the chaotic behavior of the system.

Declarations

Consent for publication

Not applicable.

Conflicts of interest

The authors declare that they have no conflict of interests.

Funding

Not applicable.

Author's contributions

M.G.: Conceptualization, Methodology, Software, Writing-Original draft. R.K.G.: Conceptualization, Methodology, Supervision, Investigation. Z.E.: Software, Methodology, Data Curation. All authors discussed the results and contributed to the final manuscript.

Acknowledgements

Not applicable.

References

[1] Allegretti, S., Bulai, I.M., Marino, R., Menandro, M.A., & Parisi, K. Vaccination effect conjoint to fraction of avoided contacts for a Sars-Cov-2 mathematical model. *Mathematical Modelling and Numerical Simulation with Applications*, 1(2), 56-66, (2021). [CrossRef]

[2] Özköse, F., Şenel, M.T., & Habbireeh, R. Fractional-order mathematical modelling of cancer cells-cancer stem cells-immune system interaction with chemotherapy. *Mathematical Modelling and Numerical Simulation with Applications*, 1(2), 67-83, (2021). [CrossRef]

[3] Ikram, R., Khan, A., Zahri, M., Saeed, A., Yavuz, M., & Kumam, P. Extinction and stationary distribution of a stochastic COVID-19 epidemic model with time-delay. *Computers in Biology and Medicine*, 141, 105115, (2022). [CrossRef]

[4] Özköse, F., Yılmaz, S., Yavuz, M., Öztürk, İ., Şenel, M.T., Bağcı, B.Ş., ... & Önal, Ö. A Fractional Modeling of Tumor–Immune System Interaction Related to Lung Cancer with Real Data. *The European Physical Journal Plus*, 137(1), 1-28, (2022). [CrossRef]
[5] Oud, M.A.A., Ali, A., Alrabaiah, H., Ullah, S., Khan, M.A., & Islam, S. A fractional order mathematical model for COVID-19 dynamics with quarantine, isolation, and environmental viral load. *Advances in Difference Equations*, 2021(1), 1-19, (2021). [CrossRef]
[6] Ali, A., Alshammari, F.S., Islam, S., Khan, M. A., & Ullah, S. Modeling and analysis of the dynamics of novel coronavirus (COVID-19) with Caputo fractional derivative. *Results in Physics*, 20, 103669, (2021). [CrossRef]
[7] Ali, A., Islam, S., Khan, M.R., Rasheed, S., Allehiany, F.M., Baili, J., ... & Ahmad, H. Dynamics of a fractional order Zika virus model with mutant. *Alexandria Engineering Journal*, 61(6), 4821-4836, (2021). [CrossRef]
[8] Hammouch, Z., Yavuz, M., & Özdemir, N. Numerical solutions and synchronization of a variable-order fractional chaotic system. *Mathematical Modelling and Numerical Simulation with Applications*, 1(1), 11-23, (2021). [CrossRef]
[9] Daşbaşı, B. Stability analysis of an incommensurate fractional-order SIR model. *Mathematical Modelling and Numerical Simulation with Applications*, 1(1), 44-55, (2021). [CrossRef]
[10] Naik, P.A., Yavuz, M., Qureshi, S., Zu, J., & Townley, S. Modeling and analysis of COVID-19 epidemics with treatment in fractional derivatives using real data from Pakistan. *The European Physical Journal Plus*, 135(10), 1-42, (2020). [CrossRef]
[11] Naik, P.A., Owolabi, K.M., Yavuz, M., & Zu, J. Chaotic dynamics of a fractional order HIV-1 model involving AIDS-related cancer cells. *Chaos, Solitons & Fractals*, 140, 110272, (2020). [CrossRef]
[12] Naik, P.A. Global dynamics of a fractional-order SIR epidemic model with memory. *International Journal of Biomathematics*, 13(08), 2050071, (2020). [CrossRef]
[13] Alidousti, J., & Eskandari, Z. Dynamical behavior and Poincare section of fractional-order centrifugal governor system. *Mathematics and Computers in Simulation*, 182, 791-806, (2021). [CrossRef]
[14] Naik, P.A., Eskandari, Z., & Shahraki, H.E. Flip and generalized flip bifurcations of a two-dimensional discrete-time chemical model. *Mathematical Modelling and Numerical Simulation with Applications*, 1(2), 95-101, (2021). [CrossRef]
[15] Sene, N. Study of a Fractional-Order Chaotic System Represented by the Caputo Operator. *Complexity*, 2021, Article ID 5534872, (2021). [CrossRef]
[16] Naik, P.A., Zu, J. & Naik, M. Stability analysis of a fractional-order cancer model with chaotic dynamics. *International Journal of Biomathematics*, 14(6), 2150046, (2021). [CrossRef]
[17] Magin, R. Fractional calculus in bioengineering. *Critical Reviews in Biomedical Engineering*, 32(1), 1-104, (2004). [CrossRef]
[18] Naik, P.A., Yavuz, M. & Zu, J. The role of prostitution on HIV transmission with memory: A modeling approach. *Alexandria Engineering Journal*, 59(4), 2513-2531, (2020). [CrossRef]
[19] Naik, P.A., Zu, J. & Owolabi, K. Global dynamics of a fractional order model for the transmission of HIV epidemic with optimal control. *Chaos Solitons & Fractals*, 138, 109826, (2020). [CrossRef]
[20] Naik, P.A., Owolabi, K.M, Zu, J. & Naik, M. Modeling the transmission dynamics of COVID-19 pandemic in Caputo type fractional derivative. *Journal of Multiscale Modelling*, 12(3), 2150006-107, (2021). [CrossRef]
[21] Yavuz, M. & Sene, N. Fundamental calculus of the fractional derivative defined with Rabotnov exponential kernel and application to nonlinear dispersive wave model. *Journal of Ocean Engineering and Science*, 6(2), 196-205, (2021). [CrossRef]
[22] Yavuz, M., Sulaiman, T.A., Usta, F. & Bulut, H. Analysis and numerical computations of the fractional regularized long-wave equation with damping term. *Mathematical Methods in the Applied Sciences*, 44(9), 7538-7555, (2021). [CrossRef]
[23] Sene, N. Second-grade fluid with Newtonian heating under Caputo fractional derivative: analytical investigations via Laplace transforms. *Mathematical Modelling and Numerical Simulation with Applications*, 2(1), 13-25, (2022). [CrossRef]
[24] Ozkose, F. & Yavuz, M. Investigation of interactions between COVID-19 and diabetes with hereditary traits using real data: A case study in Turkey. *Computers in Biology and Medicine*, 141, 105044, (2022). [CrossRef]
[25] Caputo, M. Linear models of dissipation whose Q is almost frequency independent—II. *Geophysical Journal International*, 13(5), 529-539, (1967). [CrossRef]
[26] Matignon, D. (1996, July). Stability results for fractional differential equations with applications to control processing. In *Computational engineering in systems applications* (Vol. 2, No. 1, pp. 963-968).
[27] Lai, Q., & Wang, L. Chaos, bifurcation, coexisting attractors and circuit design of a three-dimensional continuous autonomous system. *Optik*, 127(13), 5400-5406, (2016). [CrossRef]
[28] Ahmed, E., El-Sayed, A.M.A., & El-Saka, H.A. On some Routh–Hurwitz conditions for fractional order differential equations and their applications in Lorenz, Rössler, Chua and Chen systems. *Physics Letters A*, 358(1), 1-4, (2006). [CrossRef]
[29] Atanackovic, T.M., & Stankovic, B. On a numerical scheme for solving differential equations of fractional order. *Mechanics Research Communications*, 35(7), 429-438, (2008). [CrossRef]

Mathematical Modelling and Numerical Simulation with Applications, 2022, 2(1), 48–58

https://www.mmnsa.org
ISSN Online: 2791-8564 / Open Access
https://doi.org/10.53391/mmnsa.2022.01.005

RESEARCH PAPER

Shock absorber system dynamic model in model-based environment

Nafi Kulaksiz[1,§], Sevval Cip[1,§], Zeynep Gedikoglu[1,§] and Muhsin Hancer[2,*,§]

[1]Department of Aeronautical Engineering, Necmettin Erbakan University, 42140, Konya, Turkey, [2]Department of Astronautical Engineering, Necmettin Erbakan University, 42140, Konya, Turkey

*Corresponding Author
§ nafikulaksiz@gmail.com (Nafi Kulaksiz); sevvallcip@gmail.com (Sevval Cip); zgedikogluu@gmail.com (Zeynep Gedikoglu); mhancer@erbakan.edu.tr (Muhsin Hancer)

Abstract

This paper addresses the mathematical modelling of aircraft landing gear based on the shock absorber system's dynamics and examination of results depending on different touchdown scenarios and design parameters. The proposed methodology relies on determining an analytical formulation of the shock absorber system's equation of motion, modelling this formulation on the model-based environment (Matlab/Simulink), and integrating with an accurate aircraft nonlinear dynamic model to observe the performance of landing gear in different touchdown or impact velocities. A suitable landing performance depends on different parameters which are related to the shock absorber system's working principle. There are three subsystems of the main system which are hydraulic, pneumatic, and tire systems. Subsystems create a different sort of forces and behaviors. The air in the pneumatic system is compressed by the impact effect so it behaves like a spring and creates pneumatic or air spring force so the most effective parameter in this structure is determined as initial air volume. Hydraulic oil in the receptacle of the hydraulic system flow in an orifice hole when impact occurs so it behaves as a damper and creates damping or hydraulic force. The same working principle is acceptable for the air in the tire. The relationship between tire and ground creates a friction force based on dynamic friction coefficient depending on aircraft dynamics. As a result of this study effect of the impact velocity and initial air volume parameters on the system are examined and determined by optimization according to maximum initial load limits of aircraft and displacement of strut and tire surface.

Key words: Shock absorber; landing-touchdown performance; oleo-pneumatic and strut; aircraft landing loads
AMS 2020 Classification: 37M05; 37N35; 93C10; 93C35.

1 Introduction

Shock absorber systems have essential roles in aircraft structure. Accidents occur during both landing and takeoff. Shock absorber systems in landing gear can absorb the touchdown loads. This system needs to be designed and controlled as it can provide a health touchdown condition before the manufacturing process. There are two controlling ways observe the system's qualification. The first one is an empirical way that needs to test apparatuses [1]. Applying this way is expensive because there is a mechanic system to observe touchdown condition. The second way is the analytic or simulation method. In this method, the dynamics of shock absorber systems, equations of motions, tire behaviors etc. are simulated in computer programs (Matlab/Simulink) [2, 3, 4, 5].
In addition, according to international regulations and literature, there are a few landing conditions (three-point landing, two-point landing) [6, 7, 8]. These conditions directly affect the response of the system. In one-gear landing conditions, the aircraft is in the level

➤ **Received:** 15.02.2022 ➤ **Revised:** 26.03.2022 ➤ **Accepted:** 31.03.2022 ➤ **Published:** 31.03.2022

attitude. In this condition aircraft contact the runway on one main landing gear and touchdown velocity is the most important parameter for the shock absorber to healthy landing. In two-point landing conditions, load factors and pitching accelerations are changed by time. Main gear landing loads are critical in this condition. Changes in load factors are caused to differences in landing gear systems design parameters. Examples of these parameters are hydraulic characteristics and oleo length. In three-point landing conditions, pitching acceleration is equal to zero. the nose gear system and its structures are generally critical in this condition and the nose landing gear carries %15 of the total weight of the aircraft in the static position [9]. One of the main function of the landing gear systems is the compensation of the maximum critical load. The critical parameter which is the most important input to the model is a vertical component of touchdown velocity. It directly affects the motion. Some experiments show the critical touchdown velocity is between the $3 - 5\ m/s$ [10].

The discharge coefficient which is determining the buffer damping force is generally determined between 0.8-0.82 which is related to the hydraulic flow motion [1]. The oleo-pneumatic shock absorber system has a few subsystems. In this system, the air is directly used to store the impact energy. Air works like a spring and produces a spring force (air spring force). Air spring force depends on a few parameters. For instance, the initial pressure of air which is generally determined firstly is can be calculating if the air vehicle mass is known. So, initial pressure is a main design parameter. Desired air spring deflection is observed in static position of the air vehicle may determine this parameter. The other store part for impact energy is the hydraulic damping. The behavior of hydraulic oil during corresponding impact force is the product of hydraulic force. The tire which is working as a spring is needed to bear all produced forces. The tire spring characterize is the most important parameter that can directly affect the tire behavior [11].

Different coefficients of friction in different runway conditions cause frictional force variation between the aircraft and the runway. Change in friction force affects the friction force which is normal to the axis of the shock strut and friction force at the tire in the horizontal direction. The dynamic friction coefficient between the tire and the runway is not a constant value and can be expressed as a dependent function of forward velocity (u), the forward speed of the aircraft in the x direction. There is an inverse proportion between forward speed and dynamic friction coefficient.

the shock absorber landing gear system is simulated with the integration of aircraft non-linear dynamic model in this paper. The most important parameter that is impact velocity, is considered when landing maneuver scenarios creates. In this study, we want to develop a generical model of the nose and main landing gears.

2 Methodology

In this section, the oleo-pneumatic shock strut system dynamic is explained and modelled. Figure 1 shows the schematic view of the oleo-pneumatic shock strut where A_a is the net pneumatic area, A_n is the net orifice area, A_h is the net hydraulic area.

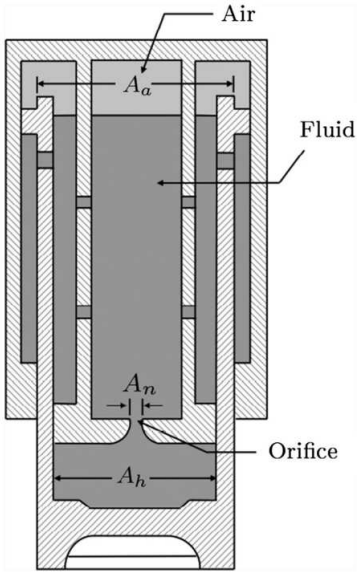

Figure 1. Schematic view of the oleo-pneumatic shock strut [15].

Mathematical model

Pneumatic force

The mathematical model of the pneumatic force in shock strut is given as:

$$F_a = A_a P_{a_0} \left(\frac{v_o}{v_0 - S_s A_a} \right)^n, \tag{1}$$

$$S_s = \frac{Z_1 - Z_2}{cos\phi}, \tag{2}$$

where F_a is the pneumatic force (air-spring force), A_a is the pneumatic area, p_{a_0} is the initial strut air pressure, v_0 is the initial air volume, n is the effective polytropic exponent for the nitrogen-compression process, S_s is the deflection of the shock strut, Z_1 and Z_2 are the vertical displacement of sprung (aircraft structure) and the unsprung mass respectively and α is the anteversion angle of the strut [12, 13].

There are many reasons why nitrogen is used instead of air in the damper system. Firstly, since the air contains oxygen and hydrogen, moisture formation may be observed during operation and this may increase the risk of cavitation. Therefore, using nitrogen is more advantageous. Secondly, during operation, the nitrogen internal pressure is more consistent than the air internal pressure. Thirdly, since the density of nitrogen is greater than the density of air, it can keep the damper pressure longer period of time. Finally, since nitrogen is an inert gas, it does not react with other damper components [14].

Hydraulic force

The main orifice hydraulic force is:

$$F_h = \rho \left(\frac{A_h^3}{2A_0^2 C_d^2} \right) |\dot{S}|\dot{S}, \tag{3}$$

$$\frac{1}{C_d} = \frac{1}{0.827 - 0.0085\frac{l}{d}} + \frac{20}{R_e}\left(1 + 2.25\frac{l}{d}\right), \tag{4}$$

where F_h is the hydraulic force, ρ is the density of the fluid, A_h is the hydraulic area, A_0 is the sectional area of the orifice inlet, C_d is the discharge coefficient, $\dot{S}$ is the stroke telescoping velocity, R_e is the Reynold number, l is the orifice length, d is the orifice diameter. Hydraulic force is the measurement of the pressure loss between the ends of the shock absorber. The discharge coefficient is calculated to find the relationship between the shock absorber hydraulic force and the strut telescoping velocity. In this paper, the l/d ratio was assumed as greater than 2. In line with the assumptions, the formula in Eq. 4 was used. According to the researches, C_d value was determined approximately 0.8 and the C_d value was assumed as 0.8 in [1, 15].

Friction force

The internal friction force in shock strut is;

$$F_f = \frac{\dot{S}}{|\dot{S}|}|F_{N\alpha}|\left[(\mu_1 + \mu_2)\frac{l_2 - S}{l_1 + S} + \mu_2\right], \tag{5}$$

$$F_{N\alpha} = \frac{w}{g}\ddot{Z}_1 \sin\alpha + F_{vg}\sin\alpha - W_2 \sin\alpha - F_{hg}\cos\alpha, \tag{6}$$

$$F_{hg} = F_{vg}\mu_{gr}, \tag{7}$$

where F_f is the friction force, $\dot{S}$ is the stroke telescoping velocity, $F_{N\alpha}$ is the force normal to the axis of the shock strut applied at axle, μ_1 is the friction coefficient between inlet cylinder and stroke surface above the orifice area, μ_2 is the friction coefficient between inlet cylinder and stroke surface at below the orifice area, l_1 is the distance between the axle and orifice area, l_2 is the distance between orifice area and upper of landing gear, α is the anteversion angle of shock strut, F_{vg} is the vertical force of tire, F_{hg} is the horizontal force of tire, μ_{gr} is the friction coefficient between ground and tire. There are two sources of friction which are tightness of seal and deformation of shock strut. The friction forces acting on the direction of strut were considered [16].

Tire force

Vertical tire force which is acting during the landing progress results from the tire compression is given by:

$$F_{vg} = (1 + \dot{Z}_2 C_T) f Z_2, \tag{8}$$

where $\dot{Z}_2$ is the tire hub vertical velocity, C_T is the vertical damping coefficient of the tire, fZ_2 is the tire static compression curve. Figure 2 shows the tire footprint. Where P is the internal tire pressure, R_L is the loaded radius, D_0 is the diameter of tire, d is the collapse distance. The dynamic friction coefficient changes depending on the forward speed of the aircraft in the x direction. The equation for the variable dynamic friction coefficient is given in below;

$$\mu(\lambda, v) = e^{C_4 \lambda v}[C_1(1 - e^{-C_2\lambda}) - C_3\lambda], \tag{9}$$

where C_1 is the friction curve maximum value, C_2 is the friction curve shape, λ is the slip ratio, μ is the aircraft forward speed, C_3 is the difference between the maximum value at $\lambda = 1$ and the maximum value of the friction curve, C_4 is in the range of $0.02 - 0.04 s/m$. For dry concrete condition parameters which used in this paper are: $C_1 = 1.2801$, $C_2 = 23.99$, $C_3 = 0.52$ and $C_4 = 0.03 s/m$ [17]. Figure 3 shows the relationship between slip ratio and friction coefficient.

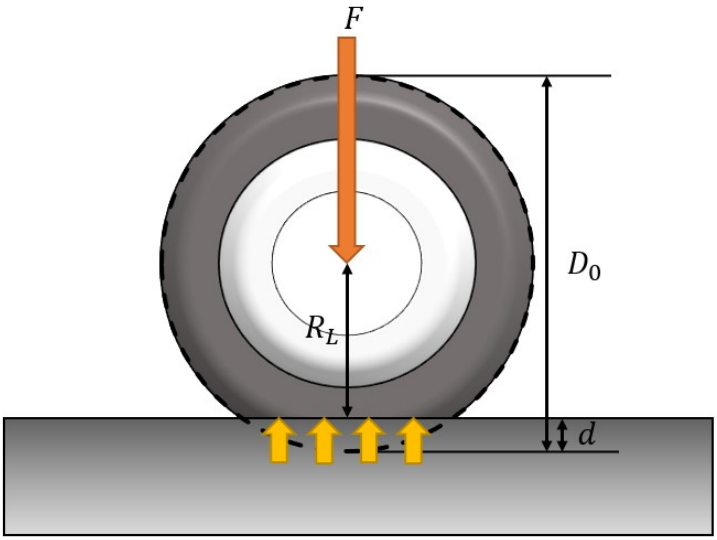

Figure 2. Tire footprint.

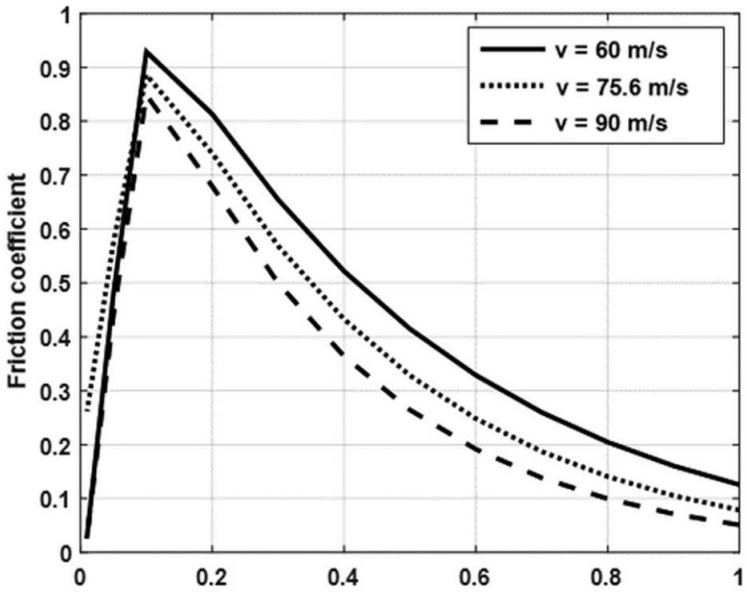

Figure 3. Relationship between λ and μ at different horizontal landing speeds [17].

Equations of motions

Tire rotation and deformation in horizontal direction are not considered, the nonlinear equations of motions are given below;

$$m_1\dot{Z}_1 = m_1 g - (F_a + F_h + F_f)\cos(\alpha), \tag{10}$$

$$m_2\dot{Z}_2 = m_2 g + (F_a + F_h + F_f)\cos(\alpha) - F_\mu, \tag{11}$$

where Z_1 and Z_2 are the vertical displacements of sprung (aircraft structure) and unsprung mass respectively [1]. Figure 4 shows the landing gear forces. $R_{(l,u)(x,y)}$ is the bearing reaction force at lower and upper, F_H is the hydraulic force, F_A is the air spring force, F_f is the friction force, F_{vg} and F_t are vertical and horizontal forces, α is anteversion angle of shock strut [18]. Figure 4 shows the free body diagram of the total system as two degrees of freedom.

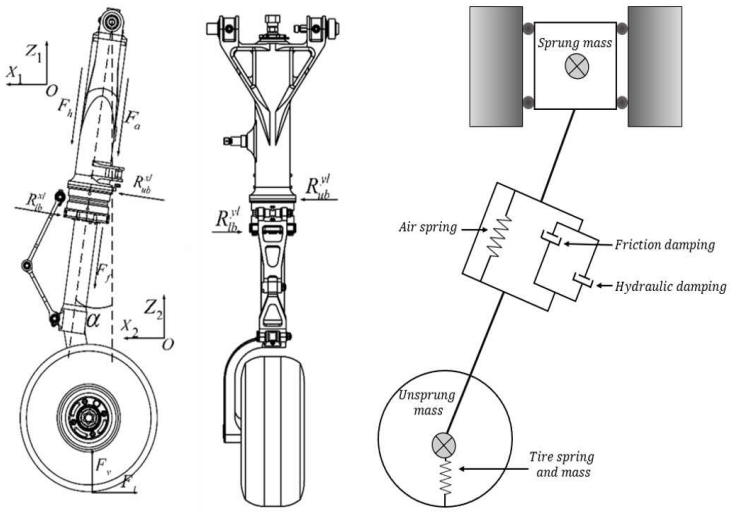

Figure 4. Forces on landing gear [1] and free body diagram of landing system.

3 Plant model development

Figure 5 shows the schematic of Simulink model. There is not any pneumatic force effect on aircraft at the initial time because there should be a reaction force of the pneumatic system to hold the airspring force. There is a pneumatic force but it does not affect aircraft force equilibrium. So, the initial force of the pneumatic system subtracts from the total strut force which directly affects the equations of motion. Figure 5 also shows the schematic of the flight dynamic model and dynamic friction coefficient connection. Since the forward speed of the aircraft v is a parameter that affects the dynamic friction coefficient function, the aircraft non-linear dynamic model is also considered in this paper. Figure 6 shows the results of dynamic friction coefficient's results depends on aircraft dynamics.

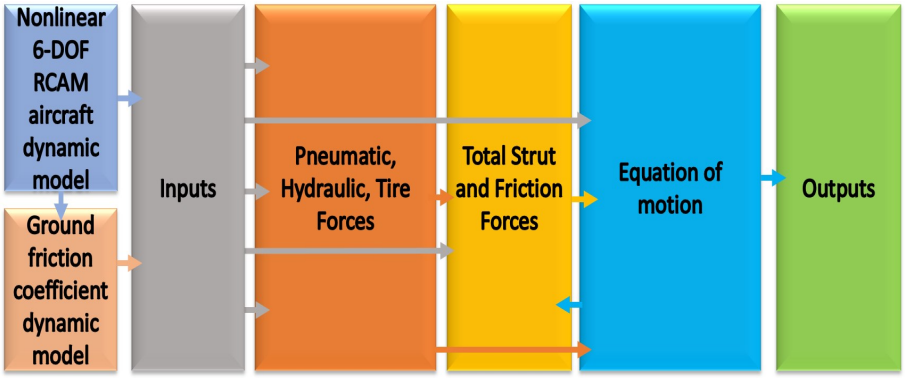

Figure 5. Schematic of Simulink model.

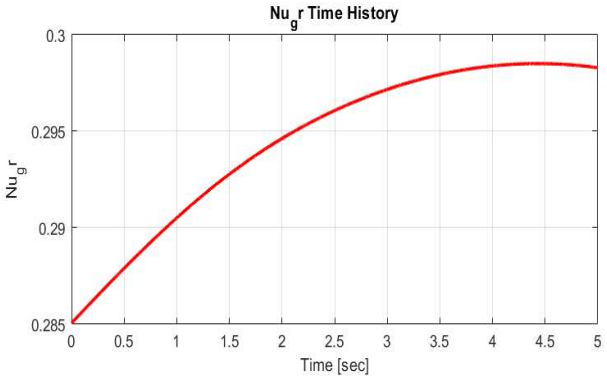

Figure 6. Dynamic friction coefficient results.

Table 1 shows the values of shock absorber system parameters.

Table 1. Parameter values and units

Parameters	Values	Units
A_a	0.014	m^2
A_h	0.013	m^2
A_n	0.0006412	m^2
n	1.6	–
ϕ	0	deg
k	950000	N/m
C_T	25000	Ns/m
μ_1	0.006	–
μ_2	0.006	–

4 Simulation results

To assess the optimum landing performance of an aircraft without any structural damage this section presents a series of simulation results that illustrate the behavior of the shock absorber system reacting to different impact velocities and initial air pressure in pneumatic system. According to the results of applying different impact velocities (2 m/s, 3 m/s, 4 m/s) to system, the displacement of sprung and unsprung mass increase proportionally with increase of impact velocities. Maximum displacement in sprung (strut) mass determined as 37.55 cm and displacement of unsprung (tire) mass determined as 15.31 cm in 4 m/s condition. Maximum loading on sprung mass that is critical structure was determined as -5.6 g and loading on unsprung mass was determined as -11.85 g. The passing time of damping of systems is inversely proportional to impact velocities because higher impact velocity creates more energy to absorb as shown on Figure 7 and Figure 8. According to the examination of these results, optimum impact velocity is determined as 3 m/s. Because, according to the design limits of sprung mass, the maximum load should be under -4.5 g. To reach the optimum performance, the impact velocity should be determined according to minimum damping time, maximum load below structural limits. Forces acting on the system according to different impact velocities as shown in Figure 9 and Figure 10.

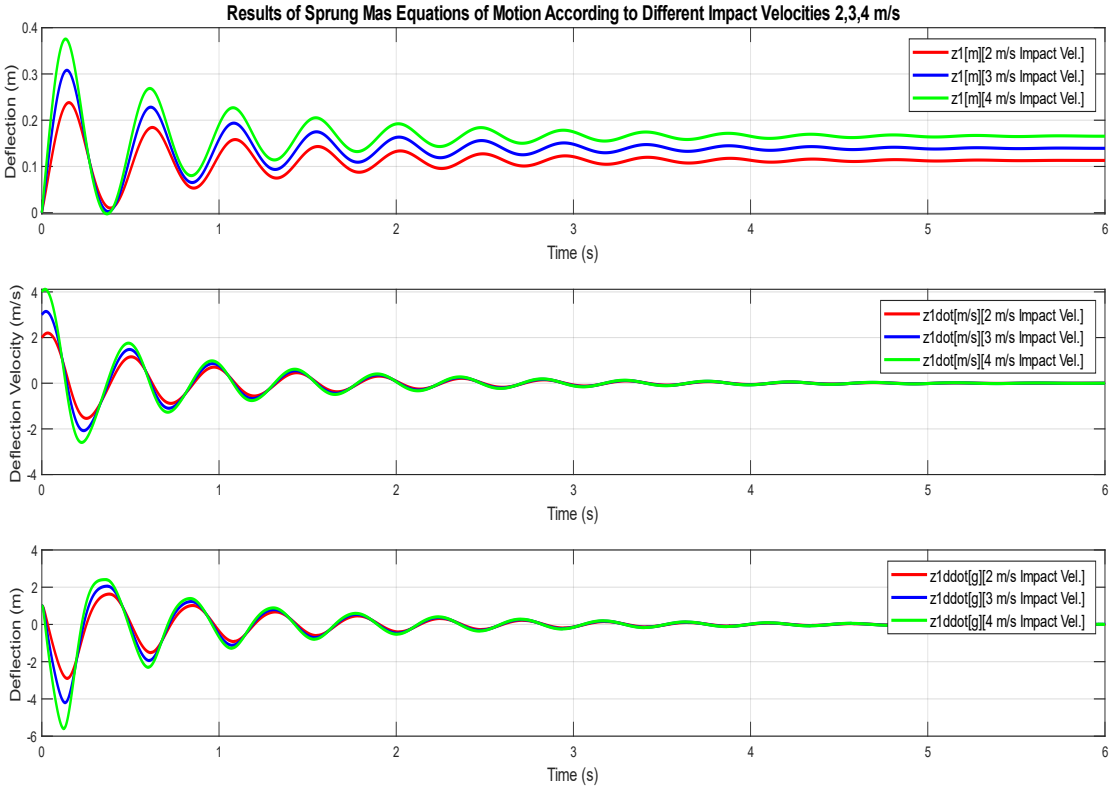

Figure 7. Sprung mass equations of motion results according to different impact velocities.

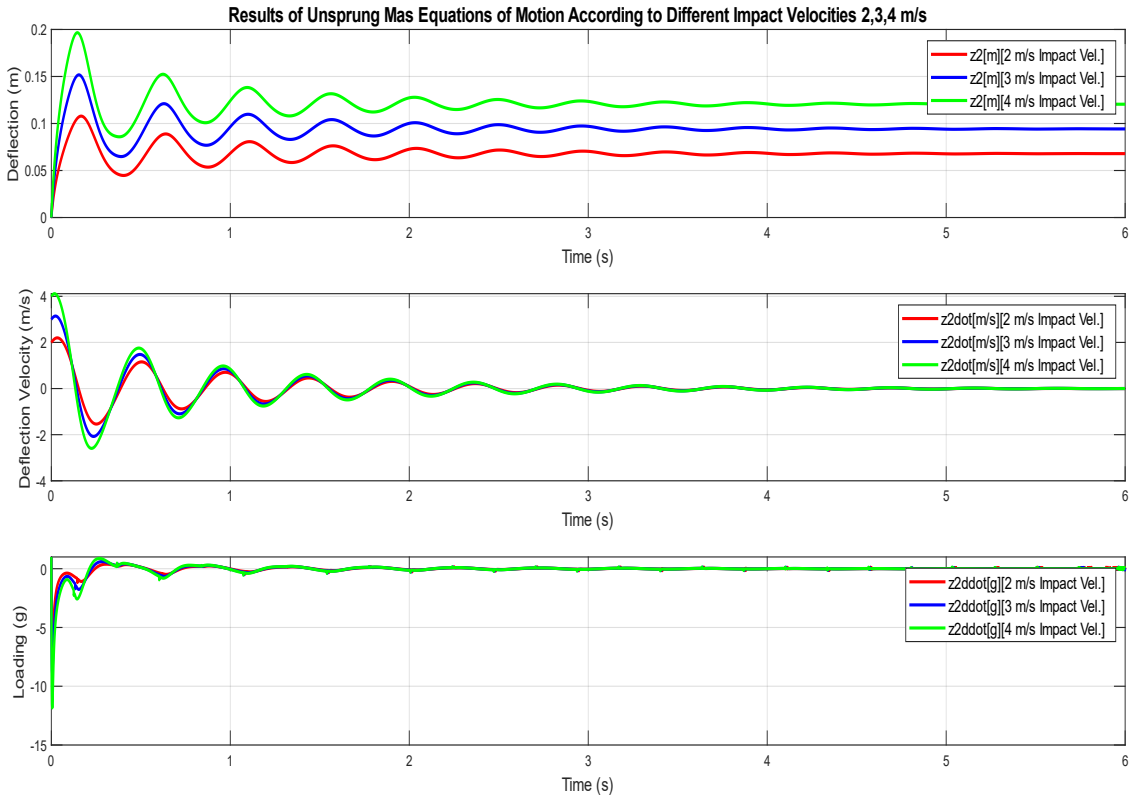

Figure 8. Unsprung mass equations of motion results according to different impact velocities.

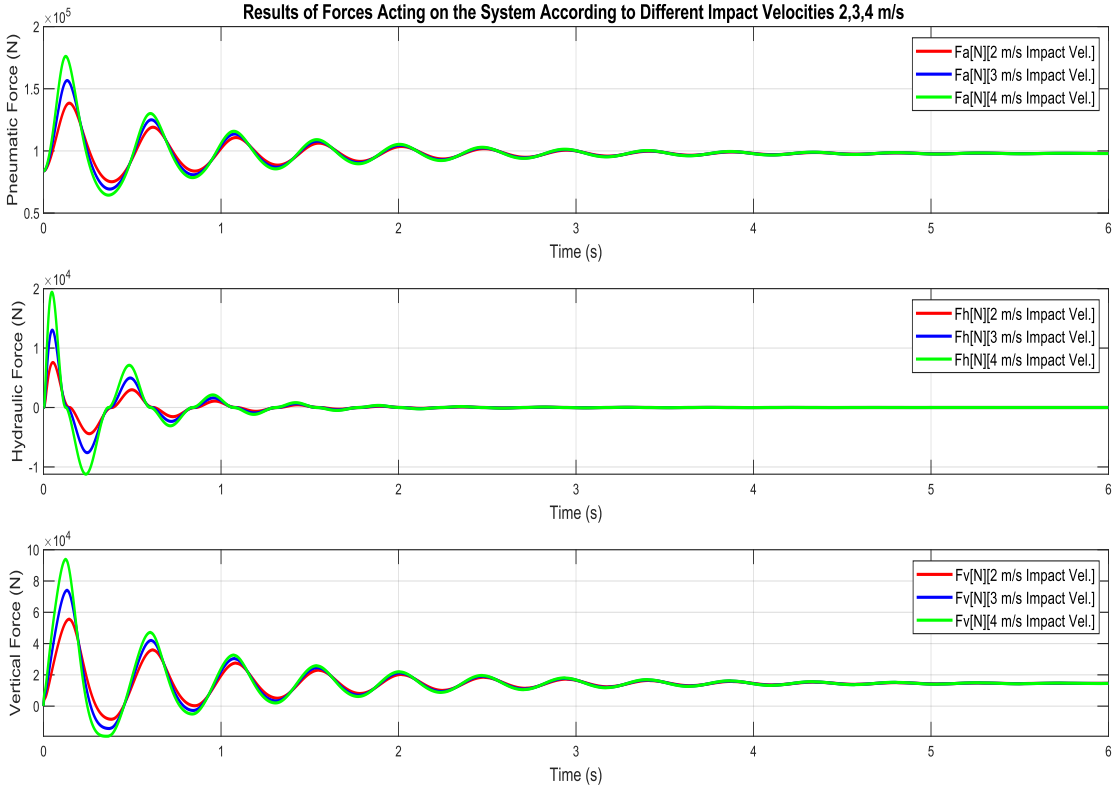

Figure 9. Forces acting on the system results according to different impact velocities.

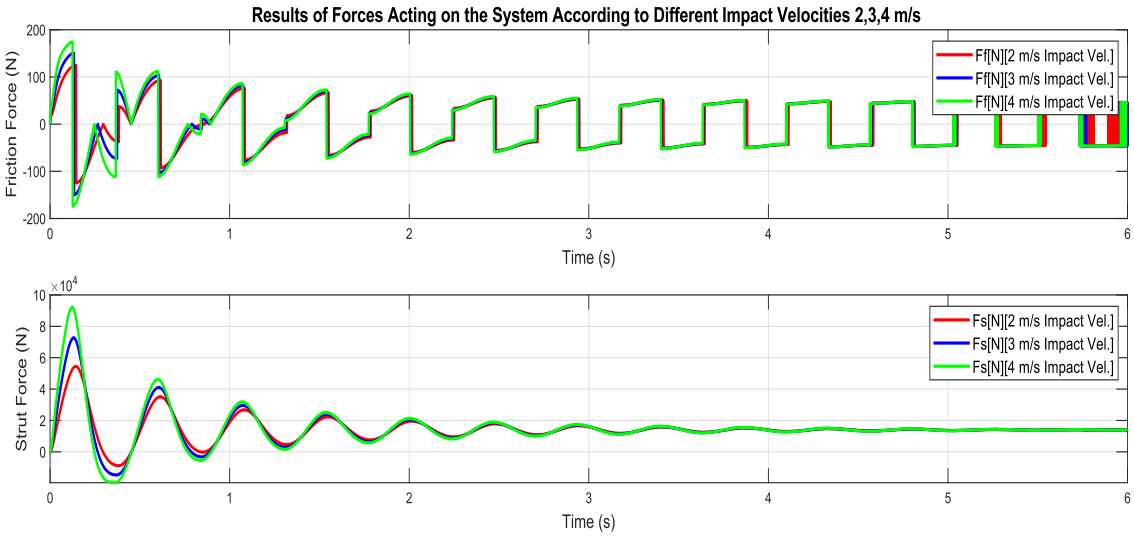

Figure 10. Forces acting on the system results according to different impact velocities.

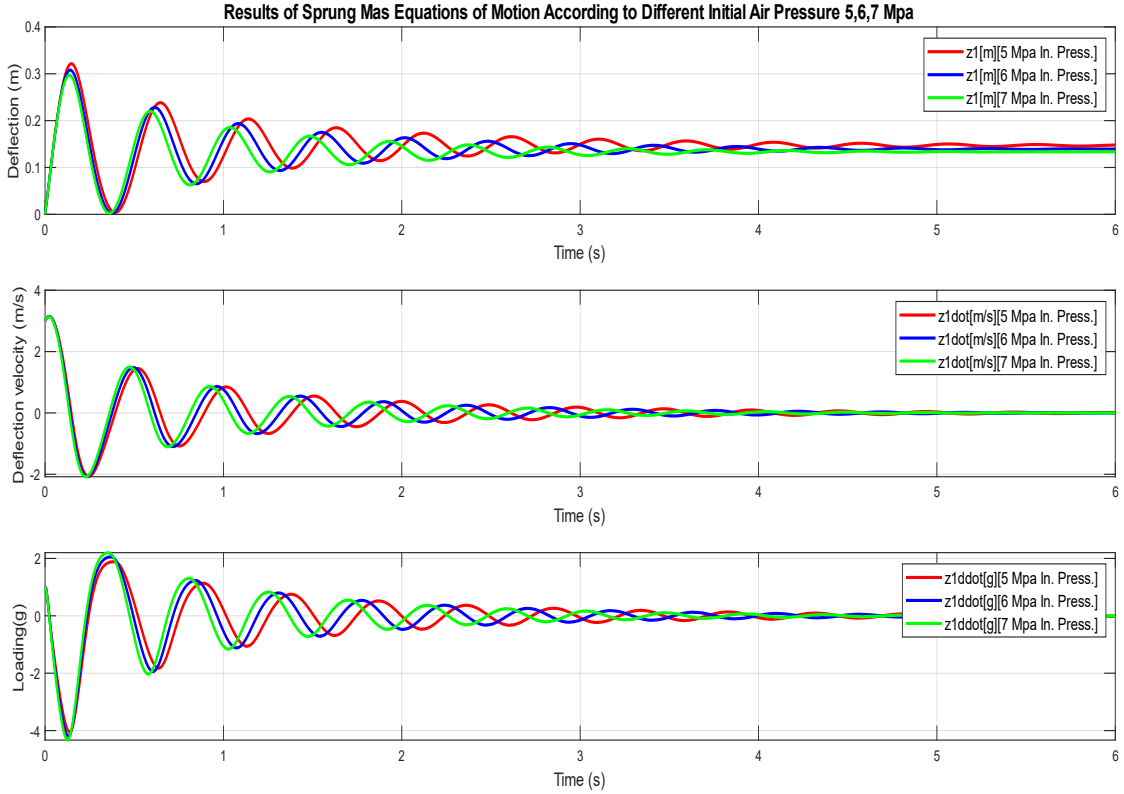

Figure 11. Sprung mass equations of motion results according to different initial air pressure.

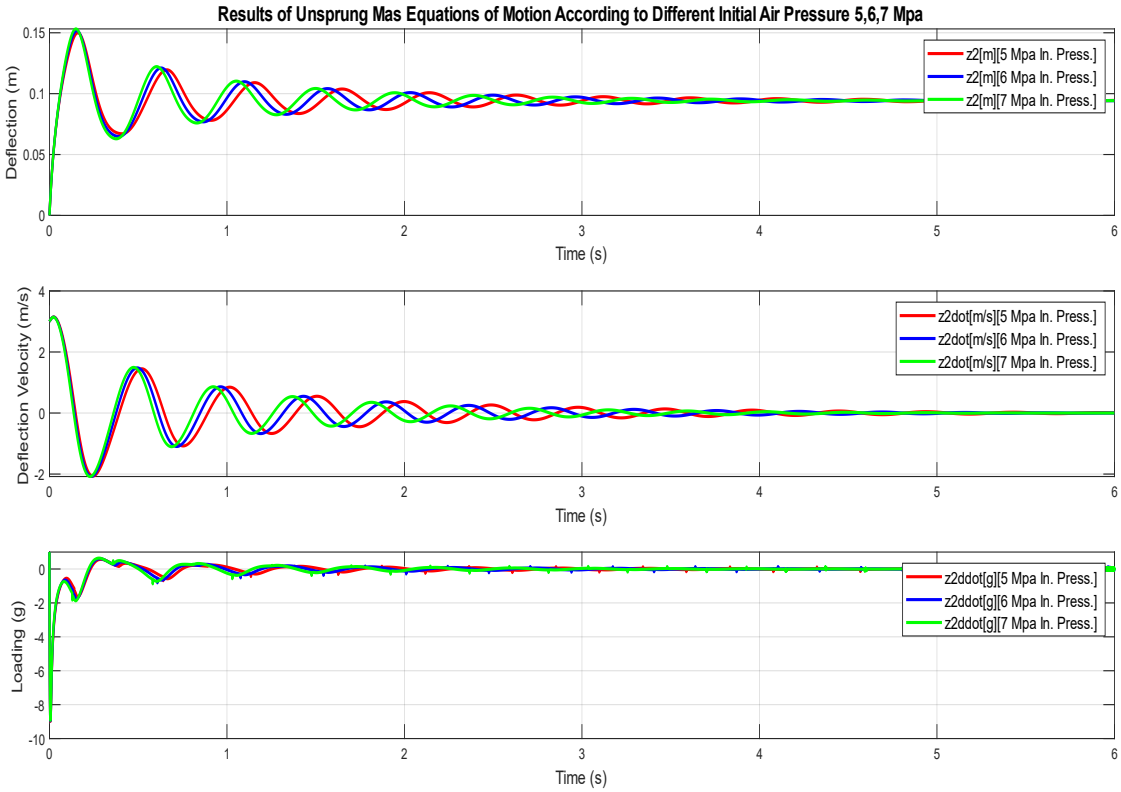

Figure 12. Unsprung mass equations of motion results according to different initial air pressure.

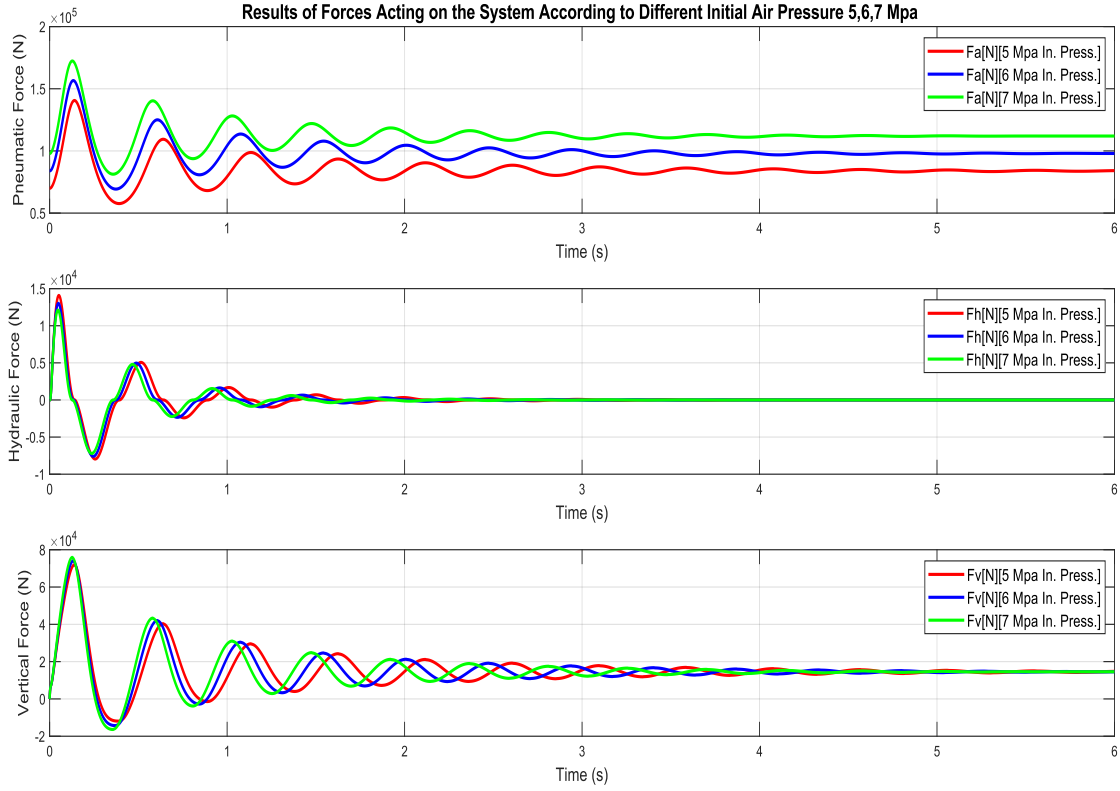

Figure 13. Forces acting on the system results according to different initial air pressure.

The system has also been simulated by applying 5 MPa, 6 MPa and 7 MPa initial air pressures with the 3 m/s impact velocity scenario, damping occurs in a short time of the displacement of sprung and unsprung mass in 7 MPa initial air pressure condition. In addition, when initial air pressure increases, the pneumatic force dramatically increases. The maximum sprung mass displacement was observed in 5 MPa initial air pressure condition as value of 32.15 cm as shown in Figure 11. The maximum unsprung mass displacement is observed in 7 MPa initial air pressure condition as value of 15.32 cm shown in Figure 12. The maximum loading on sprung mass is measured as -4.3 g at sprung mass in 7 MPa initial air pressure condition. The loading on unsprung mass is measured as -8.99 g at unsprung mass in 5 MPa initial air pressured shock absorber. According to the result of applying different initial air pressure, low pressure is more effective for sprung mass, high pressure is more effective for unsprung mass. Because high pressure in the pneumatic system behaves high spring coefficient, it creates more force and more loading but low pressure creates more oscillations and high damping time as shown in Figure 13. To sum up of the results, the most effective parameter on loading is determined as impact velocity so it is determined firstly, initial air pressure is scaled for reach optimum loading, tire deflection and damping time.

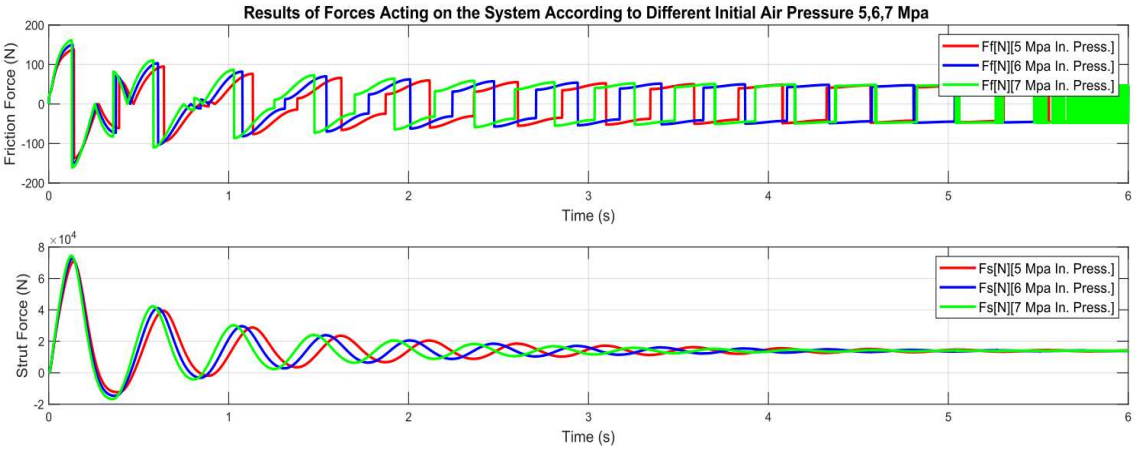

Figure 14. Forces acting on the system results according to different initial air pressure.

5 Conclusion

Landing gear shock absorber systems have a critical role in aircraft touchdown conditions. Because, there is an impact energy that needs to damping. It is important for safe landing condition. Landing gear shock absorber system dynamics have to be modelled before the manufacturing process to observe systems response. Thus, critical conditions can be predicted before a real flight and landing. Traditionally, landing gear characteristic observes with test apparatuses. This way takes a long time and more cost. However, landing gear dynamics which is modelled in model based environment such as Matlab/Simulink is cheaper and saves time. The paper has presented a perspective for shock absorber landing gear systems integrated to aircraft dynamics performance criteria. The proposed methodology relies on determining an analytical formulation of shock absorber system's equation of motion, modelling this formulation on model based environment (Matlab/Simulink) and integrating it with accurate aircraft nonlinear dynamic model to observe the performance of landing gear in different touchdown or impact velocities. Air spring force, hydraulic force, tire force, friction force and stroke position are the most important outputs of system to examine the results. The behavior of the system under different initial air pressure and impact velocities are investigated and determined with results for suitable landing gear performance. The relationship between tire and ground creates a friction force based on dynamic friction coefficient depending on aircraft dynamics. The quality of the result obtained clearly indicates that the approximation of founding optimum impact velocity and initial air pressure are suitable to aircraft and landing gear design limits. In this paper, the performance of the designed landing gear under different impact velocities and different design parameters has been investigated. In studies on landing gear design and optimization, the effect of changes in parameters such as air pressure and impact velocities on the system can be examined and system outputs can be compared with reference to this article. Therefore, this study will contribute to the developing and designing process of a landing gear for a new aircraft with decreasing time and economical aspects in the future.

Declarations

Consent for publication

Not applicable.

Conflicts of interest

The authors declare that they have no known competing financial interests or personal relationships that could have appeared to influence the work reported in this paper.

Funding

Not applicable.

Author's contributions

N.K.: Conceptualization, Methodology, Software, Validation, Formal Analysis, Investigation, Resources, Data Curation, Writing - Review and Editing, Visualization, Supervision, Project Administration. S.C.: Methodology, Investigation, Resources, Writing - Review and Editing. Z.G.: Investigation, Resources, Writing - Review and Editing, Funding Acquisition. M.H.: Conceptualization, Methodology, Investigation, Resources, Visualization, Writing - Review and Editing. All authors discussed the results and contributed to the final manuscript.

Acknowledgements

The authors acknowledge the funding provided for this research project (Project Number: 1919B012003602) by the Scientific and Technological Research Council of Turkey.

References

[1] Ding, Y.W., Wei, X.H., Nie, H. & Li, Y.P. Discharge coefficient calculation method of landing gear shock absorber and its influence on drop dynamics. *Journal of Vibroengineering*, 20(7), 2550-2562, (2018). [CrossRef]
[2] Wahi, M.K. Oleopneumatic shock strut dynamic analysis and its real-time simulation. *Journal of Aircraft*, 13(4), 303-308, (1976). [CrossRef]
[3] Daniels, J.N. A method for landing gear modeling and simulation with experimental validation. *NASA Reports*, (1996).
[4] Karakoc, T.H. & Erdem, M. Oleopneumatic shock absorber real-time simulation and analysis of the different oil service levels. *Japon Society of Mechanical Engineers Spring Annual Meeting*, 103-107, (1996).
[5] Oktay, T., Konar, M., Onay, M., Aydin, M., & Mohamed, M.A. Simultaneous small UAV and autopilot system design. *Aircraft Engineering and Aerospace Technology, Emerald Group Publishing Limited*, 88(6), 818-834, (2016). [CrossRef]
[6] Lomax, T.L. Structural loads analysis for commercial transport aircraft: theory and practice. *American Institute of Aeronautics and Astronautics*, (1996). [CrossRef]
[7] Gudmundsson, S. General aviation aircraft design: applied methods and procedures. *Butterworth-Heinemann*, (2013).
[8] CS-VLA, E.A.S.A. Certification specifications for very light aeroplanes. *Amendment*, (2009).
[9] FAA. Airworthiness standards, normal, utility, acrobatic and commuter category airplanes. *Federal Aviation Regulations,* Part 23.
[10] Yue, S., Nie, H., Zhang, M., Huang, M., Zhu, H., & Xu, D. Dynamic analysis for vertical soft landing of reusable launch vehicle with landing strut flexibility. *Proceedings of the Institution of Mechanical Engineers, Part G: Journal of Aerospace Engineering*, 233(4), 1377-1396, (2019). [CrossRef]
[11] Dinc, A. & Gharbia, Y. Effects of spring and damper elements in aircraft landing gear dynamics. *International Journal of Recent Technology and Engineering IJRTE*, 8(5), 4265-4269, (2020).
[12] Milwitzky, B. & Cook, F.E. Analysis of landing gear behavior. *National Advisory Committee for Aeronautics Report 1154*, (1953).
[13] Li, Y., Jiang, J.Z., Sartor, P., Neild, S.A. & Wang, H. Including inerters in aircraft landing gear shock strut to improve the touch-down performance. *Procedia Engineering*, 199, 1689-1694, (2017). [CrossRef]
[14] Açin, S. Uçak fren balatalarında karbon fiber boyut ve şeklinin tribolojik özelliklere etkisi. *Master Thesis*, Kocaeli University, (2019).
[15] Li, Y., Jiang, J.Z., Neild, S.A., & Wang, H. Optimal inerter-based shock-strut configurations for landing-gear touchdown performance. *Journal of Aircraft, AIAA*, 54(5), 1901-1909, (2017). [CrossRef]
[16] Wei, X.H., Liu, C.L., Song, X.C., Nie, H. & Shao, Y.Z. Drop dynamic analysis of half-axle flexible aircraft landing gear. *Journal of Vibroengineering, JVE International Ltd.*, 16(1), 266-274, (2014).
[17] Alroqi, A.A., Wang, W., & Zhao, Y. Aircraft tire temperature at touchdown with wheel prerotation. *Journal of Aircraft, AIAA*, 54(3), 926-938, (2017). [CrossRef]
[18] Yazici, H. & Sever, M. Active control of a non-linear landing gear system having oleo pneumatic shock absorber using robust linear quadratic regulator approach. *Proceedings of the Institution of Mechanical Engineers, Part G: Journal of Aerospace Engineering, Sage UK: London, England*, 232(13), 2397-2411, (2017). [CrossRef]